MODELING THE DYNAMICS OF MATERIALS PROCESSING AND ELECTROCHEMICAL SYSTEMS FOR ENERGY STORAGE APPLICATIONS

A Dissertation
Presented to the Faculty of the Graduate School
of Cornell University
In Partial Fulfillment of the Requirements for the Degree of
Doctor of Philosophy

by
George Leonard Shebert
August 2019

MODELING THE DYNAMICS OF MATERIALS PROCESSING AND ELECTROCHEMICAL SYSTEMS FOR ENERGY STORAGE APPLICATIONS

George Leonard Shebert, Ph. D.

Cornell University 2019

To realize the promise of electric vehicles, personal electronics, and renewable energy sources, improvements in energy storage technology are crucial. However, avenues for improvement such as designing superior electrode materials or modifying the battery electrolyte and separator are difficult without sufficient understanding of the materials and processes used to produce them. One such process is electrospinning, which uses high voltage to produce polymer nanofibers cheaply and continuously. To examine the effect of electrospinning on material morphology, the placement of nanoparticles within lamella-forming polymer blends and block copolymers is simulated using molecular dynamics under planar elongational flow. Then, extensional flow is combined with cylindrical confinement to simulate a block copolymer-filled cylinder with a constantly shrinking diameter, which is a better model for electrospinning. The appearance of ordered or disordered morphologies is found to be connected to a Weissenberg number relating the deformation and self-assembly time scales.

A second approach towards understanding energy storage systems is to simulate the battery's electrochemical performance. Of particular interest is the lithium-sulfur (Li-S) battery, which aims to replace lithium-ion batteries due to its higher specific capacity and cheaper material costs. However, well-known challenges such as polysulfide crossover, large volume changes during cycling, and deposition of insulating lithium sulfide limit the capacity and capacity retention of Li-S batteries. Using a continuum-level numerical simulation which includes reaction, mass transport, adsorption, and nucleation, these challenges are investigated in order to explain the mechanisms underlying Li-S discharge behavior. The model is used to explain the end-of-discharge failure behavior of liquid and gel electrolyte systems, finding that insufficient mass transport of polysulfides is the cause. In addition, the effects of adsorptive materials, cathode passivation with insulating lithium sulfide, and spherical carbon cathode particle geometry is investigated. It is found that adsorptive materials can greatly improve battery performance when the location of lithium sulfide deposition is considered in the model. Finally, the model suggests that different cathode processing techniques in experiment can lead to different end-of-discharge failure mechanisms.

BIOGRAPHICAL SKETCH

George Shebert was born in Luxembourg on March 30th, 1992, and grew up outside of Rochester, New York. He naturally leaned towards quantitative thinking in school which led him to follow in the footsteps of his mother and major in Chemical Engineering at University of Rochester. In his junior year, he became interested in graduate research in order to pursue newfound interests in computer simulation and programming. After visiting Cornell University, he decided to join the PhD program and entered Professor Joo's group in the Chemical and Biomolecular Engineering Department in Fall 2014. In Professor Joo's group, he had the opportunity to develop multiple types of simulations in polymer self-assembly and lithium-sulfur batteries and use them towards applications in materials and energy storage.

ACKNOWLEDGMENTS

I would like to express my deep appreciation to my advisor Professor Yong Lak Joo for his guidance, patience, and encouragement during my PhD studies. I acknowledge my committee members Professor Fernando Escobedo, Professor Uli Wiesner, and Professor Jin Suntivich for their support and perspectives. In the Joo group, I appreciate Dr. Brian Williams, Dr. Joe Carlin, Professor Jay Park, Dr. Yevgen Zhmayev, Dr. Mounica Divvela, Dr. Somayeh Zamani, Rui Zhang, and Christopher Klaassen for both their assistance in research and their camaraderie. For insightful and fun discussions as well as friendship and advice, I would like to sincerely thank Dr. Shubham Pinge. Lastly, I would like to thank my mother, father, sister, and brother. Without their emotional support, this research would not have been possible.

TABLE OF CONTENTS

LIST OF FIGURES

LIST OF TABLES

CHAPTER 1

INTRODUCTION

1.1 The role of energy storage

A fundamental purpose of energy storage technology is to provide heat, light, mechanical work, or electricity, particularly in a portable form. In earlier centuries, energy storage existed primarily in the form of unsustainable fuel combustibles like coal and whale oil which could be used to power trains or lamps during travel. These energy storage devices were "charged" by nature and then harvested by humans for discharge. Even today, gasoline is predominantly used to provide portable energy for automobiles. However, despite their high energy density and simplicity, such hydrocarbon fuels suffer from their wasteful single use nature and their inability to be miniaturized. Rechargeable or secondary energy storage like batteries satisfy these requirements by taking in external energy and storing it efficiently, which can then be recovered later. Such a system should be able to last hundreds or thousands of cycles of charge and discharge to maintain cost efficiency. While as of yet unable to match the energy density of fossil fuels, secondary batteries have achieved widespread use in today's economy.[1]

The most prominent secondary battery in use today is the lithium-ion battery (Li-ion). In this battery, external electric current is stored by electrochemically converting lithium ion (Li^+) stored in the nickel-manganese-cobalt (NMC) cathode into Li intercalated into the graphite anode. The reverse occurs upon discharge to produce electricity, and 1000s of cycles are possible before battery failure.[2] These batteries have obtained widespread use in personal electronics like smartphones and an increasing number of battery-powered electric vehicles. However, after decades of relatively slow improvement in Li-ion battery performance, batteries are struggling to meet the increasing requirements of electric vehicles which demand a 300-400 mile operating range with limitations on battery volume and mass.[3] Until energy storage technology can become more energy dense, more efficient, and more long-lasting, it will be difficult to move away from modern society's reliance on fossil fuels.

1.2 The lithium-sulfur battery

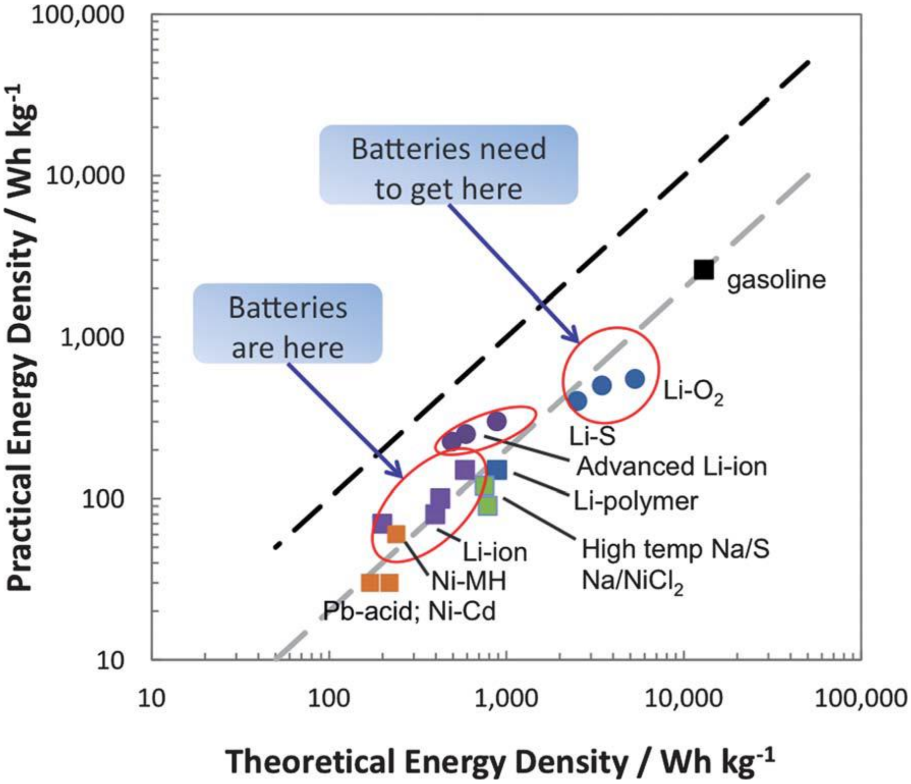

Figure 1.1 Energy densities of varying battery chemistries compared to gasoline. (Thackeray, Wolverton, and Isaacs 2012[3])

An overview of the energy densities for different types of batteries is presented in Figure 1.1. Among the highest theoretical energy densities for secondary batteries are lithium-oxygen (Li-O_2) and lithium-sulfur (Li-S). Li-O_2 has the advantage of potentially using plentiful atmospheric oxygen as a reactant, but suffers from severe challenges in lifetime which require further research and development.[4] Li-S is closer to becoming a viable alternative to Li-ion, which has led government organizations like the Department of Energy, research universities, and private companies to devote substantial efforts towards Li-S research. In Figure 1.2, the increasing number of publications focusing on Li-S is illustrated.

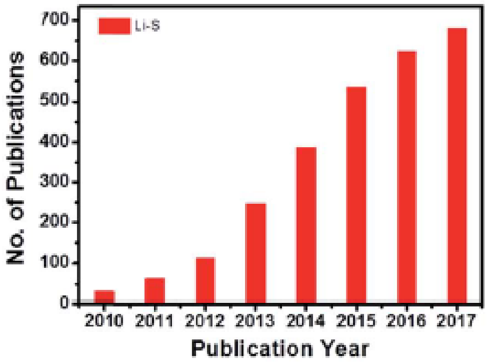

Figure 1.2 Li-S publications per year. From Kumar et al. 2018.[5]

The Li-S battery is typically constructing with a lithium metal anode, a polyolefin separator, and a carbon/sulfur composite cathode. The battery is filled with organic glyme-based electrolyte with dissolved lithium salts. During discharge, Li-S batteries convert a Li metal anode into Li^+ ions, which migrate to the cathode. Simultaneously, sulfur (S_8) is reduced at the cathode and combines with Li^+ to form lithium polysulfides. These polysulfides are intermediate reactive species with the varying lengths of sulfur, with longest begin Li_2S_8. As discharge continues, longer-chain polysulfides with more sulfur like Li_2S_8 are successively reduced into short-chain polysulfides like Li_2S_6 and Li_2S_4. The polysulfides are soluble in the electrolyte and can undergo side reactions with the lithium metal if they diffuse across the battery to the anode. The varying reactivity of these intermediates gives Li-S its distinctive discharge voltage vs. capacity curve, shown in Figure 1.3, which can be divided into four regions. After elemental sulfur is consumed in region 1 and long-chain polysulfides are consumed in region 2, a long plateau of constant voltage is observed. This is due to reaction of Li_2S_4 to form Li_2S, which is insoluble and precipitates onto the carbon cathode surface. The constant precipitation of reaction products keeps the reaction equilibrium in favor of the forward direction, leading to the constant voltage profile. A visualization of the battery structure and discharge process is shown in Figure 1.4. During charging, Li_2S s converted back to elemental sulfur in the reverse process. The anode and cathode half-reactions for the Li-S battery is given below:

Anode half reaction:

$$2\mathrm{Li} \rightleftharpoons 2\mathrm{Li}^{+} + 2e^{-}$$

Cathode half reaction:

$$\mathrm{S} + 2\mathrm{Li}^{+} + 2e^{-} \rightleftharpoons \mathrm{Li}_2\mathrm{S}$$

where the forward reaction is battery discharge.

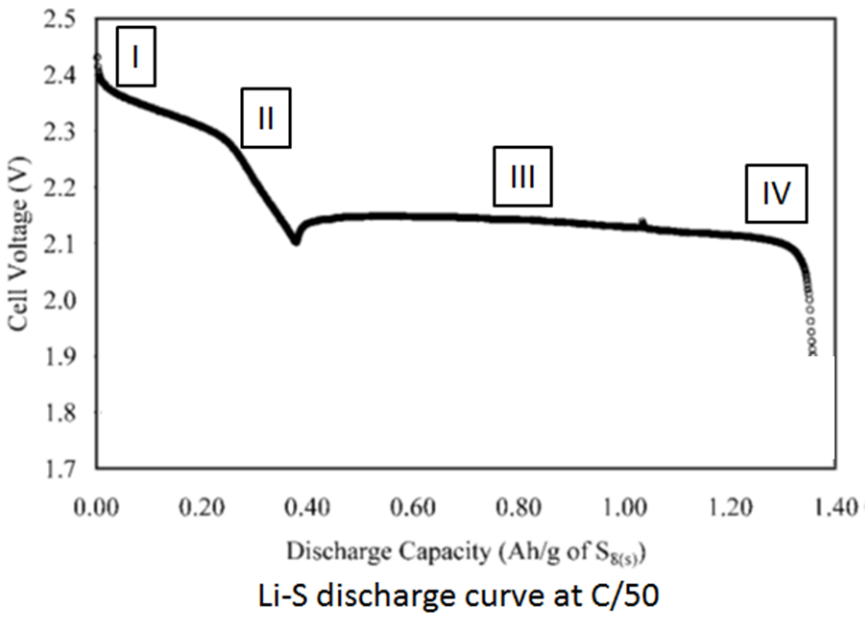

Figure 1.3 Representative discharge voltage vs. discharge capacity curve for a Li-S battery. The reactions occurring within the battery at different points leads to a four region division. Adapted from Kumaresan et al. 2008.[6]

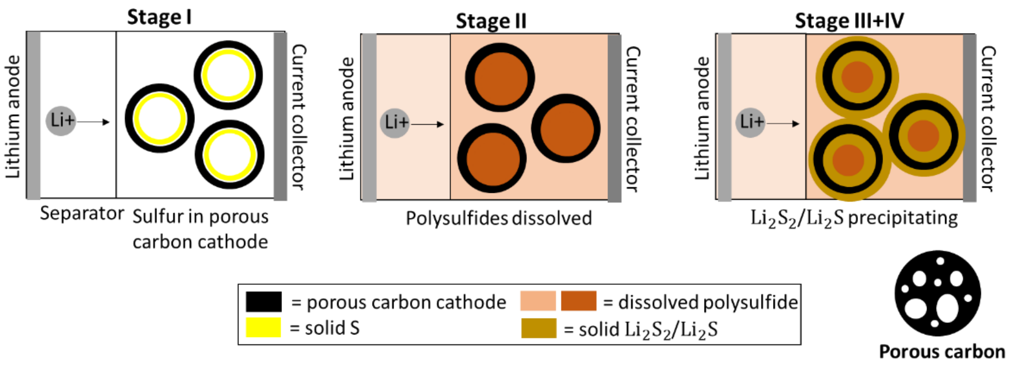

Figure 1.4 Visualization of the Li-S discharge process and battery structure.

Li-S batteries are promising due to their higher theoretical energy densities. In addition, they also benefit from lower material costs. Instead of the expensive cobalt metal commonly used in Li-ion batteries cathodes, inexpensive and naturally abundant sulfur is used. The challenges of cobalt sourcing and an example of sulfur’s abundance as a petroleum refining byproduct are shown in Figure 1.5. Despite these advantages, Li-S faces significant challenges such as polysulfide crossover, large volume changes in the cathode during cycling, and passivation of reaction sites which limit the capacity and capacity retention. Research has frequently focused on improving materials used in the cathode, separator, and electrolyte in order to mitigate these issues. However, the complexity of physics and chemical species in Li-S makes interpretation of experimental results challenging, leading researchers to develop Li-S battery simulation techniques.

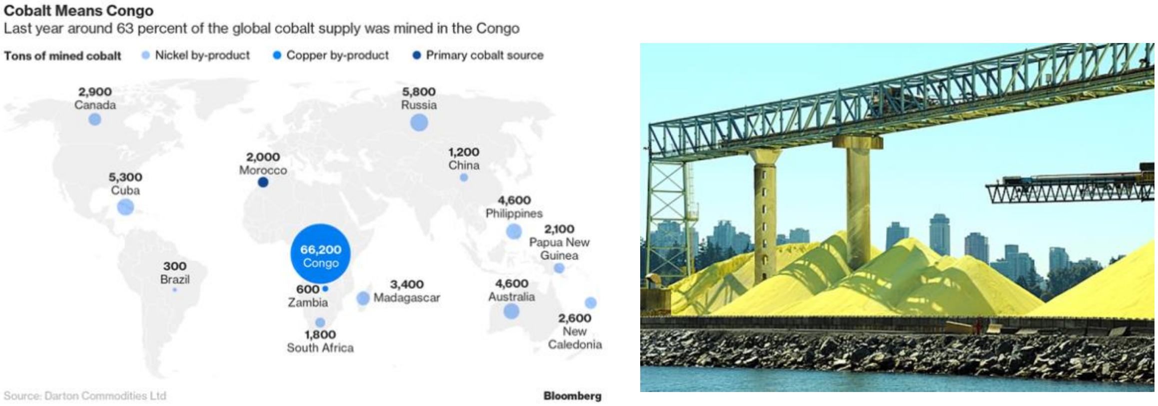

Figure 1.5 Left: global production of cobalt in tons during 2017. Source: Bloomberg News. Right: elemental sulfur piles in North Vancouver. Source: North Shore News.

These numerical simulations attempt to obtain the concentrations and voltages of the Li-S battery by solving the governing partial differential equations numerically. While limited in accuracy due to the complexity of the Li-S system and incomplete knowledge of model parameters, such models are able to conveniently investigate the effect of individual variables compared to time-consuming and difficult-to-control experimental methods. If the model captures the proper electrochemical mechanisms present in the battery, it can serve as a guiding tool for researchers attempting to solve problems in their experiments and propose avenues for improved battery performance. Towards this end, Li-S simulations are presented in Chapters 3 and 4 which investigate the effects of cathode structure, adsorption, and electrolyte on battery performance. An investigation of end-of-discharge failure mechanisms is also presented and compared to experimental results.

1.3 Materials for energy storage applications

1.3.1 Electrospun polymer and carbon materials

A common feature of Li-ion, Li-S, Li-O_2, and even flow battery chemistries like Zinc-Bromine is that better battery performance is achieved through improvements in the electrode materials, separator materials, or electrolyte composition. In particular, all of the batteries listed rely on carbon materials in their anode or cathode. This is due to carbon's chemical inertness, low cost, high conductivity, and adjustable surface area and pore structures. In addition, innovations in carbon materials such as the development of graphene have opened even more avenues for research.[7] Carbon can also be combined with nanoparticles to add further control over the thermal conductivity, electric conductivity, and catalytic properties of the nanocomposite.[8]

Creating suitable carbon and polymer materials with tunable properties is critical towards the success of energy storage systems. Surface area and pore structure of the carbon influence the catalytic properties of the carbon, and conductivity of the bulk carbon cathode must be maximized. The process of electrospinning is suitable for this task, as it yields sub-micron diameter nanofibers continuously, scalably, and easily. The fibers have high surface area due to their small diameter and high conductivity due to their interconnectivity. A micrograph of electrospun nanofibers is shown in Figure 1.6.

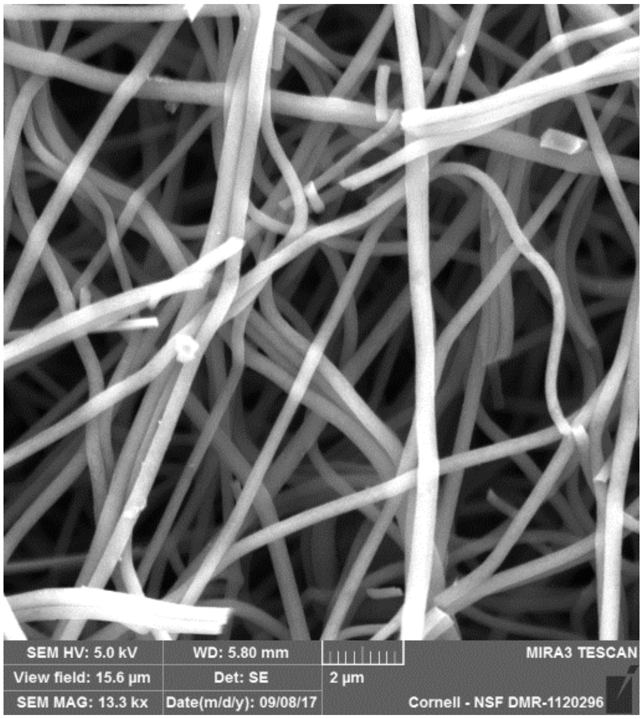

Figure 1.6 Scanning electron microscope image of electrospun polyacrylonitrile.

The process starts with a polymer solution, which is ejected from a nozzle under high voltage and travels through the air to a collector plate.[9] While in the air, the solvent evaporates and electrostatic charge on the fiber surface results in whipping motion, which stretches the polymer fiber down to nanoscale diameters. After the randomly deposited polymer is collected, it can be heated under high temperatures to produce carbon fibers. Carbon fibers with controlled pore structure can be created by using a combination of two polymers and subsequently removing one polymer to leave behind pores.[10] If nanoparticles are mixed into the initial polymer solution, a nanocomposite fiber can be produced, allowing additional control over properties. The properties of such a nanocomposite fiber will be maximized if the dispersion of nanoparticles is a good as possible. A schematic of the carbon fiber synthetic process is provided in Figure 1.7.

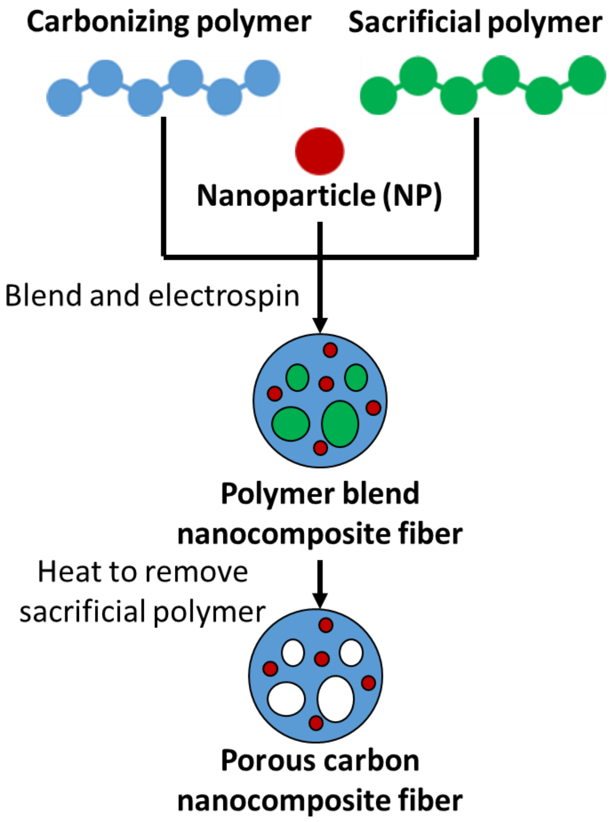

Figure 1.7 Schematic of carbon nanocomposite fiber production using electrospinning.

Electrospinning applies high extensional deformation and cylindrical confinement to the polymer fiber which may affect the morphology of the polymers and the dispersion of nanoparticles.[11,12] If block copolymers are used, which consist of two unlike polymers bonded together, ordered structures can form which also may be affected by the extensional strain. These ordered structures are useful to create ordered pore structures upon removal of one polymer or to aid in the dispersion of nanoparticles. In order to better understand these effects, this work uses molecular dynamics simulations combined with extension and confinement effects to simulate the electrospinning process. Molecular dynamics is a versatile simulation technique frequently used for polymer systems which solves Newton's equations of motion by calculating the forces between nearby atoms. In Chapter 2, immiscible polymer blends and block copolymers with nanoparticle additives are simulated under planar elongation flow. In Chapter 3, uniaxial extensional deformation is combined with cylindrical confinement to further improve the simulation, and the self-assembly behaviour of block copolymers under electrospinning conditions is simulated. Visualizations of the PEF and UEF deformations are shown in Figure 1.8. An application of the simulation towards materials for Li-ion batteries is also included in Chapter 2.

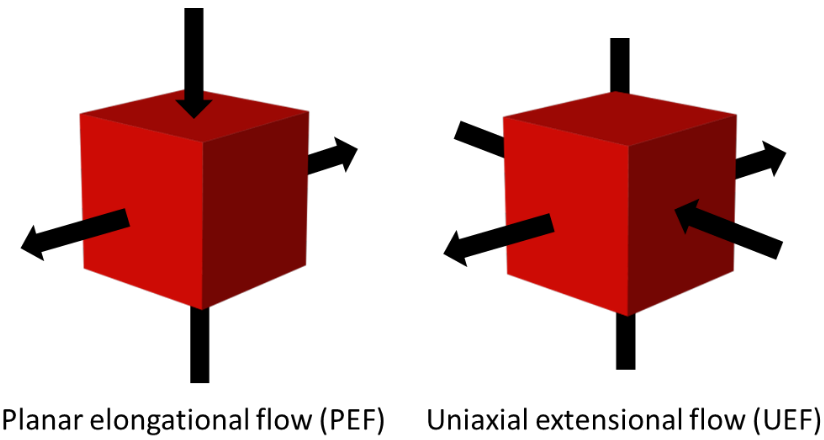

Figure 1.8 Compression and expansion directions for the two deformation fields that were implemented in molecular dynamics simulations of polymers.

1.3.2 Graphene materials: synthesis and transportation

Graphene is a newer form of carbon which has promising applications in energy storage due to its unique 2-d structure.[13] This yields high surface, conductivity, and catalytic properties compared to the commonly used graphite form. Improvements in the production and transportation of graphene are necessary to allow further reductions in cost that will enable adoption in batteries. Graphene synthetic methods like chemical vapor deposition are unsuitable for mass production to their cost. Transportation of graphene is also challenging due to the aggregation and restacking of graphene into graphite, a problem which requires graphene to be dispersed at low percentages in water. Towards solving these issues, research into alternative graphene processes that use high shear flow to exfoliate graphene can increase the rate of production. For transport, water dispersion medium can potentially be avoided through graphene fiber spinning, which uses a coagulating agent to create a micron scale graphene fiber from a dispersed graphene solution. The effect of these two processing techniques on graphene and graphite is simulated in Chapter 6 using a nonequilibrium molecular dynamics approach.

Overall, this thesis focuses on improving fundamental understanding of energy storage materials through simulation methods. Two main approaches are used: first, the effects of the electrospinning process are simulated to determine their effect on material properties; and second, Li-S batteries are simulated to understand the mechanisms at work during battery discharge.

1.4 References

1. Choi, J. W. & Aurbach, D. Promise and reality of post-lithium-ion batteries with high energy densities. *Nature Reviews Materials* **1**, (2016).
2. Cheng, X., Pan, J., Zhao, Y., Liao, M. & Peng, H. Gel Polymer Electrolytes for Electrochemical Energy Storage. *Adv. Energy Mater.* **8**, 1–16 (2018).
3. Thackeray, M. M., Wolverton, C. & Isaacs, E. D. Electrical energy storage for transportation - Approaching the limits of, and going beyond, lithium-ion batteries. *Energy Environ. Sci.* **5**, 7854–7863 (2012).
4. Girishkumar, G., McCloskey, B., Luntz, A. C., Swanson, S. & Wilcke, W. Lithium-air battery: Promise and challenges. *J. Phys. Chem. Lett.* **1**, 2193–2203 (2010).
5. Kumar, R., Liu, J., Hwang, J. Y. & Sun, Y. K. Recent research trends in Li-S

batteries. *J. Mater. Chem. A* **6**, 11582–11605 (2018).

6. Kumaresan, K., Mikhaylik, Y. & White, R. E. A Mathematical Model for a Lithium–Sulfur Cell. *J. Electrochem. Soc.* **155**, A576 (2008).

7. Halim, W. *et al.* Directly deposited binder-free sulfur electrode enabled by air-controlled electrospray process. *ACS Appl. Energy Mater.* **2**, 678–686 (2019).

8. Li, B. *et al.* Bismuth nanoparticle decorating graphite felt as a high-performance electrode for an all-vanadium redox flow battery. *Nano Lett.* **13**, 1330–1335 (2013).

9. Chen, Q., Saha, P., Kim, N. G. & Kim, J. K. Processing and characterization of electrospun trans-polyisoprene nanofibers. *J. Polym. Eng.* **35**, 53–59 (2015).

10. Williams, B. P. & Joo, Y. L. Tunable Large Mesopores in Carbon Nanofiber Interlayers for High-Rate Lithium Sulfur Batteries. *J. Electrochem. Soc.* **163**, A2745–A2756 (2016).

11. Zhmayev, Y. *et al.* Controlling the Placement of Spherical Nanoparticles in Electrically Driven Polymer Jets and its Application to Li-Ion Battery Anodes. *Small* 5543–5553 (2016). doi:10.1002/smll.201601878

12. Zhmayev, Y. *et al.* Non-enthalpic enhancement of spatial distribution and orientation of CNTs and GNRs in polymer nanofibers. *Polymer.* **178**, 121551 (2019).

13. Munaiah, Y., Ragupathy, P. & Pillai, V. K. Single-Step Synthesis of Halogenated Graphene through Electrochemical Exfoliation and Its Utilization as Electrodes for Zinc Bromine Redox Flow Battery. *J. Electrochem. Soc.* **163**, A2899–A2910 (2016).

CHAPTER 2

EFFECT OF ELONGATIONAL FLOW ON IMMISCIBLE POLYMER BLEND/NANOPARTICLE COMPOSITES: A MOLECULAR DYNAMICS STUDY

Using coarse-grained nonequilibrium molecular dynamics, the dynamics of a blend of the equal ratio of immiscible polymers mixed with nanoparticles (NP) are simulated. The simulations are conducted under planar elongational flow, which affects the dispersion of the NPs and the self-assembly morphology. The goal of this study is to investigate the effect of planar elongational flow on the nanocomposite blend system as well as to thoroughly compare the blend to an analogous symmetric block copolymer (BCP) system to understand the role of the polymer structure on the morphology and NP dispersion. Two types of spherical NPs are considered: (1) selective NPs that are attracted to one of the polymer components and (2) nonselective NPs that are neutral to both components. A comparison of the blend and BCP systems reveals that for selective NP, the blend system shows a much broader NP distribution in the selective phase than the BCP phase. This is due to a more uniform distribution of polymer chain ends throughout the selective phase in the blend system than the BCP system. For nonselective NP, the blend and BCP systems show similar results for low elongation rates, but the NP peak in the BCP system broadens as elongation rates approach the order-disorder transition. In addition, the presence of NP is found to affect the morphology transitions of both the blend and BCP systems, depending on the NP type.

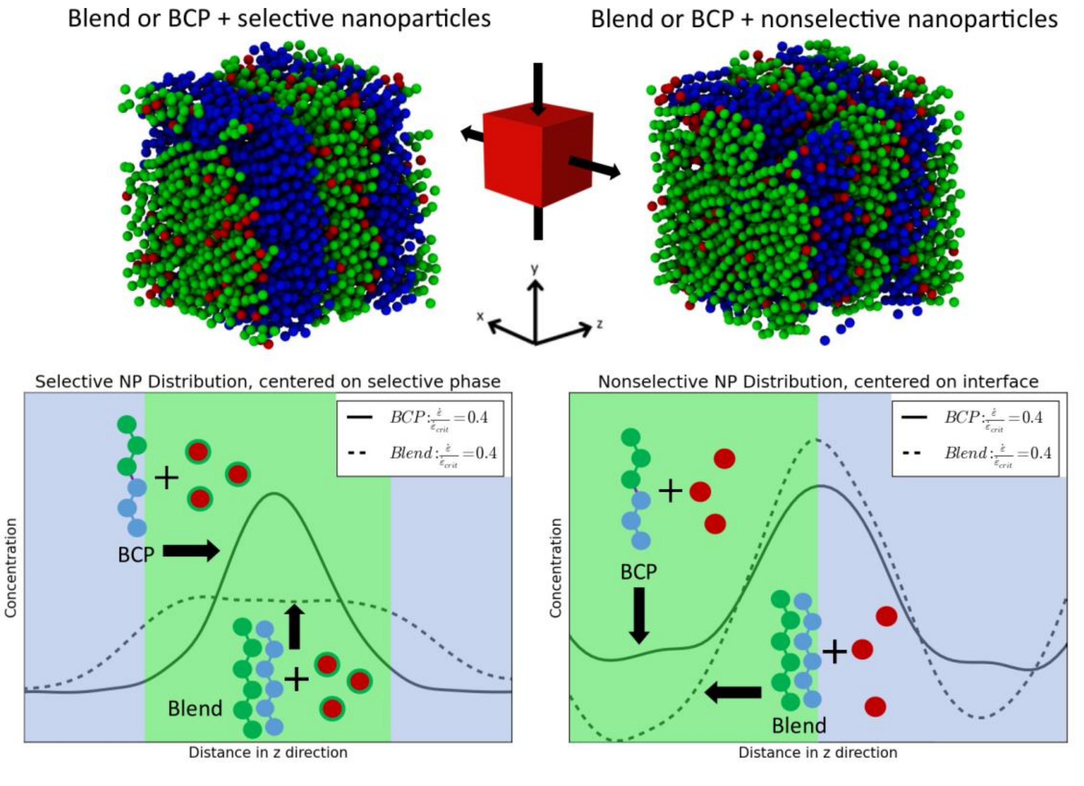

Abstract Figure Summary of key results from molecular dynamics simulations of immiscible polymers plus nanoparticles under planar elongational flow.[1]

2.1 Introduction

Nanocomposite materials have attracted great interest for their unique morphologies and improved thermal, mechanical, and electrical properties.[2,3,4] The degree of improvement in such properties depends on the alignment and dispersion of the nanofillers; for example, the thermal conductivity of a composite is maximized when carbon nanotubes (CNT) are aligned,[5] and electrical and mechanical properties improve when CNT are well dispersed.[6] In addition, good dispersion can result in materials with improved optical and mechanical properties with applications in optoelectronics and catalysis.[7,8] Nanofillers such as silica nanoparticles (NP), CNT, and graphene nanoribbons (GNR) tend to aggregate, so controlling the placement of nanofillers is a major challenge in their effective incorporation into composite materials. Placing NP at the interface between two phases can also lead to useful properties. For example, NP can serve as a binder between two materials that would otherwise phase separate, which has potential for fuel cell and battery applications.[9]

Nanocomposite materials can be fabricated by extensional flow, allowing the creation of fibers and sheets. A distinctive example process is electrospinning, which uses a powerful electric field to apply extensional strain rates of around 10000 s^{-1} on a polymer solution. This causes the polymer solution to extend into thin, high specific surface area fibers which are attractive for modern applications in separation, filtration, and sensing. [10–12] The extensional strain in this process both creates the nanoscale fibers and plays a role in the placement of nanoscale additives within the fibers.[13]

For complex polymer systems such as block copolymers (BCP), which are known to self-assemble into mesoscale phases like cylinders and lamellae, shear and strain also affect the morphology and alignment of the material.[14] The microstructures produced by self-assembly make these composites useful as templates for producing interesting nanostructured materials. For example, block copolymers can be used as “sacrificial” systems where one of the phases is removed by solvent, high temperature, or radiation. This leaves behind a mesoporous material that is applicable in membranes and battery separators. As an alternative to BCPs, which can be costly to synthesize, immiscible polymer blends may also have the potential to form ordered morphologies given the correct stimulus such as extensional strain.

The NPs in a self-assembled system can prefer one polymer type over another, or this result can be engineered by attaching ligands preferential to one polymer type. We will describe this type of NP as selective (S-NP). Alternatively, NPs may not prefer either phase or could have ligands attached that prefer both phases. These NPs will be described as nonselective (NS-NP). For the case of a “sacrificial” system, the NP should be selective towards the residual polymer to improve dispersion in the resulting material without losing its loading after the removal of sacrificial component.

The equilibrium placement of NP within a self-assembled structure is governed by thermodynamics. NP may be attracted to one phase or to each other, which corresponds to enthalpic benefits. In addition, there are enthalpic interactions between the self-assembled polymer phases which are affected by the presence of nanoparticles. Entropic considerations include the translational entropy of NP and the configurational entropy of polymer chains.[15] For selective NP in BCPs, it has been found that NP are pushed towards the center of the phase, where the polymer chain ends concentrate.[16] For nonselective NP, it might be predicted that the NP will disperse evenly through the material. However, experiments illustrate competing thermodynamic forces. Using BCP with gold NPs with ligands of both polymer types attached, Kramer found that NP tended to place at the interface of the phases.[9] These NP reduced the unfavourable enthalpic interactions between the polymer blocks at the phase interface and acted as a bridge between the two dissimilar phases, resulting in decreased segregation between the phases. Simulation results also support that the reduction of polymer phase contact is a driving force for nonselective NP placement.[17,18]

While BCP[14] and immiscible blend self-assembly and NP placement has been well-studied under equilibrium, there is less research into nonequilibrium conditions like extensional flow. This is in part due to the experimental challenges of studying systems with changing dimensions. Extensional deformation is of particular interest due to its use in the processing of polymer composites. The aforementioned electrospinning, as well as film molding and blow molding, subject polymer composites to high extensional deformation.[19] It is therefore valuable to understand the effect of extensional flow on the self-assembly morphology and the placement of NP. However, when conducting an experiment involving extensional deformation one encounters constantly shrinking and expanding dimensions. Eventually the shrinking dimension becomes too small, resulting in the end of the experiment. This makes it challenging to run the experiment long enough to reach steady state. Experimental methods that have been used to study polymer systems under extensional flow, such as melt extrusion and Taylor cells, can only maintain the extensional flow on a given polymer chain for a short time scale.[20,21]

Shear flow experiments, which are easier to conduct than extensional flow experiments, have identified steady-state morphologies for blend and BCP systems. Blended polymers have been found to show string-like phase separation,[22,23] and shear flow molecular dynamics simulations have shown similar string morphologies.[24] BCPs under shear flow has exhibited parallel and perpendicular lamellae for symmetric BCPs[25], and BCC and hexagonal cylinder morphology for asymmetric BCP.[26] Shear flow has also been shown to improve the alignment and uniformity of BCP thin films.[27,28] Molecular dynamics simulations of BCPs under shear flow have investigated the transition between the parallel and perpendicular morphologies[29,30] as well as the placement of NP within lamellar BCP domains.[17]

Under extensional flow, Kim *et al*. experimentally studied poly(styrene-co-acrylonitrile) blended with poly methyl methacrylate but was unable to reach steady state.[31] Lamellar diblock copolymer morphology under small strain has exhibited lamellae that align perpendicular to the flow direction.[32] Oriented microphase-separated triblock and diblock copolymers have also been studied experimentally using roll casting, which combines shear and elongational strains.[33] Triblock block copolymers self-assembly with clay nanoparticle additives have also been studied under elongational flow, and formed hexagonal cylindrical morphologies.[34] In polystyrene-talc composites, foaming behaviour was studied under extensional stresses and nucleation was found to improve for higher stress and larger talc particles.[35] However, it is difficult for these experiments to gain fundamental insights into the driving forces behind the particle placement due to their short time scales.

This work builds off the previous simulation work of Tran and Kalra, who simulated immiscible polymer blends without nanoparticles using the same approach as this paper.[36] They found that at low elongation rates, the blend arranges in a perpendicular separation morphology that consist of one phase of each polymer type. The "perpendicular" signifies that the normal of the interface is perpendicular to the neutral *z* axis, which undergoes neither expansion nor compression. At higher elongation rates, perpendicular lamellae are formed. Above elongation rates of 0.5 MD units (~10^9 s^{-1}), the polymer blend can no longer maintain self-assembly and appears as a disordered state. In the present work, we introduce selective and nonselective NP, which has not been previously simulated for an immiscible blend of polymers.

We also seek to compare the placement of NP in immiscible polymer blend to NP in BCP. Selective and nonselective NP have been previously simulated in BCP, and were found to concentrate at the phase center and interfaces respectively.[37] Comparing the immiscible blend to the BCP system allows us to better understand the effect of the polymer structure on the NP distribution and composite morphology.

2.2 Model and simulation details

2.2.1 Model

We used coarse-grained non-equilibrium molecular dynamics to study the effect of elongation on nanocomposite systems. In this paper, properties are listed in their reduced form, which is a non-dimensionalization of the real values using the fundamental constants of bead mass (m), Lennard-Jones energy ε, and Lennard-Jones bond length σ. These constants are set to unity so that the reduced values of temperature T, elongation rate $\dot{\varepsilon}$, and distance are represented in terms of combinations of mass, energy, and bond length. Polymers are modeled as bead-rod chains of ten beads while nanoparticles are modeled as a single bead. The bond length σ between consecutive polymer beads is fixed using the method of constraints described by Bruns *et al*.[38] Pair-wise potentials were not applied between neighboring beads in the same chain.

The coarse-grained beads interact with one other with pair-wise potentials. To simulate the two distinct polymer species, polymer chains consist of either *A*-type or *B*-type beads. Unfavorable *A*-*B* interactions are modeled by the Weeks-Chandler-Anderson (WCA) potential,[39]

$$u_1(r) = 4\varepsilon\left[\left(\frac{\sigma}{r}\right)^{12} - \left(\frac{\sigma}{r}\right)^{6}\right] + \varepsilon, \qquad r \leq 2^{\frac{1}{6}}$$

$$u_1(r) = 0, \quad r > 2^{\frac{1}{6}}$$

where *r* is the distance between two beads. The cutoff distance of $2^{\frac{1}{6}}$ eliminates the attractive portion of the function, resulting in a purely repulsive potential. *A*-*A* and *B*-*B* interactions are modeled by the full cut and shifted Lennard-Jones potential,

$$u_2(r) = 4\varepsilon\left[\left(\frac{\sigma}{r}\right)^{12} - \left(\frac{\sigma}{r}\right)^{6}\right] + \varepsilon, \qquad r \leq 2.5$$

$$u_2(r) = 0, \quad r > 2.5$$

Table 2.1 Model for polymer and NP interactions. NS refers to nonselective and S refers to selective.

Pair interactions	**Pair potential**
A : *A* , *B* : *B* *S*-NP : *S* -NP, *S* -NP : *A* *NS*-NP : *NS* -NP, *NS* -NP : *A* , *NS* -NP : *B*	Lennard-Jones, cutoff 2.5, shifted
A : *B* *S* -NP : *B*	Weeks-Chandler-Anderson

which captures the attraction between polymers of the same type. The cutoff of 2.5 reduces computation time by eliminating the low magnitude force calculations of beads far from each other. The term "shifted" refers to subtracting a constant from the function so that at 2.5 the value is zero. This avoids a discontinuity in the potential. This coarse-graining model bears similarities to more specific coarse-graining approaches, and could be considered to be a generalization of a PS-PMMA system.[40] To simulate BCP, the same interactions are used but the composition of the polymer differs. Instead of ten beads all of either type *A* or *B*, the BCP chains consist of five type *A* beads connected to five type B beads. With both systems, the difference in potential between polymer types causes self-assembly into *A* and *B* phases. The overall number of polymer chains, *A* beads, and *B* beads are identical in the blend and BCP systems. NPs interact with the polymer chains differently if they are selective or nonselective. For selective nanoparticles, S-NP:A and S-NP:S-NP pair interactions are modeled by u_2 and NP-B interactions are modeled by u_1. Therefore, by design it is more energetically favourable for *S*-NP to be near *A* beads compared to *B* beads. For *NS*-NP, all three interactions are modeled by u_2, meaning that *NS*-NP have no preference towards a particular type of polymer. A given simulation included only one type of NP: either selective (*S*-NP) or nonselective (*NS*-NP). The pair interactions are summarized in Table 2.1.

2.2.2 Simulation details

Table 2.2 Simulation parameters and estimated physical equivalents. MD units are defined as multiples of mass, bond energy, and bond distance.

Parameter	**Value (MD units)**	**Value (dimensional)**
Box length	16.76	N/A
Number of beads	4000	4000
Site density	0.85	0.85
Bead diameter	1	~1 nm
Temperature	1	~370 K
Elongation rate	0.001 – 1.0	~10^8 – 10^{11} s^{-1}
NP site fraction	0.05 – 0.4	0.05 – 0.4
Polymer aspect ratio	10	10
A-type bead: B-type bead	1:1	1:1
Timestep	0.005	~0.1 ps

Simulations were carried out in an initially cubic box with an isotropic initial state. The temperature was fixed at 1.0 reduced MD units using a Gaussian thermostat,[41] and the site density ρ was fixed at 0.85. A list of parameters used is given in Table 2. The timestep was chosen to be as large as possible while maintaining simulation stability, and the number of beads was selected to allow a reasonable simulation run time.

Planar elongational flow (PEF) with expansion in the x direction and compression in the y direction was implemented using the method described by Todd and Daivis.[41] This approach relies on work by Kraynik and Reinelt that found that a lattice rotated at 31.7° to the x direction exhibited temporal and spatial periodicity under PEF.[42] After a fixed Henky strain $\varepsilon_p = 0.9624$ the original lattice is reproduced. In terms of MD simulation, this allows the system boundaries to be rescaled to their original dimensions whenever ε_p is reached. When this occurs, particles are moved back into to the rescaled box using the periodic boundary conditions. Without this method, the simulation could not run beyond the time where the compressing dimension becomes smaller than the pair cutoff radius, preventing long-time simulations.

The lengths of the box in the x and y directions, L_x and L_y, change with time with the following equations,

$$L_x(t) = L_x(t = 0)\exp(\dot{\varepsilon}t)$$

$$L_y(t) = L_y(t = 0)\exp(-\dot{\varepsilon}t),$$

and are rescaled to their initial values when simulation time $t = \frac{n\varepsilon_p}{\dot{\varepsilon}}$ where n is an integer. Periodic boundary conditions were implemented according to the deforming brick scheme introduced by Todd and Daivis.[41]

Bead positions and velocities were calculated using the SLLOD equations of motion were used with a Gaussian thermostat,[43]

$$\frac{dr_{i,v}}{dt} = \frac{p_{i,v}}{m_v} + r_{j,v}\frac{du_i}{dx_j}$$

$$\frac{dp_{i,v}}{dt} = F_{i,v} - p_{j,v}\frac{du_i}{dx_j} - \alpha p_{i,v}$$

where $r_{i,v}$ is the position of the vth bead in the i direction, $p_{i,v}$ is the momentum, m_v is the mass, $F_{i,v}$ is the force, du_i/dx_j is the velocity gradient, and α is the Gaussian thermostat multiplier. For planar elongational flow,

$$\frac{du_i}{dx_j} = \begin{bmatrix} \dot{\varepsilon} & 0 & 0 \\ 0 & -\dot{\varepsilon} & 0 \\ 0 & 0 & 0 \end{bmatrix}$$

and

$$\alpha = \frac{\sum_v p_{i,v}\left[F_{i,v} - p_{j,v}\frac{du_i}{dx_j}\right]}{\sum_v p_{i,v}^2}.$$

The SLLOD equation, which incorporates PEF directly into the equations of motion, was integrated using a Velocity Verlet approach, a common numerical integration scheme with error $O(\Delta t^4)$. To prevent numerical errors from compounding, the total momenta was set to zero periodically.[44]

Our code was validated by comparing the pressure tensor to the results of Matin *et al*.[45] This information can be found in the appendix, in addition to results regarding simulation box size and nanoparticle diameter.

The simulations were run for 2x10^6 timesteps with a timestep of 0.005. By this point, properties such as pressure and potential energy have reached a constant value demonstrating that the system had reached steady state.

2.3 Results and Discussion

2.3.1 Morphology of BCP and blend systems

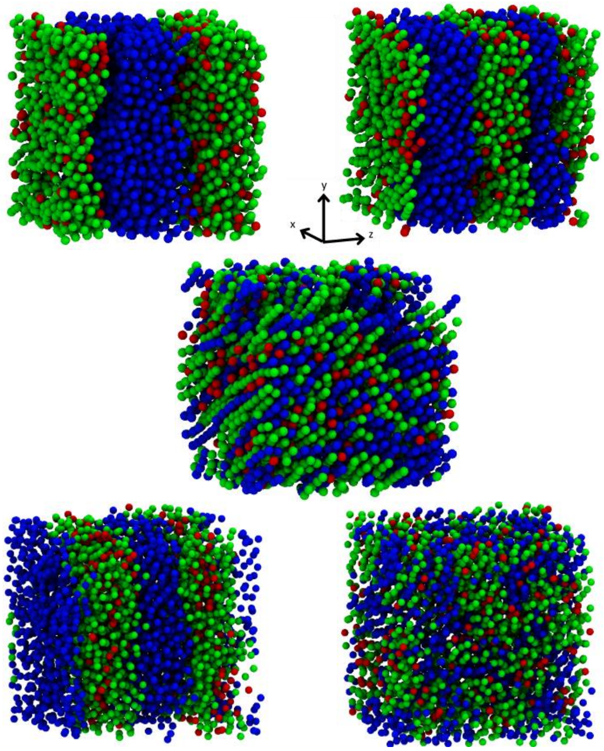

Figure 2.1: Visualizations of blend/S-NP and BCP/S-NP morphologies. green: polymer A, blue: polymer B, red: S-NP. Top left: blend/S-NP perpendicular separation, Top right: blend/S-NP perpendicular lamellae, Middle: blend/S-NP disordered, Bottom left: BCP/S-NP perpendicular lamellae, Bottom right: BCP/S-NP disordered.

Figure 2.1 shows snapshots of Blend/*S*-NP and BCP/*S*-NP with 10% NP concentration to illustrate the different self-assembly morphologies observed under PEF. Visualizations were produced using the Visual Molecular Dynamics software.[46] Table 3 shows morphology transition strain rates, which are the elongation rate at which the morphology changes from perpendicular separation to perpendicular lamellae or perpendicular lamellae to disordered. At elongation rates typically lower than 0.05 MD units, the blend system self-assembles into a perpendicular separation morphology. The perpendicular designation indicates that the normal of the phase interface is perpendicular to the z-axis. At elongation rates typically between 0.05 and 0.5, the composite shows a perpendicular lamellae morphology, forming two pairs of lamellae. With a box length of 16.76, these lamellae have an average width of 4.19. Above an elongation rate of 0.5, the system enters a disordered phase where discrete phases are no longer observed. For the BCP system, only the transition between perpendicular separation and disordered is observed. These morphologies closely follow those simulated for the case of a blend without NP.[36]

For BCPs, the self-assembly is caused by the chemical bonds between the unlike polymer types. For the blend, which has no connection between chains of different types, it is clear that in the absence of flow the polymers would fully phase separate. However, strong elongational flow can result in the formation of a metastable perpendicular lamellae morphology instead of full phase separation. The strong flow prevents the full phase separation of the blend by effectively confining the local regions of polymer into lamellae that are aligned to the flow direction and unable to come into contact with each other. This is supported by the full phase separation observed at low elongation rates, where the convection effect is not strong enough to prevent the contact and coalescence of blend lamellae. In addition, if a perpendicular separation starting state is used instead of an isotropic starting state, perpendicular lamellae did not form and the perpendicular separation morphology was found to persist until the order-disorder transition elongation rate. For flow rates near perpendicular separation – perpendicular lamellae transition, some blend simulations showed perpendicular lamellae structure initially before collapsing into perpendicular separation.

Table 2.3 Elongation rates of perpendicular separation-perpendicular lamellae transition and perpendicular lamellae-disordered transition for various systems.

System	**Sep-Lam transition elongation rate**	**Lam-disorder transition elongation rate**
Blend	0.05	1.0
Blend/*S*-NP: 10%	0.06	0.5
BCP/*S*-NP: 10%	Does not exist	0.025
Blend/*NS*-NP: 10%	0.06	0.5
Blend/*NS*-NP: 40%	<0.005	<0.4
BCP/*NS*-NP: 10%	Does not exist	0.02
BCP/*NS*-NP: 20%	Does not exist	0.01
BCP/*NS*-NP: 40%	Does not exist	<0.005

Table 2.4 *x*,*y*, and *z* components of the average polymer end-to-end vector.

Simulation	***x***	***y***	***z***
Blend, $\dot{\varepsilon}$=0.01	6.24	2.10	2.62
Blend, $\dot{\varepsilon}$=0.06	7.5	2.0	2.1
Blend, $\dot{\varepsilon}$=0.1	7.9	2.0	1.9
BCP, $\dot{\varepsilon}$=0.005	4.83	2.03	4.78
BCP, $\dot{\varepsilon}$=0.01	5.28	2.04	4.53
BCP, $\dot{\varepsilon}$=0.015	5.59	2.1	3.68

For the BCP/*S*-NP and BCP/*NS*-NP systems, a perpendicular lamellae morphology is observed below elongation rates of around 0.025 MD units, and a disordered morphology is observed above that point. In this case, the perpendicular lamellae morphology is a stable state which is caused by the bond between polymer *A* and *B* present in the BCP polymer.

Comparing the morphology transitions for the BCP and blend systems, it can be seen that the constraints imposed by the BCP structure cause a less stable structure in the presence of PEF. In BCP, two phases must be chemically bound at their interface, while in blend, the two phases move easily with respect to each other. As a result, the blend system can much more easily accommodate the strain created by PEF, resulting in a much higher perpendicular lamellae-disorder transition rate (0.5) than in BCP (0.025). The chemical bond across the phase interface also prevents the BCP system from exhibiting the perpendicular separation phase observed in the blend system.

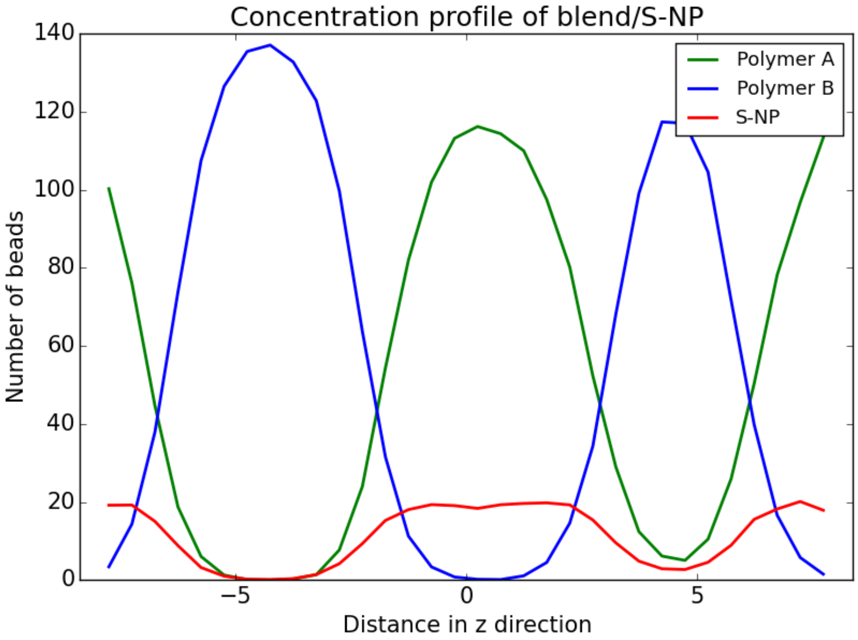

Figure 2.2 Time-averaged blend/S-NP concentration profile of the three bead types for elongation rate = 0.1 and 10% S-NP concentration.

The differences in morphology transition raise issues in comparing the BCP/*S*-NP system to the blend/*S*-NP system because at a given elongation rate, the systems have different morphology. For example, at an elongation rate of 0.01, the BCP system is in a perpendicular lamellae phase while the blend system is in a perpendicular separation phase. This means that the phase widths are not equal for the two systems at the same elongation rate. To address this, we will make two different comparisons between the blend/*S*-NP and BCP/*S*-NP systems: one where the morphology is the same and one where the elongation rate is the same. For the elongation rate comparison, we normalize by the phase width.

2.3.2 Selective Nanoparticles (*S*-NP) Distribution in Blend and BCP

Figure 2.2 shows the distribution of *S*-NP, polymer *A*, and polymer *B* for the perpendicular lamellae phase. The polymer distribution shapes were found to be similar to those observed by Tran and Kalra.[36] The lack of a rectangular shape of the A and B concentrations is attributed to the slight movement and distortions of the interface as the simulation progresses. As expected, *S*-NP tend to place within the

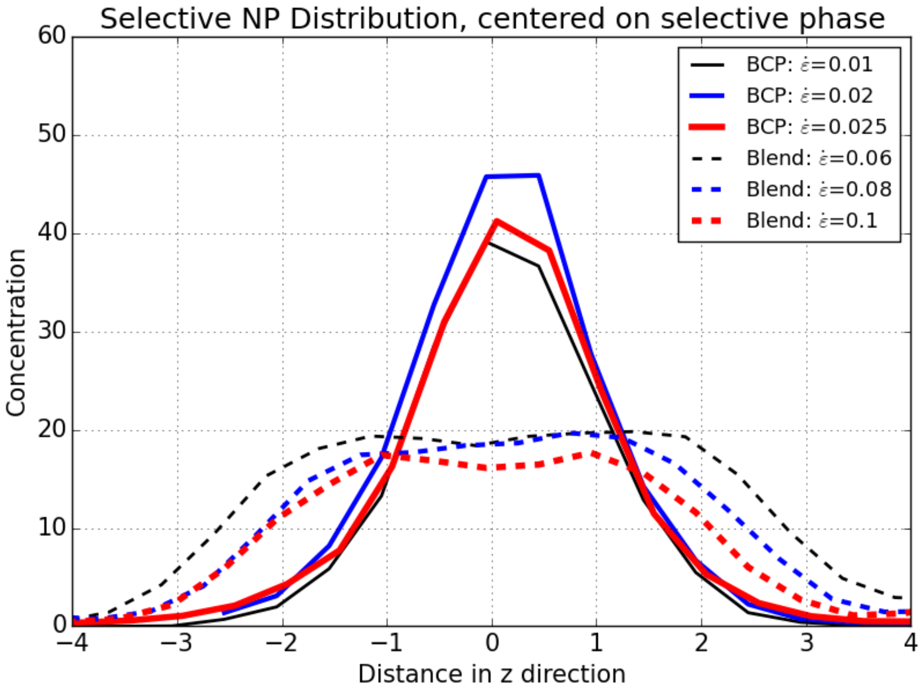

Figure 2.3 Concentration profile of S-NP for BCP/S-NP and blend/S-NP systems and varying elongation rates. The graph is centered on the selective phase so that 0 on the z axis is the center of the selective phase. Overall S-NP concentration is 10%.

polymer phase they are selective towards, polymer *A*. This results in a swelling of the *A* phase compared to the *B* phase. We can also note that NP distribution is relatively flat and well-distributed within the selective phase. Comparing blend to BCP, Figure 2.3 shows that for increasing elongation rate but maintaining the perpendicular lamellae phase there is no change in the *S*-NP distribution. This can be understood by considering the effect of PEF on the polymer and the S-NP. For the polymer, PEF is expected to orient and stretch the polymer chains so that they are pointing along the expansive (*x*) direction and perpendicular to the compressive (*y*) direction. However, we can see from Table 2.4 that the blended polymers are already well aligned to the flow direction, as they have a large x-component and small y and z-components of the end-to-end vector. This means that the surroundings polymers are not changing significantly with elongation rate. For the NP, PEF is expected to disperse the NP. Since the NP are already well dispersed at lower elongation rates, the increase in elongation rate does not affect the distribution.

Figure 2.3 also shows that the *S*-NP in BCP concentrate at the center of the selective phase while the *S*-NP in blend do not. For BCP/S-NP, it has been found previously that S-NP concentrate at the center of the selective phase,[37] which is also found here. The difference in placement between the blend and BCP *S*-NP can be understood by examining the location of the polymer chain ends, shown in Figure 2.4.

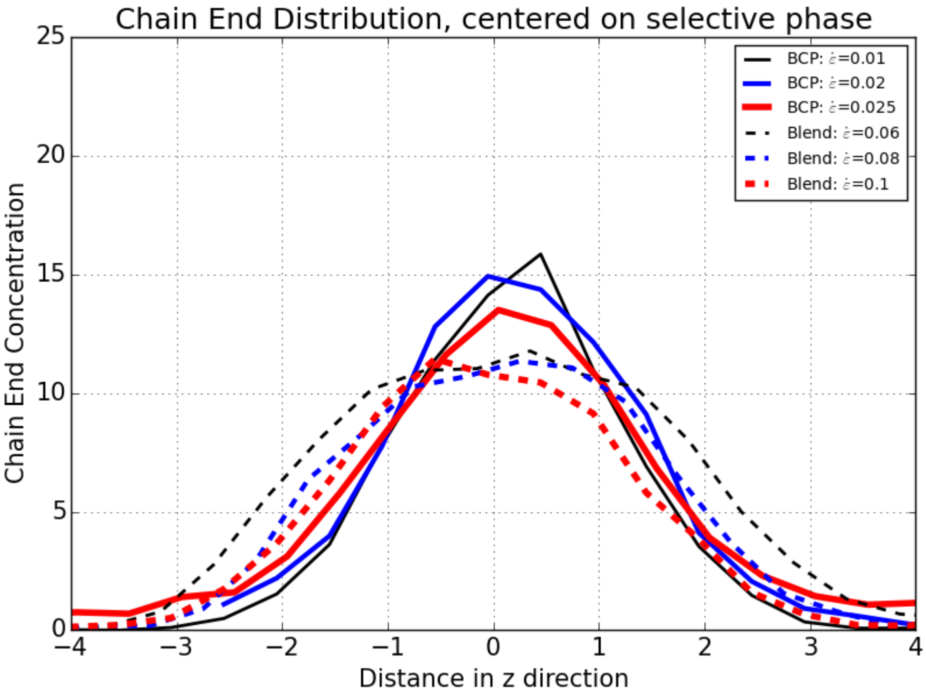

Figure 2.4 Concentration profile of polymer chain ends for BCP/S-NP and blend/S-NP for varying elongation rates. The graph is centered on the selective phase so that 0 on the z axis is the center of the selective phase. S-NP concentration is 10%.

For the BCP, the chain ends lie in the middle of a phase, while the phase boundary is at the center of the chain where the polymer type changes. This leads microstates where S-NP lie near the chain ends to be entropically favourable, encouraging the placement of S-NP there.[17,37,47] The average orientation of the BCP chains is listed in Table 2.4. They have a relatively large *z*-direction component, which is required for the BCP to be able to from lamellae. The BCP chains need to extend somewhat in the *z* direction so that they cross between two lamellae. However, PEF tries to force the chains into the x direction. Therefore, for the BCP system the chain orientation encouraged by PEF is working against the orientation needed for self-assembly. As the elongation rate increases, the BCP chains are forced more into the *x* direction and their *z* component is reduced. Once the *z* component is too small, it is impossible to form lamellae and a disordered phase is observed in the simulation, occurring at an elongation rate of 0.25.

Table 2.5 Average S-NP distance from the selective phase center for BCP and blend systems. The normalized distance is divided by the phase width. NP concentration is 10%. P. lam: perpendicular lamellae, P. sep: perpendicular separation

Polymer Type	**Elongation Rate**	**Phase**	**Avg. NP distance**	**Normalized NP distance**
BCP	0.01	P. lam	0.713	0.323
BCP	0.02	P. lam	0.739	0.330
BCP	0.025	P. lam	0.780	0.363
Blend	0.01	P. sep	2.34	0.525
Blend	0.02	P. sep	2.34	0.523
Blend	0.025	P. sep	2.31	0.515
Blend	0.06	P. lam	1.39	0.65
Blend	0.08	P. lam	1.42	0.665
Blend	0.1	P. lam	1.41	0.65

For the polymer blend system, chain ends have no driving force to lie in the center of a phase because the immiscible polymers are no longer bonded. This is reflected in Figure 2.4. Since their chain ends are evenly distributed, NP are expected to be more spread out through the phase, which is the result obtained in Figure 2.3. We can see that the surrounding polymer allows a degree of control over the *S*-NP placement: the blend/*S*-NP leads to more dispersed S-NP than the BCP/S-NP system when both systems are in the same phase.

To further support this conclusion, the BCP/*S*-NP and blend/*S*-NP systems are compared for the same elongation rates. For elongation rates 0.01-0.025, the BCP and blend systems show different morphologies. Therefore, we calculated the average distance of *S*-NP within the selective phase from the center of the phase. Shown in Table 2.5, the perpendicular separation blend shows much larger average NP distance than the perpendicular lamellae blend due to the much larger phase width. When the average NP distance is normalized by the phase width, both the low and high elongation rate blend/*S*-NP normalized distances are significantly higher than the BCP/*S*-NP normalized distance. This supports the conclusion drawn in Figure 2.3 that the blend system leads to significantly improved *S*-NP dispersion within the selective phase.

2.3.3 Effect of S-NP concentration

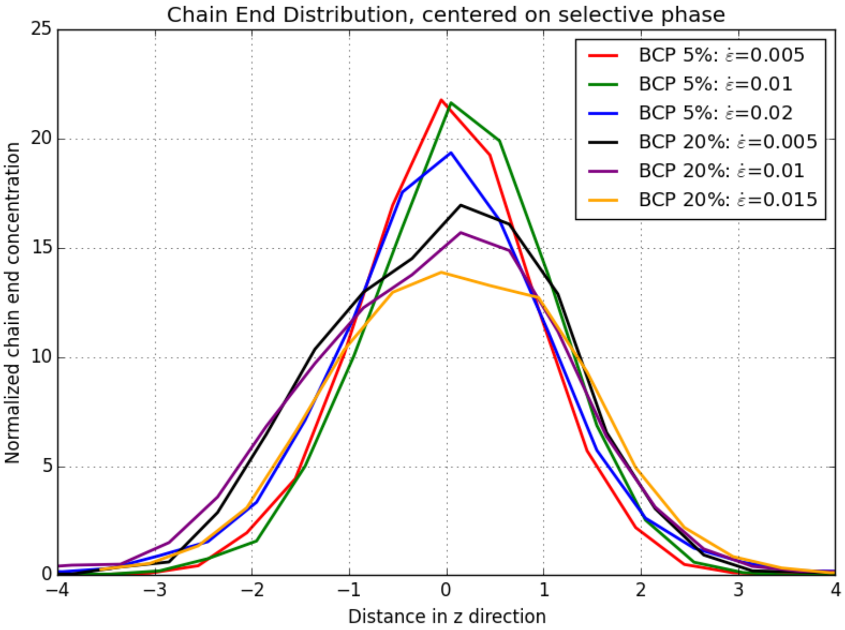

Figure 2.5 Chain end concentration for BCP/S-NP for varying NP concentration and elongation rate. The concentrations were normalized by the total number of chain ends.

Previous discussion of *S*-NP has limited the *S*-NP concentration to 10%. For 5% and 20% concentrations, we found that the *S*-NP similarly placed in the center of the selective phase for BCP, and distributed throughout the phase for blend. In addition, similar to the 10% case, the distributions were not affected by increasing elongation rate while maintaining the perpendicular lamellar morphology. Examining the normalized polymer chain end distribution for BCP/*S*-NP, shown in Figure 2.5, shows that at higher NP concentrations, the NP placing at the center of the selective phase are displacing the polymer chain ends, resulting in a broader polymer chain end distribution. In addition, as elongation rate increases the polymer chains are forced to align more towards the *x* direction, resulting in a slightly lower chain end distribution at the center. As for the 10% case, the blend polymer chain ends did not concentrate at the center of the phase, instead orienting along the x direction.

2.3.4 Nonselective Nanoparticle (*NS*-NP) distribution in Blend and BCP

NS-NP were found to concentrate at the phase boundary for both blend and BCP systems, shown in Figure 2.6. Instead of the chain end placement as a driving force for NP distribution, as seen for *S*-NP, the *NS*-NP placement is motivated by a reduction in the unfavourable interactions between the two phases. Figure 2.6 shows that for blend/*NS*-NP, elongation rate does not affect the *NS*-NP distribution. This is due to the unbound nature of the blend interface which allows the interface to easily adjust to increasing strain. The BCP system, with its bonded interface, cannot adjust so easily to the elongational strain.

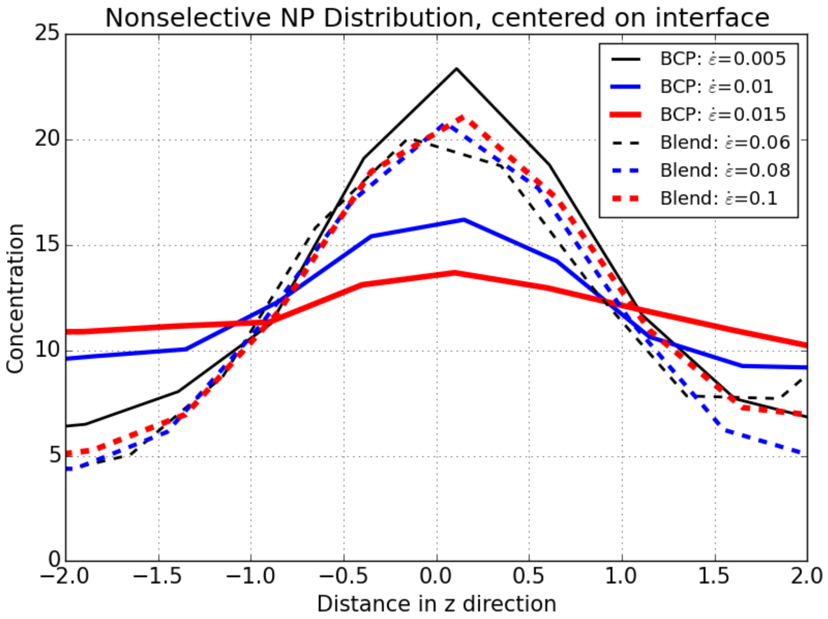

Figure 2.6 Concentration profile of NS-NP for BCP/NS-NP and blend/NS-NP for varying elongation rates. The graph is centered on the interface between the two polymer phases, which is set to 0 on the z axis. NS-NP concentration is 10%. Elongation rates are selected to create perpendicular lamellae structure for both BCP and blend.

At an elongation rate of 0.005, the BCP/NS-NP distribution is similar to the distribution for the blend/*NS*-NP system, showing that far from the critical elongation rate the difference in interface plays a minor role in NS-NP distribution. However, as the elongation rate increases closer to the order-disorder transition at 0.02, the BCP chains face increasing force to align towards the flow direction and become less able to maintain an even, discrete interface. This results in a broadening of the *NS*-NP distribution corresponding to the coarsening of the interface. This is supported by Table 4, which shows that at an elongation rate of 0.015 the average *z* direction length is 3.68. To have two pairs of lamellae in box size of 16.67, we would expect an average phase width of 4.17. The smaller *z* component indicates that the BCP chains are struggling to maintain the interface, which leads to a wider *NS*-NP distribution.

Figure 2.7 shows again that BCP chain ends concentrate at the center of the phase while blend chain ends are more evenly distributed. However, in comparing the BCP/*NS*-NP chain ends to the BCP/*S*-NP chain ends in Figure 2.4, the BCP/*NS*-NP show a much sharper decrease in the peak value as elongation rate increases.

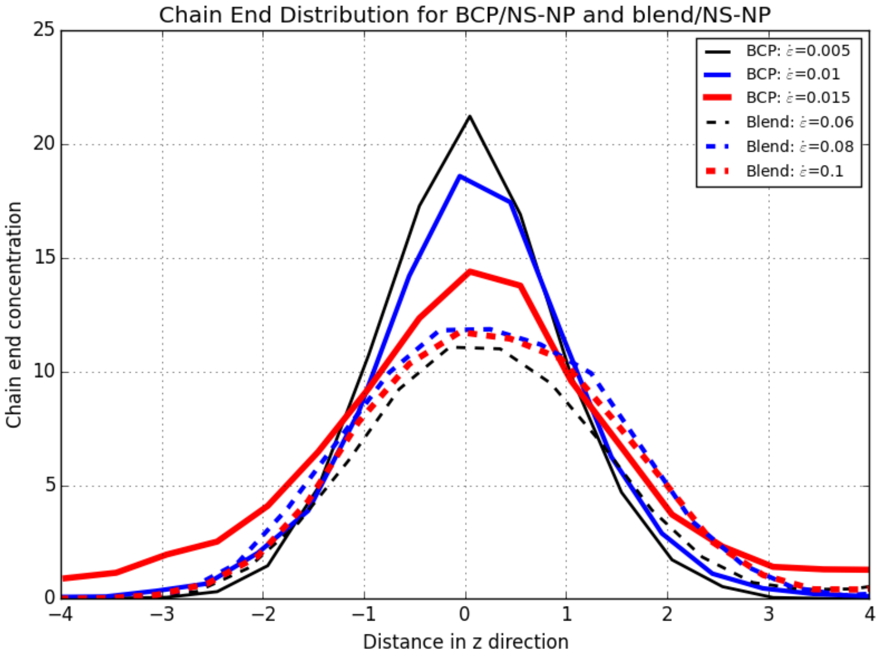

Figure 2.7 Concentration profile of polymer chain ends for BCP/NS-NP and blend/NS-NP for varying elongation rates. The graph is centered so that 0 on the z axis is the center of one of the polymer phases. NS-NP concentration is 10%.

This is due to a “crowding out” effect of the *S*-NP that limits the number of chain ends that can place at the center of the phase. The BCP/*NS*-NP, which has no NP placed in the center, can easily concentrate it chain ends at the center of the phase. Then, higher elongation rates force the chains to reorient towards the flow direction, moving some of the chain ends away from the center.

2.3.5 Effect of *NS*-NP concentration

As the *NS*-NP reduce interfacial energy by placing between the two phases and preventing polymer interaction, we can expect that higher concentrations will lower the interfacial energy further. This is shown quantitatively in Table 6 by measuring the pairwise interaction energy between the two polymer types near the interface. For the 10% concentration, the energy is not much lower than the reference S-NP case, showing that the interface is only partially screened by the *NS*-NP. At higher concentrations, the energy drops significantly as the two polymer phases are prevented from interacting with each other by the *NS*-NP.

Table 2.6 Interfacial energies for varying NP concentration and type. All cases are for the polymer blend at an elongation rate of 0.08.

NP type	**NP concentration**	**Interfacial energy**
NS-NP	10%	13.29
NS-NP	20%	6.85
NS-NP	40%	4.82
S-NP	10%	14.87

This screening effect stabilizes morphologies with more interface surface area. To examine this, we first compare the order-disorder transition elongation rates for varying concentrations in Table 2.3. For both BCP/*NS*-NP and blend/*NS*-NP, increasing concentration of NS-NP decreases the order-disorder transition. The disordered phase, which in the absence *NS*-NP has large unfavourable interactions between the A and B phases, becomes much more energetically favourable when increased amounts of screening *NS*-NP are present. The blend system is found to handle increased loading better than the BCP system, as it was able to form ordered phases at a concentration of 40% while the BCP system could not. The BCP system effectively has a limited amount of space at its interface for NS-NP to place due to its inability to phase separate. As a result, at high loading *NS*-NP must place elsewhere in the phases, decreasing the selectivity of the phases.

The *NS*-NP also prevent the formation of a perpendicular separation phase for blend/*NS*-NP at a concentration of 40%, listed in Table 2.3. With so many *NS*-NP, the NP can saturate four interfaces as easily as two, making the interfacial energy difference between the perpendicular lamellae and perpendicular separation phases negligible. This is illustrated in Figure 2.8. The increased entropy of the perpendicular lamellae phase causes it to be preferential in this situation. The high concentration of NP at the interface also stabilizes the perpendicular lamellae in the polymer blend by

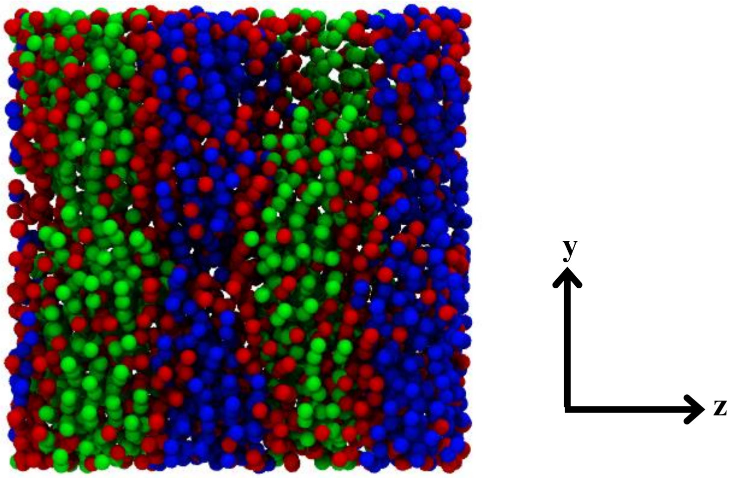

Figure 2.8 Snapshot of 40% concentration blend/NS-NP for elongation rate = 0.01. The high concentration of NP results in the interface saturating with NP, increasing the stability of the perpendicular lamellae at lower elongation rates.

preventing contact between lamellae of the same polymer type.

2.4 Conclusion

Using molecular dynamics, we have studied the effect of planar elongation flow on immiscible polymer blend/NP composites and compared the NP dispersion and morphology to the block copolymer analogue. For selective NP, the blend system showed much better dispersion of the NP throughout the selective phase than the BCP system. For nonselective NP, both blend and BCP systems showed similar concentrations at the interface, but the blend system was able handle higher NP loading. In general, the blend system allows a greater range of elongation rates and more possible morphologies, a potential advantage for processing. The main difference between the BCP and blend systems, namely the presence of a chemical bond across the phase interface, explains the difference in both NP distribution and morphology transitions. Overall, the strength of elongational flow had little effect on the NP distribution for the blend case beyond controlling the self-assembly morphology. For the BCP case, the strength of the flow played a larger role, especially for the nonselective case. This difference was found to be a result of the BCP chains desiring to orient in the non-flow (z) direction to maintain the self-assembly morphology, while the blend chains were able to orient in the flow direction independent of their morphology.

2.5 Supplemental information

2.5.1 Effect of system size

In the main text, all simulations were conducted with a simulation box length of 16.76. Simulations with larger box lengths revealed that the number of lamellae and the morphology transitions points change somewhat but also that the NP placement observed using the smaller box size continues to hold.

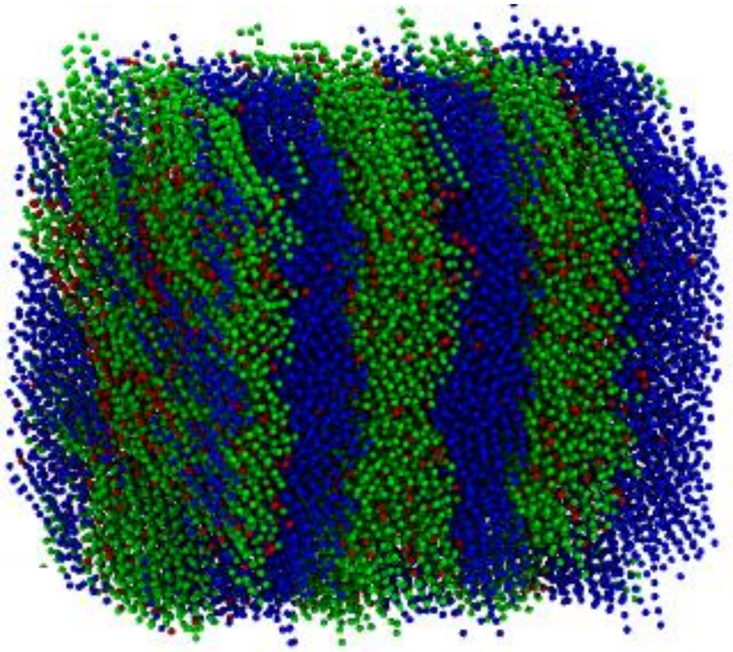

Figure 2.9 Visualization for elongation rate = 0.1, box length = 36, S-NP in blend.

Table 2.7 Number of lamellae phase pairs observed for different conditions and the width of lamellae observed. The highlighted row corresponds to the simulation shown in Figure 2.9.

Box length	**El. Rate**	**Number of lamellae pairs**	**Phase width**
17	.03	1	8.4
17	.1	2	4.19
26	.03	2	6.5
26	.1	2	6.5
36	.03	2	9
36	.1	3	6

Table 2.7 shows that the phase width in the neutral flow direction and the number of lamellae vary with the box length. This is apparent in Figure 2.9, which shows 3 phase pairs, in contrast to the images shown in the main text. With the box length of 16.76, it was not possible to observe 3 phase pairs due to the limited repeating box size. Despite the fully periodic nature of the simulation, the box length thus acts as an artificial constraint due to the requirement that the box length by an integer multiple of the phase. Therefore, with larger box lengths, this issue is reduced and the system approaches its unconstrained state. To fully eliminate this effect very large box sizes would be needed. Due to the comparative nature of the study, it is not expected that eliminating the box size effect would change the conclusions regarding the NP distribution and NP effect on morphology transitions.

2.5.2 Effect of chain length

Polymers with chain lengths of 20 (as opposed to 10 used in the main text) were simulated without changing the simulation box size but ordered self-assembly was not achieved. This is due to the much larger box size and time scale that would be needed for self-assembly to occur. These larger systems were not investigated due to increasing computational requirements. At the smaller box sizes there was not enough space to accommodate the larger chains and phase widths.

Polymer chain lengths of 5 were also simulated for the blend system. By reducing from a length of 10 to 5, the perpendicular separation to perpendicular lamellae morphology transition was pushed to a higher elongation rate. This is due to the improved diffusion of the shorter chains, which requires a higher elongation rate to prevent the coalescence of lamellae into the perpendicular separation morphology.

2.5.3 Effect of temperature annealing on the polymer blend

After elongational flow ended, simulations were run without flow at high temperatures to investigate the effect of post-processing high temperature annealing. It was found that with sufficient temperature (T = 3 MD units) the perpendicular lamellae phase could revert back to a perpendicular separation phase. This supports that the perpendicular separation phase is a lower energy state due to its smaller interface area and that the perpendicular lamellae can collapse into perpendicular separation given fast enough diffusion.

2.5.4 Validation details

As validation, the trace of the pressure tensor and the total potential energies found from our molecular dynamics code were compared to those published by Matin, Daivis, and Todd, *J. Chem. Phys.* 113 9122 for a one-site LJ fluid. The trace of the pressure tensor was calculated according to the method used in the reference.

Table 2.8 Validation details for the elongational molecular dynamics code.

Elongation rate	**Tr(P) (this work)**	**Tr(P) (Matin)**	**Total potential energy (this work)**	**Total potential energy (Matin)**
0.01	7.89	7.85	622	627
0.02	7.88	7.86	632	627
0.05	7.75	7.87	629	627
0.1	7.86	7.89	630	628

2.5.5 Effect of nanoparticle diameter

For the BCP system, S-NP with diameters of 0.7 and 2.0 were simulated and compared to the diameter 1.0 NP used elsewhere in the paper. The NP volume concentration was kept constant at 10% for the different diameters. The distributions of the S-NP in BCP were found to be similar for the tested diameters, shown in Figure 2.10. This is in agreement with the simulations results of Schulz, Hall, and Genzer, *Macromolecules* 38 3007, who studied a similar system under equilibrium (no flow) conditions.

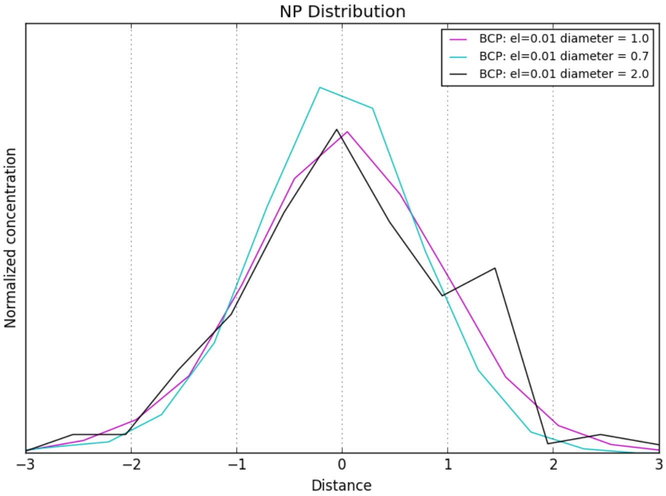

Figure 2.10 S-NP concentration in BCP for varying S-NP diameter. The elongation rate was kept constant at 0.01 and the S-NP volume concentration was fixed at 10%.

For the blend system, shown in Figure 2.11, the change in diameter of S-NP had a pronounced effect on their placement and the system morphology. The 2.0 diameter S-NP placed at the interface instead of throughout the selective phase, likely due to entropic benefits of placing in the uncrowded interface area. The 0.7 diameter had a slightly more narrowed concentration, which was also observed for the blend case.

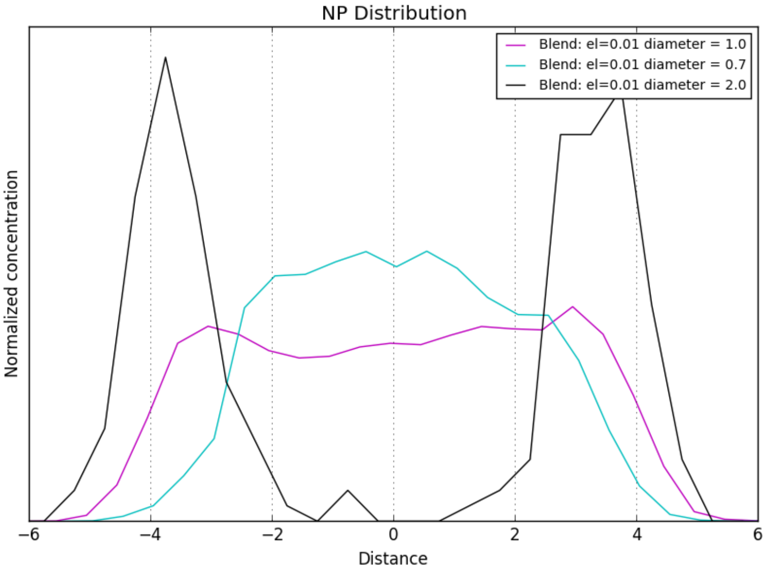

Figure 2.11 S-NP concentration in blend for varying S-NP diameter. The elongation rate was kept constant at 0.01 and the S-NP volume concentration was fixed at 10%.

2.5.6 Application of model to electrospun nanocomposites

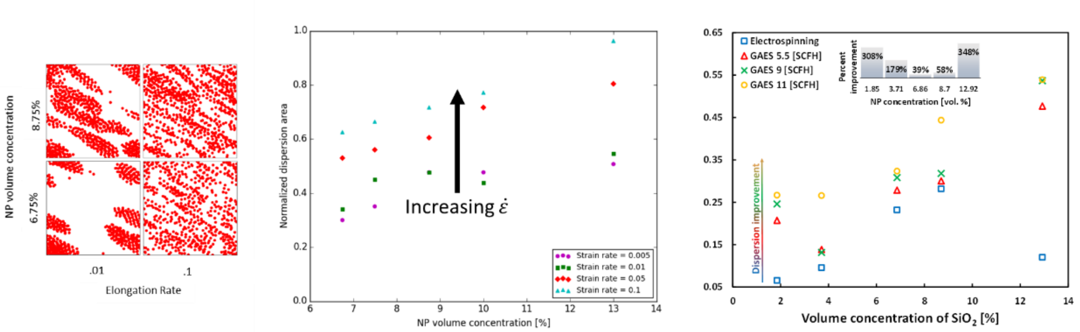

Simulation visualization (polymer blanked)

Simulation dispersion results

Experimental results from electrospun polyvinyl alcohol fibers with SiO_2 NP

Figure 2.12 Comparison of simulation and experimental electrospinning results for a homopolymer system with nanoparticles. Higher dispersion area corresponds to better dispersion. Experimental results from Dr. Yevgen Zhmayev.[48]

Figure 2.12, leftmost figure, shows visualizations of planar elongational simulations with a single polymer type plus nanoparticles. Multiple nanoparticle concentrations and planar elongational strain rates were simulated. In the rightmost figure, polyvinyl alcohol nanofibers were electrospun with silica nanoparticles. The strain rate was adjusted by varying the flow rate of a concentric air sheath around the electrospinning nozzle. Then, the proportion of the image filled with nanoparticles in transmission electron microscope images was calculated as the dispersion area. If nanoparticles are well dispersed, they will occupy a large area in the image and yield a high dispersion area. This analysis method was also used in simulation to compare to experiment. Both experiment and simulation show the same qualitative trends that higher strain rates and higher NP concentration yield better dispersion. From the simulation, this behavior is due to a reduction in NP diffusion when polymer chains align to the flow direction at higher strain rates.

2.6 References

1. Shebert, G. L. & Joo, Y. L. Effect of elongational flow on immiscible polymer blend/nanoparticle composites: A molecular dynamics study. *Soft Matter* **12**, 6132–6140 (2016).

2. Balazs, A. C., Emrick, T. & Russell, T. P. Nanoparticle polymer composites: where two small worlds meet. *Science.* **314**, 1107–1110 (2006).

3. Bockstaller, M. R., Mickiewicz, R. A. & Thomas, E. L. Block copolymer nanocomposites: Perspectives for tailored functional materials. *Adv. Mater.* **17**, 1331–1349 (2005).

4. Buxton, G. A. & Balazs, A. C. Simulating the morphology and mechanical

properties of filled diblock copolymers. *Phys. Rev. E. Stat. Nonlin. Soft Matter Phys.* **67**, 031802–031814 (2003).

5. Huang, H., Liu, C., Wu, Y. & Fan, S. Aligned carbon nanotube composite films for thermal management. *Adv. Mater.* **17**, 1652–1656 (2005).
6. Liao, S. *et al.* Preparation and properties of carbon nanotube/polypropylene nanocomposite bipolar plates for polymer electrolyte membrane fuel cells. *J. Power Sources* **185**, 1225–1232 (2008).
7. Pryamitsyn, V. & Ganesan, V. Strong segregation theory of block copolymer-nanoparticle composites. *Macromolecules* **39**, 8499–8510 (2006).
8. Shenhar, R., Norsten, T. B. & Rotello, V. M. Polymer-Mediated Nanoparticle Assembly: Structural Control and Applications. *Adv. Mater.* **17**, 657–669 (2005).
9. Kim, B. J., Fredrickson, G. H., Hawker, C. J. & Kramer, E. J. Nanoparticle surfactants as a route to bicontinuous block copolymer morphologies. *Langmuir* **23**, 7804–9 (2007).
10. Kalra, V. *et al.* Confined assembly in coaxially electrospun block-copolymer fibers. *Adv. Mater.* **18**, 3299–3303 (2006).
11. Kapllani, A., Tran, C. & Kalra, V. Self-assembly of fully conjugated rod–rod diblock copolymers within nanofibers. *Soft Matter* **9**, 11014 (2013).
12. Greenfeld, I. & Zussman, E. Polymer entanglement loss in extensional flow: Evidence from electrospun short nanofibers. *J. Polym. Sci. Part B Polym. Phys.*

51, 1377–1391 (2013).

13. Park, J. H. & Joo, Y. L. Tailoring nanorod alignment in a polymer matrix by elongational flow under confinement: simulation, experiments, and surface enhanced Raman scattering application. *Soft Matter* 3494–3505 (2014). doi:10.1039/c4sm00096j

14. Park, C., Yoon, J. & Thomas, E. L. Enabling nanotechnology with self assembled block copolymer patterns. *Polymer.* **44**, 6725–6760 (2003).

15. Thompson, R. B., Ginzburg, V. V., Matsen, M. W. & Balazs, A. C. Predicting the Mesophases of Composites. *Science.* **292**, 2469–2473 (2001).

16. Chiu, J. J., Kim, B. J., Kramer, E. J. & Pine, D. J. Control of nanoparticle location in block copolymers. *J. Am. Chem. Soc.* **127**, 5036–5037 (2005).

17. Kalra, V., Mendez, S., Escobedo, F. & Joo, Y. L. Coarse-grained molecular dynamics simulation on the placement of nanoparticles within symmetric diblock copolymers under shear flow. *J. Chem. Phys.* **128**, 1–11 (2008).

18. Stratford, K., Adhikari, R., Pagonabarraga, I., Desplat, J.-C. & Cates, M. E. Colloidal jamming at interfaces: a route to fluid-bicontinuous gels. *Science.* **309**, 2198–2201 (2005).

19. Kalra, V. *et al.* Self-Assembled Structures in Electrospun Poly (styrene-b lock-isoprene) Fibers. *Macromolecules* **39**, 5453–5457 (2006).

20. Anne-Archard, D., d'Olce, M., Tourbin, M. & Frances, C. Aggregation of silica nanoparticles in concentrated suspensions under turbulent, shear and

extensional flows. *Chem. Eng. Sci.* **95**, 184–193 (2013).

21. Huitrón-Rattinger, E. & Romo-Uribe, A. Shear and extensional rheometry of PA6 reinforced with polyacrylic nanoparticles. *Polym. Bull.* **70**, 2547–2567 (2013).

22. Hasimoto, T., Matsuzaka, K. & Moses, E. String Phase in Phase-Separating Fluids under Shear Flow. *Phys. Rev. Lett.* **74**, 126–129 (1995).

23. Hobbie, E., Kim, S. & Han, C. Stringlike patterns in critical polymer mixtures under steady shear flow. *Phys. Rev. E* **54**, R5909–R5912 (1996).

24. Luo, K., Zhang, H. & Yang, Y. The chain stretching effect on the morphology and rheological properties of phase-separating polymer blends subjected to simple shear flow. *Macromol. Theory Simulations* **13**, 335–344 (2004).

25. Kannan, R. M. & Kornfield, J. A. Evolution of Microstructure and Viscoelastic during Flow Alignment of a Lamellar Diblock Copolymer. *Macromolecules* **27**, 1177–1186 (1994).

26. Koppi, K. A., Tirell, M. & Bates, F. S. Epitaxial growth and shearing of the body centered cubic phase in diblock copolymer melts. *J. Rheol. (N. Y. N. Y).* **38**, 999 (1994).

27. Angelescu, D. E., Waller, J. H., Register, R. A. & Chaikin, P. M. Shear-induced alignment in thin films of spherical nanodomains. *Adv. Mater.* **17**, 1878–1881 (2005).

28. Qiang, Z., Zhang, Y., Groff, J. A., Cavicchi, K. A. & Vogt, B. D. A generalized

method for alignment of block copolymer films: solvent vapor annealing with soft shear. *Soft Matter* **10**, 6068–6076 (2014).

29. Fraser, B., Denniston, C. & Müser, M. H. Diffusion, elasticity, and shear flow in self-assembled block copolymers: A molecular dynamics study. *J. Polym. Sci. Part B Polym. Phys.* **43**, 970–982 (2005).

30. Fraser, B., Denniston, C. & Müser, M. H. On the orientation of lamellar block copolymer phases under shear. *J. Chem. Phys.* **124**, 124–129 (2006).

31. Kim, Y. H. *et al.* Phase structure development in poly (styrene-co-acrylonitrile)/ poly (methyl methacrylate) blend under elongational flow. *Polymer.* **41**, 4747–4749 (2000).

32. Kwon, Y. K., Ko, Y. S. & Okamoto, M. Elongation flow-induced morphological change of a diblock copolymer melt of polystyrene and poly(ethylene propylene). *Polymer.* **49**, 2334–2341 (2008).

33. Albalak, R. J. & Thomas, E. L. Microphase separation of block copolymer solutions in a flow field. *J. Polym. Sci. Part B Polym. Phys.* **31**, 37–46 (1993).

34. Amurin, L. G., Carastan, D. J. & Demarquette, N. R. Morphological evolution of block copolymer nanocomposites submitted to extensional flows. *J. Rheol. (N. Y. N. Y).* **60**, 175–189 (2016).

35. Wong, A. & Park, C. B. The effects of extensional stresses on the foamability of polystyrene–talc composites blown with carbon dioxide. *Chem. Eng. Sci.* **75**, 49–62 (2012).

36. Tran, C. & Kalra, V. Molecular dynamics study on effect of elongational flow on morphology of immiscible mixtures. *J. Chem. Phys.* **140**, 134902 (2014).

37. Kalra, V. & Joo, Y. L. Coarse-grained molecular dynamics study of block copolymer/nanoparticle composites under elongational flow. *J. Chem. Phys.* **131**, 214904 (2009).

38. Bruns, W. & Bansal, R. Molecular dynamics study of a single polymer chain in solution. *J. Chem. Phys.* **74**, 2064–2072 (1979).

39. Weeks, J., Chandler, D. & Andersen, H. C. Role of Repulsive Force in Determining the Equilibrium Structure of Simple Liquids. *J. Chem. Phys.* **54**, 5237 (1971).

40. Chremos, A., Nikoubashman, A. & Panagiotopoulos, A. Z. Flory-Huggins parameter χ, from binary mixtures of Lennard-Jones particles to block copolymer melts. *J. Chem. Phys.* **140**, 054909 (2014).

41. Daivis, P. J. & Todd, B. D. A new algorithm for unrestricted duration nonequilibrium MD simulation of planar elongational flow. *Comput. Phys. Commun.* **117**, 191–199 (1999).

42. Kraynik, A. M. & Reinelt, D. A. Extensional Motions of Spatially Periodic Lattices. *Int. J. Multiph. Flow* **18**, 1045–1059 (1992).

43. Daivis, P. J. & Todd, B. D. A simple, direct derivation and proof of the validity of the SLLOD equations of motion for generalized homogeneous flows. *J. Chem. Phys.* **124**, (2006).

44. Todd, B. D. & Daivis, P. J. The stability of nonequilibrium molecular dunamics simulations of elongational flows. *J. Chem. Phys.* **112**, 40 (2000).

45. Matin, M. L., Daivis, P. J. & Todd, B. D. Comparison of planar shear flow and planar elongational flow for systems of small molecules. *J. Chem. Phys.* **113**, 9122 (2000).

46. Humphrey, W., Dalke, A. & Schulten, K. VMD: Visual Molecular Dynamics. *J. Mol. Graph.* **14**, 33–38 (1996).

47. Schultz, A. J., Hall, C. K., Genzer, J. & Carolina, N. Computer Simulation of Block Copolymer / Nanoparticle Composites. *Macromolecules* **38**, 3007–3016 (2005).

48. Zhmayev, Y. *et al.* Controlling the Placement of Spherical Nanoparticles in Electrically Driven Polymer Jets and its Application to Li-Ion Battery Anodes. *Small* 5543–5553 (2016). doi:10.1002/smll.201601878

CHAPTER 3

SIMULTANEOUS UNIAXIAL EXTENSIONAL DEFORMATION AND CYLINDRICAL CONFINEMENT OF BLOCK COPOLYMERS USING NON-EQUILIBRIUM MOLECULAR DYNAMICS

Using coarse-grained nonequilibrium molecular dynamics, symmetric block copolymers are simulated under the combined effects of cylindrical confinement and uniaxial extensional deformation. For a given confinement diameter, a block copolymer (BCP) will self-assemble into a fixed number of concentric cylinder lamellae at equilibrium. The changing diameter during uniaxial extensional deformation therefore is expected to affect the morphology of the BCPs. The aim of this study is to investigate the interplay of deformation and confinement on BCP morphology by varying the simulation strain rate and diameter. Two different simulation approaches are conducted: constant time simulations with varying initial diameter and constant strain simulations with varying simulation time. A comparison of self-assembly at different strain rates shows that for low strain rates, near-equilibrium morphology can form despite the deformation, while for progressively higher strain rates, extra lamellae and disordered morphologies appear. By defining a Weissenberg number based on the deformation and polymer self-assembly time-scales, the morphologies at different strain rates and diameters are explained. Using the time scale analysis, ordered morphologies appear for $Wi < 1$, while extra lamellae and disordered morphologies occur at $Wi > 1$. For the latter case, the cylinder diameter shrinks too quickly for polymers to form the equilibrium morphology, which results in a mixture of lamellar structures along the cylinder length.

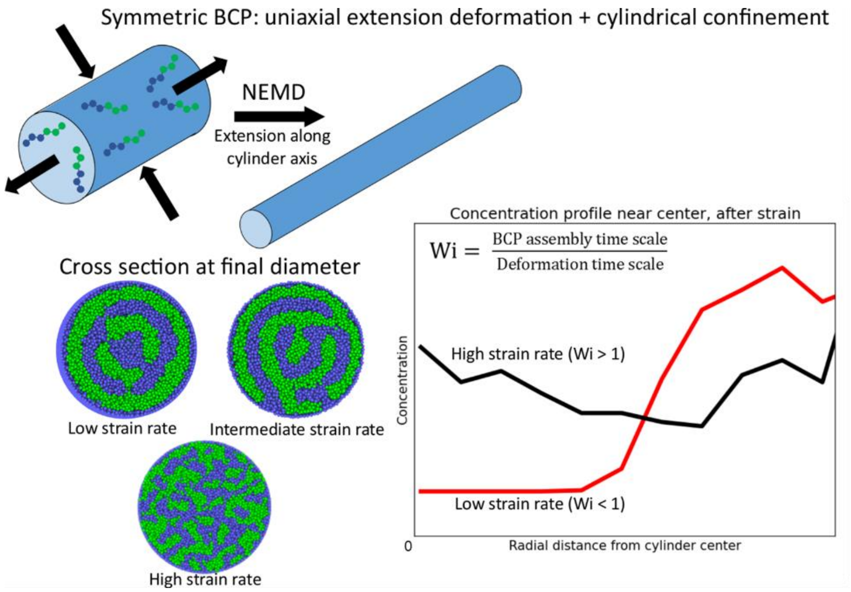

Abstract Figure Summary of extension + confinement simulation method and the Weissenberg time scale analysis results.[1]

3.1 Introduction

Block copolymers (BCPs) have attracted extensive interest over the last few decades due to their ability to self-assemble into ordered mesoscale domains.[2] These ordered structures have current and potential applications in the energy storage, semiconductor, and medical industries.[3,4] The mesoscale domains can be used as a template to place nanoparticles selectively, or one polymer species can be removed to leave behind a porous or patterned material.[5–7] This enables the fabrication of materials with controllable features at nanometer length scales.[8]

The self-assembly process in a diblock copolymer is driven by a difference in chemical interaction between the two polymer blocks, A and B, which are covalently bonded together into a chain. Typically, it will be more enthalpically favorable for a polymer to place near its own species, leading to the formation of phase separated domains. This is limited by the covalent bond linking the dissimilar polymers together physically as well as entropic contributions related to the chain stretching. These forces cause BCPs to self-assemble into a variety of interesting morphologies. At highly asymmetric volume ratios, BCPs assemble into spheres to minimize the unfavorable surface contacts between unlike domains. At symmetric volume ratios (1:1), BCPs form lamellar structures.[9] The morphology is also greatly influenced by physical confinement. When symmetric BCPS are trapped between parallel plates, the number of lamellae will depend on the length of the gap between the plates and the length of the polymer chains. More complex confinements have also been studied, such as cylindrical confinement. Molecular dynamics simulations[10–12] and experiments[13–17] of cylindrically confined BCPs have shown good agreement in predicting new self-assembled morphologies such as concentric lamellae, helical, and stacked disc.

Cylindrical confinement is of particular interest because it occurs during polymer nanofiber processing methods like electrospinning. Electrospinning allows BCPs and other polymers to be processed into nanofibers with high surface area to volume ratios and is considered to be an effective process due to its ease of use, speed, and scalability.[18,19] During the electrospinning process, polymer solution is drawn from a needle and undergoes very high uniaxial extensional deformation due to an external electrical field, which can affect the polymer chain entanglement.[20] The large surface area created causes the solvent to evaporate quickly, leaving behind polymer fibers with diameters between 100nm and 1 micron. When BCPs are used in the electrospinning process they self-assemble while sufficient solvent is present, but their rearrangement freezes once the solvent is removed, resulting in kinetically trapped morphologies. In electrospinning of BCPs, it has proven difficult to achieve complete ordered self-assembly during the process itself, which we hope to explain by investigating through simulation.[14]

Extensional deformation without confinement has also been investigated for BCPs in both experiment and simulation. Kim et. al. experimentally studied poly(styrene-co-acrylonitrile) mixed with poly methyl methacrylate but could not reach steady state.[21] Polystyrene-poly(ethylene propylene) diblock copolymer under small elongational strain showed lamellae that align perpendicular to the flow direction, showing that the deformation affects the orientation of the self-assembled domains.[22] Planar elongational flow simulations have observed order-disorder transitions caused by the strain rate.[23] Shear flow has been more frequently investigated and has been shown to orient domains towards the shear direction and affect the distribution of nanoparticles.[24,25] Combining deformation and confinement, Guo et al. conducted simulations of cylindrically confined BCPs under oscillatory shear flow and observed that morphology transitions could be induced with increasing oscillatory shear frequency and amplitude. However, the case of uniaxial extensional flow with confinement is necessary to model assembly during the electrospinning

In this study, we develop a method to investigate the case where both uniaxial extensional deformation and cylindrical confinement are affecting BCP self-assembly simultaneously using nonequilibrium molecular dynamics. To the author's best knowledge, this is the first molecular dynamics study to combine extensional deformation and cylindrical confinement in one simulation. The advantages of molecular dynamics over experiment in this case include a complete picture of the mesoscale morphology and easy adjustment of strain rates, confinement diameters, and polymer structure. We intend to use insight from simulation to better understand the interplay of these two external effects in transient time scales and guide electrospinning experiments in controlling BCP domain formation.

3.2 Model and Simulation Details

3.2.1 Model

We used coarse-grained non-equilibrium molecular dynamics to study the transient effect of uniaxial extensional flow on cylindrically confined polymers. In this paper, all properties are listed in their reduced form, which is a non-dimensionalization of the real values using the fundamental constants of bead mass (m), Lennard-Jones energy ε, and Lennard-Jones bond length σ. These constants are set to unity so that the reduced values of temperature T, uniaxial extensional strain rate $\dot{\varepsilon}$, and distance are expressed in terms of combinations of mass, energy, and bond length. Polymers are modelled as bead-spring chains of ten beads. Neighbouring beads in a chain are bonded by a harmonic bond potential:

$$u_{\mathrm{bond}}(r) = \mathrm{K}(r - r_0)^2$$

where r is the distance between two bonded beads. K, the harmonic bond constant, is set as 1000 and r_0, the equilibrium bond length, is set as 1.

The coarse-grained beads interact with one another with pair-wise potentials. Pair-wise potentials are not applied between neighbouring beads in the same chain. To simulate the block copolymer system, a polymer chain contains 5 *A*-type beads connected to 5 *B*-type beads in a linear chain. Due to the difference in potentials between *A*-type beads and *B*-type beads, self-assembly will occur as the polymers segregate into A and B phases. Unfavorable *A*-*B* interactions are modelled by the Weeks-Chandler-Anderson (WCA) potential,[26]

$$u_1(r) = 4\varepsilon\left[\left(\frac{\sigma}{r}\right)^{12} - \left(\frac{\sigma}{r}\right)^{6}\right] + \varepsilon, \qquad r \le 2^{\frac{1}{6}}$$

$$u_1(r) = 0, \quad r > 2^{\frac{1}{6}}$$

where r is the distance between two beads. Favorable *A*-*A* and *B*-*B* interactions are modeled by the full cut and shifted Lennard-Jones potential,

$$u_2(r) = 4\varepsilon\left[\left(\frac{\sigma}{r}\right)^{12} - \left(\frac{\sigma}{r}\right)^{6}\right] + \varepsilon, \qquad r \le 2.5$$

$$u_2(r) = 0, \quad r > 2.5$$

which captures the attraction between polymers of the same type. This Lennard-Jones potential has been used by previous molecular dynamics approaches, and has been found to reproduce the BCP phase diagram well.[27–29] In addition, this coarse-graining model bears similarities to more specific coarse-graining approaches, and could be considered to be a generalization of a PS-PMMA system.[30] The degree of incompatibly between the A and B polymer blocks is typically described by the Flory-Huggins parameter, χ_{ab}, which is dependent upon temperature and the chemical nature of the polymers. In this model the Flory-Huggins parameter was determined to be 53.3, well above the order-disorder value.

Table 3.1 Model for polymer and NP interactions.

Pair interactions	**Potential**
$A : A$, $B : B$ A : Wall	Lennard-Jones, cutoff 2.5, shifted
$A : B$ B : Wall	Weeks-Chandler-Anderson

3.2.2 Confinement and Flow Details

Initially, polymers chains are placed isotropically into a cylindrical region bounded by a cylindrical wall through which beads cannot pass. The wall is selective to the A-type and repulsive to the B-type, which is required to form cylindrical lamellae. We also investigated the nonselective wall case, which can be found in the Supplemental Information. The cylinder axis is aligned along the z direction so that as the simulation progresses, the diameter of the cylinder shrinks and the length increases according to the uniaxial extension strain. Beads are given streaming velocities based on their positions relative to the center of the cylinder, and are integrated using the SLLOD equations of motion.[31] The uniaxial flow is defined by the velocity profile du_i/dx_j:

$$\frac{du_i}{dx_j} = \begin{bmatrix} -\dot{\varepsilon}/2 & 0 & 0 \\ 0 & -\dot{\varepsilon}/2 & 0 \\ 0 & 0 & \dot{\varepsilon} \end{bmatrix}$$

where $\dot{\varepsilon}$ is the extensional strain rate. The temperature was controlled at 1.0 reduced MD units using a Nose-Hoover thermostat, and the site density ρ was fixed at 0.85.[32]

A list of parameters used is given in Table 3.2.

Table 3.2 Simulation and system parameters for the extensional BCP simulation.

Parameter	**Value (MD units)**
Cylinder starting diameter	21-260
Cylinder final diameter	16.4,27.5,39,45
Equilibrium BCP domain length (L_0)	~9.1
Number of beads	60000-1000000
Site density	0.85
Bead diameter	1
Temperature	1
Extensional strain rate	0.001 – 0.02
Polymer aspect ratio	10
A-type bead: B-type bead in BCP chain	1:1
Flory-Huggins parameter	53.3
Timestep	0.005

These simulations are limited in duration by the contraction of the cylinder diameter. If the cylinder diameter approaches the bead diameter, then the simulation will be unable to continue. However, this time limitation still allows the observation of transient behaviour and is appropriate to describe a process like electrospinning which occurs on very fast timescales. Simulation methods for infinite-time simulations of planar elongation flow[33] and uniaxial extensional flow[34] have been developed, but it is not possible to combine these methods with cylindrical confinement.

The diameter and length of the confinement cylinder change in time with the following equations:

$$\mathrm{D}(t) = \mathrm{D}(t=0)\exp(-\dot{\varepsilon}t/2)$$

$$\mathrm{L}(t) = \mathrm{L}(t=0)\exp(\dot{\varepsilon}t)$$

where D$(t = 0)$ and L$(t = 0)$ are the initial cylinder diameter and length, respectively. Periodic boundary conditions are present across the z-axis boundary, but are not present in the x and y directions as beads are blocked by the cylindrical wall. The simulations were run between $3x10^4$ and $6x10^5$ timesteps with a timestep of 0.005 using LAMMPS.[35]

We conducted two different types of simulations: (1) constant strain and (2) constant strain. For constant time simulations, varying the strain rate with constant final diameter required varying the starting diameter. The time was set to 100000 timesteps for these simulations, which was sufficient to observe BCP domain formation in the equilibrium simulation. For the constant strain simulations, varying the strain rates causes the simulation time to vary while the starting and ending diameters are fixed. The strain was set to 4.5 with respect to cylinder diameter which corresponded to a strain of 20 with respect to cylinder length. Therefore, constant strain simulations with higher strain rates had a shorter simulation time. The shortest timescale $3x10^4$ was still sufficient to show ordered self-assembly for the no-flow case at constant diameter of 20.

3.3 Results and Discussion

We look at the case of symmetric block copolymers, which are expected to form concentric cylindrical lamellae at equilibrium with the number of lamellae determined by the polymer properties and confinement diameter.[12] Visualizations of these equilibrium morphologies are shown in Figure 3.1 for different confinement diameters. In a uniaxially deforming cylinder, the confinement diameter shrinks over time, so the number of expected lamellae will change during the simulation. Figure 3.2 shows the deformation of the simulation cylinder over the course of the simulation.

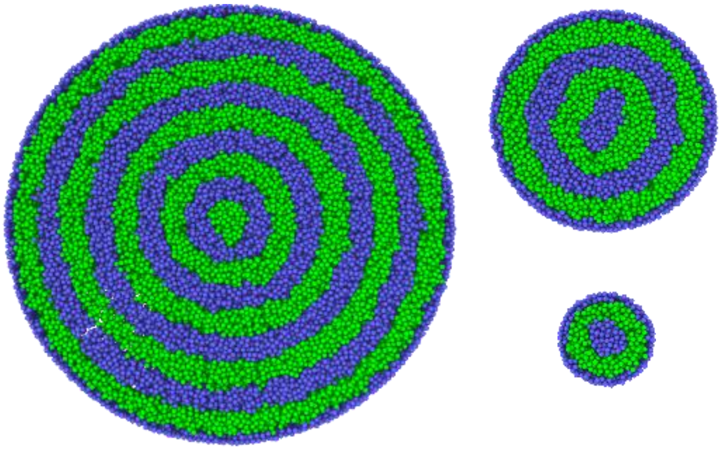

Figure 3.1 Radial cross sections of equilibrium cylindrically confined BCP morphology for varying confinement diameters. Left: $D/L_0 = 10$, Top right: $D/ L_0 = 5$, Bottom right: $D/ L_0 = 2.2$. The cylinder axis is oriented into the page. Polymer type A = blue, polymer type B = green.

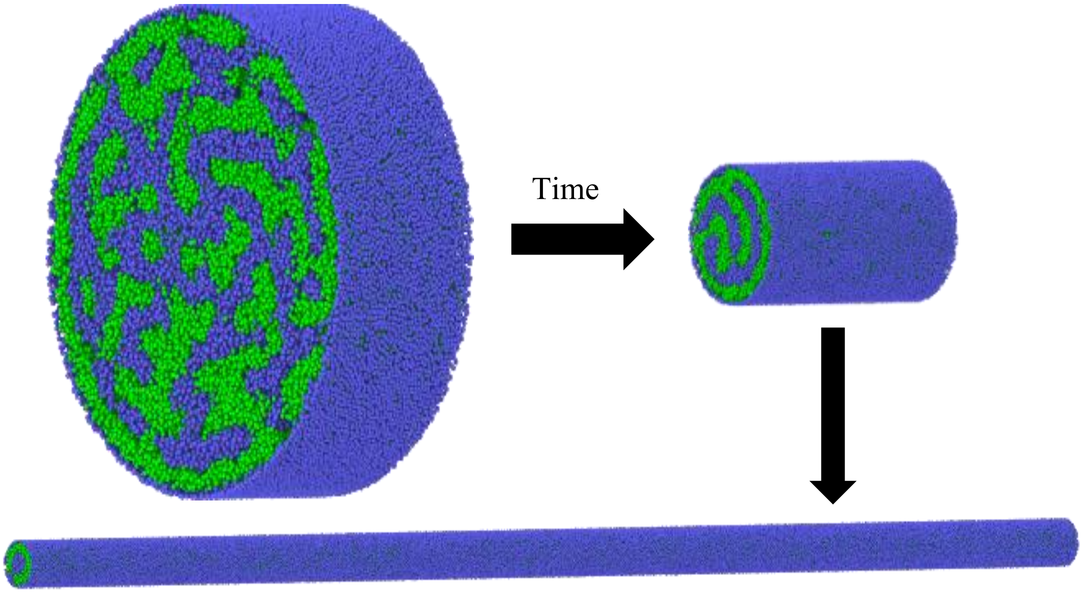

Figure 3.2 Visualizations of transient cylindrically confined BCP morphology over the duration of a simulation. Left: D/L_0 = 10 strain = 1, (early time), Right: D/ L_0 = 5, (middle time), Bottom right: D/ L_0 = 2.2 (late time). Images are not to scale.

In order to understand the effect of the changing diameter on the ordered assembly, it is necessary to identify the number of lamellae expected at equilibrium for a given diameter cylinder. This was accomplished by performing equilibrium (no strain) simulations for incremental diameters, shown in Figure 3.3, and recording the number of concentric cylinder lamellae formed. As expected, as the diameter of the cylinder decreases the number of concentric lamellae decreases. This means that during a nonequilibrium simulation the number of lamellae that are expected at equilibrium will decrease with the diameter according to Figure 3.3. For a simulation with deformation, if the number of lamellae observed after strain is the same as shown in Figure 3.3, then the system is close to or at an equilibrium morphology.

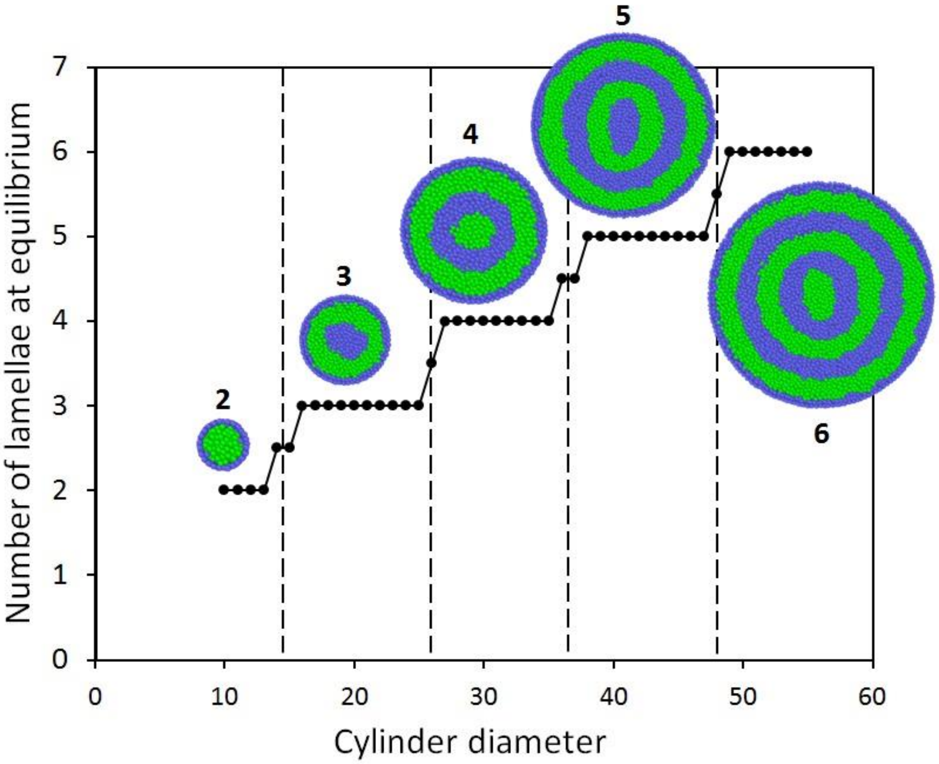

Figure 3.3 Equilibrium number of concentric cylinders for constant diameter simulations. Visualizations of the equilibrium morphology are placed near to the corresponding part of the plot. A value of 2.5 indicates both regions of 2 lamellae and regions of 3 lamellae were observed along the cylinder.

3.3.1 Uniaxial extensional deformation: constant time simulations

In the constant time simulations, the final diameter and simulation time are kept constant while the strain rate and initial diameter vary. The final diameters of 16.4 and 27.9 were chosen for the constant time simulations. These diameters share the characteristic of being immediately before the transition in lamellae number shown in Figure 3.3. This was chosen to ensure that the system was allowed to spend time in the region where 3 lamellae are expected (for 16.4) or 4 lamellae are expected (for 27.9). If instead an ending diameter of 25 was chosen, for example, the system would have very little time in the 3 lamellae region before completing. It was found that the time spent at diameters corresponding to the final number of lamellae strongly influences the final morphology observed.

The equilibrium morphology was observed to be concentric cylinders for all the diameters investigated. Therefore, we used a radial concentration profile as a measure of the order and degree of self-assembly in the system. If the system is at the equilibrium morphology, there should be strong peaks in concentration moving radially along the cylinder. The concentration profiles at ending diameter 16.4 for varying extension rates are shown in Figure 3.4, as well as the corresponding snapshots. For the low strain rates, the profile observed corresponds to the 3 lamellae structure, where polymer B (green) does not place in the center of the cylinder (r=0). This shows that it is still possible to produce equilibrium morphology despite deformation. As the strain rate increases, the distribution changes primarily near r=0. For strain rates starting at 0.007 and above, polymer B begins to have higher concentrations at r=0 and shows a profile with two peaks. This corresponds to, on average, a 4 lamellae morphology shown in Figure 3.3. In addition, the domains are less well formed in general at higher strain rates, with lower peaks and higher troughs, which can also be seen from the snapshots. So, for low strain rates the strain does not affect the final morphology while at high strain rates regions of extra lamellae or disordered morphology emerge.

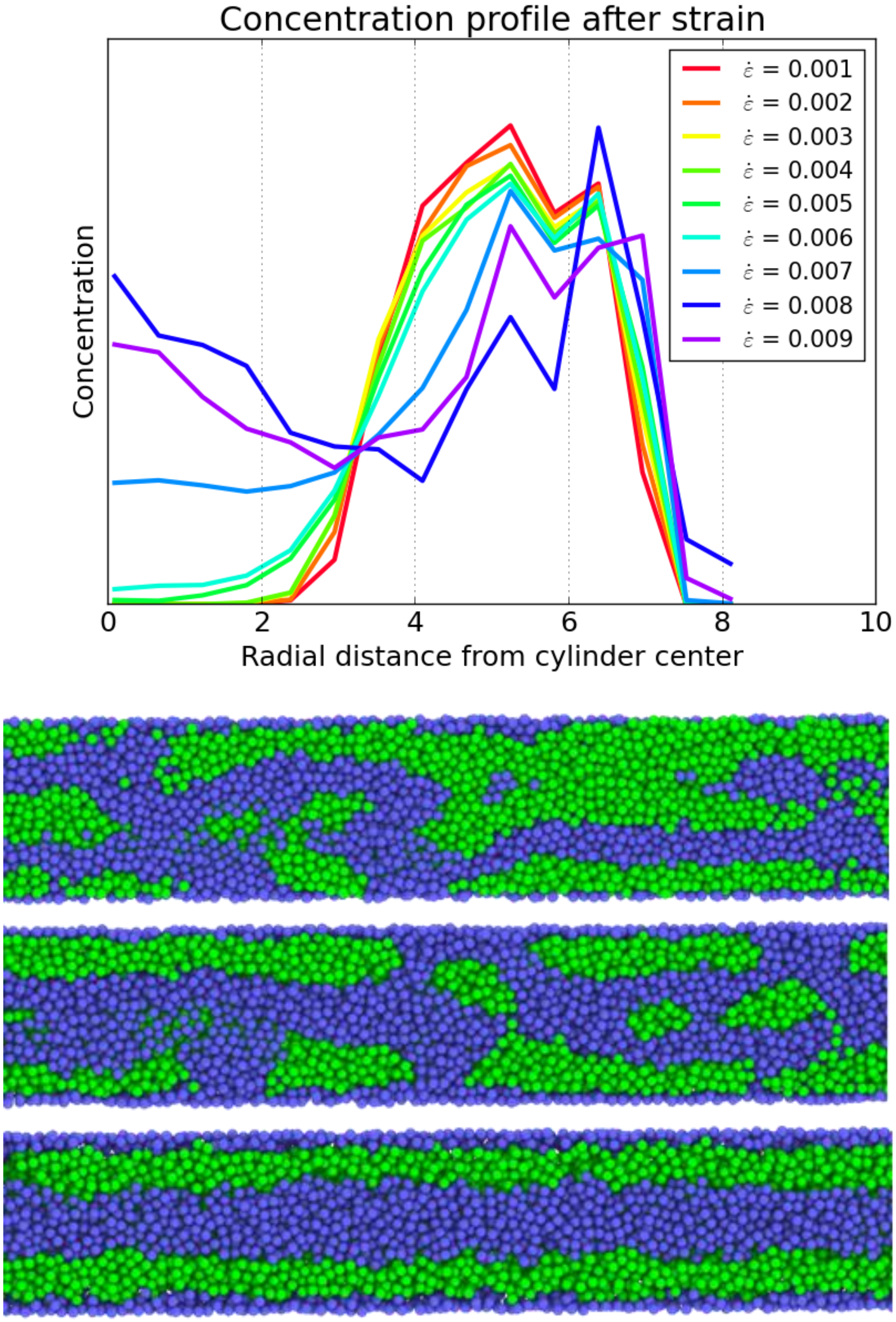

Figure 3.4 Radial concentration profile of polymer B (green) after strain for constant time simulations and corresponding axial cross section images. For images, $\dot{\varepsilon}$ = 0.009

(top), $\dot{\varepsilon}$ = 0.005 (middle), and $\dot{\varepsilon}$ = 0.001 (bottom). $\dot{\varepsilon}$ = uniaxial extensional strain rate and final diameter = 16.4.

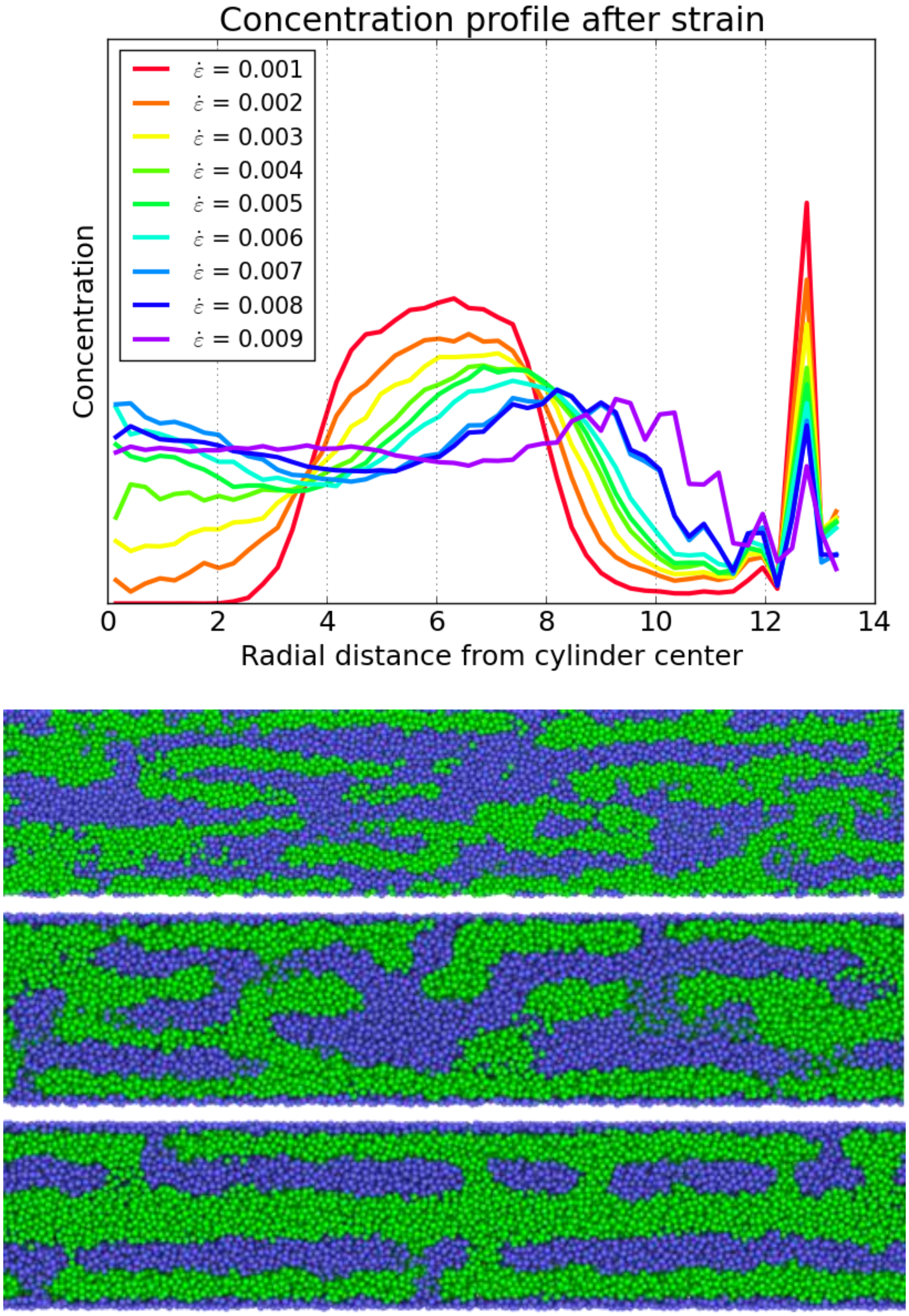

Figure 3.5 Radial concentration profile of polymer A (blue) after strain for constant time simulations and corresponding axial cross section images. For images, $\dot{\varepsilon}$ = 0.009 (top), $\dot{\varepsilon}$ = 0.005 (middle), and $\dot{\varepsilon}$ = 0.001 (bottom). $\dot{\varepsilon}$ = uniaxial extensional strain rate

and final diameter = 27.5.

This behavior is confirmed by examining results from a second final diameter, 27.5. For this case, the expected equilibrium final morphology is 4 lamella instead of the 3 lamellae observed for the 16.4 case. Again, at the low strain rate of $\dot{\varepsilon}$ = 0.001 the equilibrium 4 lamellae structure is still formed from the nonequilibrium simulation, although microbridging defects are present. However, nonequilibrium structures begin to appear at much lower strain rates than the 16.4 case. For $\dot{\varepsilon}$ = 0.006, an extra peak at radius 0 corresponding to the 5 lamella morphology can be seen in plot of Figure 3.5, despite the final diameter having an equilibrium morphology of 4 lamellae. This extra lamella peak is a transient phenomenon resulting from structures formed earlier at higher diameters not having time to be fully erased or combined as the diameter shrinks. As the diameter crosses the threshold between the 5 lamella equilibrium morphology region and 4 lamella equilibrium morphology region, it is no longer thermodynamically favorable for the extra domain to exist. However, if the polymer re-assembly time-scale is comparatively slower than the extensional deformation time scale, then the extra lamella can be observed.

At even higher strain rates, such as $\dot{\varepsilon}$ = 0.009, the diameter is changing fast enough that lamellae do not have adequate time to form well. This results in no peaks appearing in the concentration distribution. Even though the $\dot{\varepsilon}$ = 0.001 and the $\dot{\varepsilon}$ = 0.009 cases have the same time for self-assembly to occur, the high strain rate $\dot{\varepsilon}$ = 0.009 has greatly inhibited ordered assembly, showing that strain rate can be used to control BCP morphology.

The effect of strain rate be explained the considering the different competing time scales present during deformation. First, there is a self-assembly process underway which requires time for polymer chains to diffuse and reorient to form domains. The time scale for self-assembly is related to polymer properties such as length, strength of interaction, and wall selectivity. Second, there is the deformation time scale which is defined by the strain rate and controls how fast the system moves through different diameter regimes and aligns the polymer chains towards the flow direction.

To quantify the relationship between self-assembly, confinement, and strain rate, a Weissenberg number, representing the ratio of convection to diffusion, is defined as:

$$Wi = \frac{t_{SA}}{t_m}$$

where t_{SA} is a self-assembly time and t_m is a morphology time. t_{SA} was defined as the simulation time required for the concentric lamella to self-assemble during an equilibrium simulation at the final diameter. t_{SA} was calculated as the time required for the system energy to reach 99% of the final value, and the results are shown in Table 3.3. At larger diameter, t_{SA} is larger, which is explained by the method in which the self-assembly occurs. The self-assembly is driven by the wall selectivity, as shown in Figure 3.6. The domains first form furthest from the center at the wall, and the inner domains form after. Therefore, at a larger diameter, the wall is more domains away from the center, increasing the time for the effect of the wall templating to reach the center. This explains why the greatest differences in morphology appear at r=0, which is furthest from the cylinder wall.

Table 3.3 Value of t_{SA}, the self-assembly time of the cylindrically confined system at equilibrium for the given diameter.

Diameter	t_{SA}
16.7	110
27.5	228
39.0	485

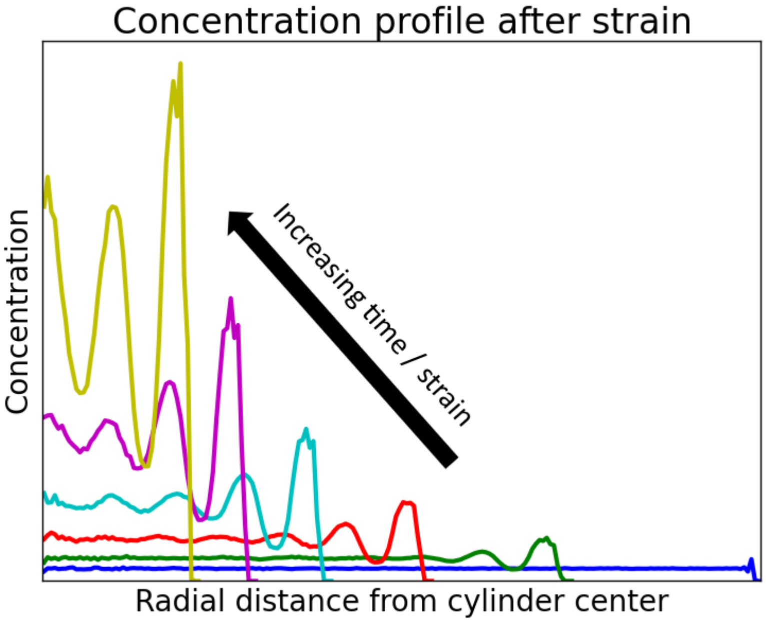

Figure 3.6 Example time series of radial concentration profiles during strain. Successive curves from right to left are the profiles of the same simulation at later simulation times.

Strain rate	**Start Diameter**	**End Diameter**	t_m	**Wi**
0.001	21.1	16.4	500	0.22
0.002	27.1	16.4	460	0.24
0.003	34.8	16.4	300	0.37
0.004	44.7	16.4	230	0.48
0.005	57.3	16.4	185	0.59
0.006	73.7	16.4	153	0.72
0.007	94.5	16.4	131	**0.84**
0.008	121.5	16.4	114	**0.96**
0.009	156	16.4	102	**1.07**
0.001	35.3	27.5	500	0.46
0.002	45.3	27.5	270	**0.83**
0.003	58.2	27.5	180	**1.27**
0.004	74.75	27.5	135	**1.69**
0.005	95.98	27.5	108	**2.11**
0.006	123.2	27.5	90	**2.53**
0.007	158.3	27.5	77	**2.96**
0.008	203.2	27.5	67	**3.40**
0.009	260.9	27.5	60	**3.80**

Table 3.4 Time scale analysis for BCP self-assembly and deformation in the constant time simulations. Bolded Wi numbers correspond to strain rates where extra peaks or no peaks are observed in the concentration profiles of Figures 3.4 and 3.5.

t_m is defined as the time the cylinder diameter is within the range where the final number of lamellae is expected. For example, for the 16.4 final diameter case, this would be the time that spent between D = 25, the largest diameter where 3 lamellae are expected, and 16.4, the final diameter. So, comparing t_m to t_{SA} is comparing the amount of time required for ordered assembly against the amount of time available for assembly.

Table 3.4 shows the results of the Wi number time scale analysis. It can be seen that for Wi numbers much lower than 1, the equilibrium morphology is obtained for both the 16.4 and 27.5 final diameters. When Wi is close to or greater than 1, it was found that nonequilibrium morphology is present. The bold entries in Table 3.4 indicate simulations for which extra peaks or no peaks are present in Figures 3.4 and 3.5, which correspond to the extra lamellae and disordered morphologies. The consistency over both diameters and the transition occurring near Wi = 1 suggests that the two time scales used in the Wi analysis are the primary competing forces in BCP self-assembly with extensional deformation and cylindrical confinement. It is interesting to note that the disruptive effects at Wi ~ 1 of extensional deformation on the BCP self-assembly stem not from the velocity gradients imposed on the polymers but rather the changing wall diameter. With higher strain rates, the cylindrical wall surface contracts too quickly for the polymer domains to form with the correct number of lamellae, resulting in the transient morphologies presented.

To further apply the time scale approach, the constant time simulations were repeated for the case of final diameter = 39 (5 equilibrium lamellae). The same time scale approach and the results for the three diameters are summarized in Figure 3.7. The dotted line indicates the cutoff Wi number (0.8) above which nonequilibrium, low order morphologies began to appear.

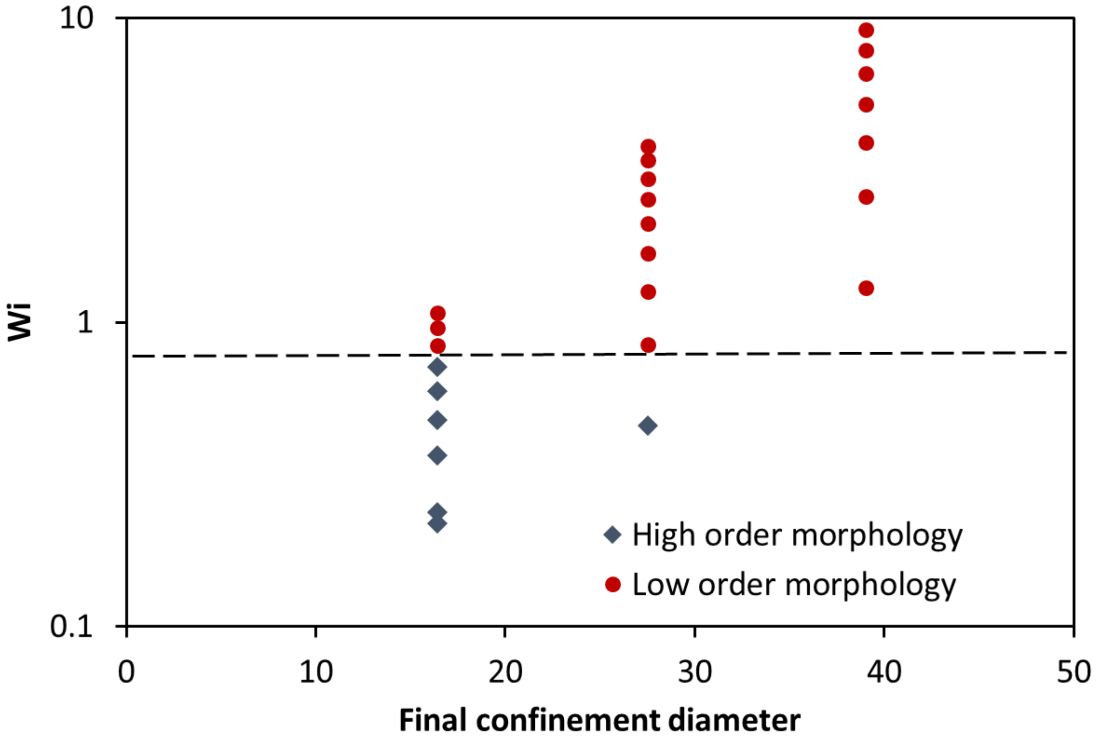

Figure 3.7 Calculated Weissenberg values for constant time extensional deformation simulations. High order morphologies were generally observed for Wi < 1, and low order, transient morphologies were observed for Wi > 1.

3.3.2 Uniaxial extensional deformation: constant strain simulations

To verify that the appearance of extra lamellae morphology is not a byproduct of the varying initial starting diameters necessary for the constant time simulations, constant strain simulations with varying simulation time were conducted. Since the both the starting and ending diameters are constant for varying strain rate, higher strain rates will result in shorter simulation times. Figure 3.8 shows the radial concentration profiles for starting diameter of 200 and final diameter of 45 and the corresponding snapshots. The $\dot{\varepsilon} = 0$ entry represents the equilibrium result at the final diameter. $\dot{\varepsilon} = 0$ shows well defined peaks which match the equilibrium ordered concentric lamellae shown in the Figure 3.1 top right image. In contrast, $\dot{\varepsilon} = 0.02$ is far from the equilibrium morphology, similar to the high strain rate results for the constant time simulations, and has a disordered morphology. This is not due to a lack of domain formation; rather, along the length of the cylinder there are different numbers of poorly formed concentric lamellae, which average out to show no radial dependence. This is shown in the topmost cross sectional images of Figure 3.8, where regions of 3 lamellae and 2 lamellae are both common.

While the equilibrium ($\dot{\varepsilon} = 0$) and $\dot{\varepsilon} = 0.02$ cases show the two extremes in morphology, intermediate strain rates show the formation of extra transient lamellae. This is most prominent for $\dot{\varepsilon} = 0.002$, where a strong 3rd peak is present in the concentration profile. This again indicates that the extra lamella phenomenon can be controlled by the process strain rate.

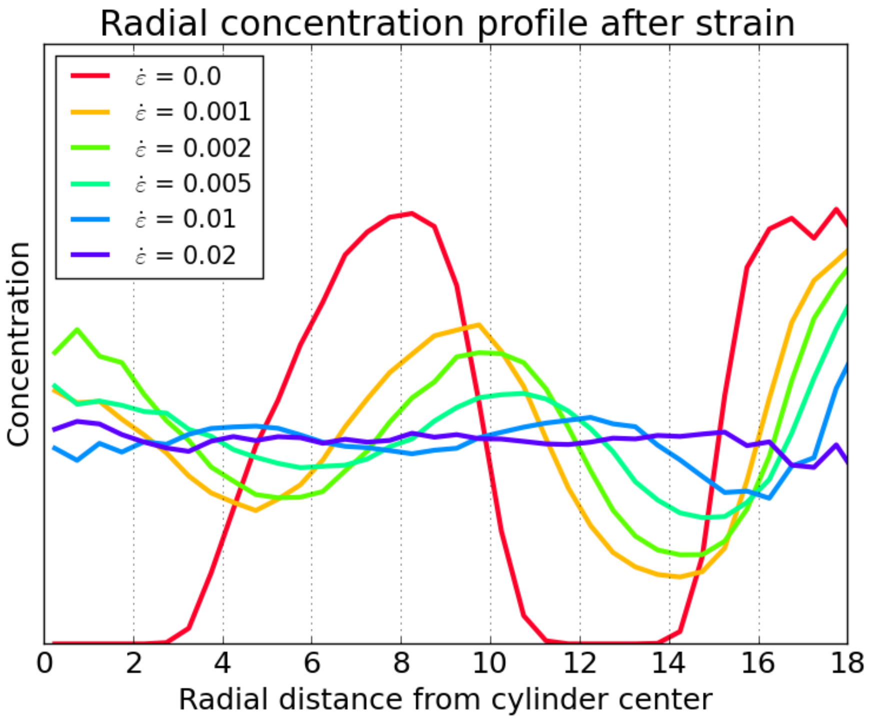

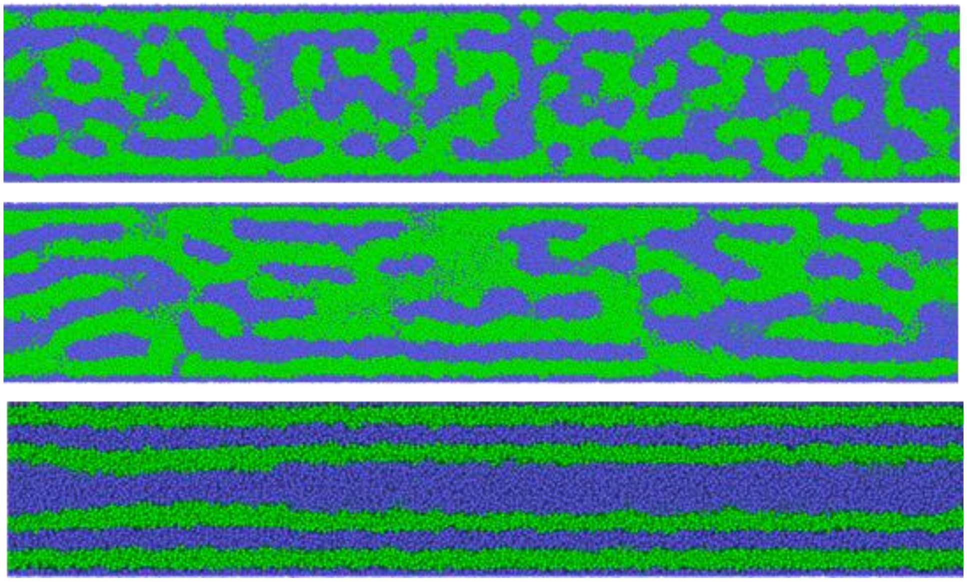

Figure 3.8 Radial concentration profile of polymer B (green) at strain = 4.4 for constant strain simulations and corresponding axial cross section images. For images, $\dot{\varepsilon}$ = 0.02 (top), $\dot{\varepsilon}$ = 0.002 (middle), and $\dot{\varepsilon}$ = 0 (bottom). $\dot{\varepsilon}$ = uniaxial extensional strain rate.

3.4 Conclusions

By combining the effects of uniaxial extensional deformation and cylindrical confinement into a single simulation, the interplay between the two effects and their impact on BCP self-assembly was investigated. For low strain rates, it was still possible to obtain the equilibrium concentric cylinder morphology despite the deformation. However, with increasing strain rate transient morphologies began to appear, including mixtures of the correct number of lamella and an extra lamella within the same cylinder. The appearance of transient, nonequilibrium morphologies was explained by defining a Wi number relating the time scale of self-assembly for the no-deformation case to the time that the cylinder diameter is within a range where the expected number of lamella is constant. These findings suggest that by varying the strain rate of a polymer fiber spinning process such as electrospinning, the self-assembled morphology within the resulting nanofiber can be controlled. Under typical electrospinning conditions the strain rate is high and the polymer assembly kinetics slow, resulting in poor ordered assembly.[16] A typical electrospinning time scale is around 1ms, and an optimistic value for an experimental BCP assembly time is around 1 minute, resulting in a very high Wi number and poor self-assembly.[36,37] However, the molecular dynamics simulations here suggest that if the Wi number could be reduced to near or lower than unity, ordered concentric cylinder assembly could occur during the electrospinning process. This could be accomplished by lowering the strain rate, decreasing the solvent evaporation rate, lowering the polymer chain length, strengthening unfavorable interactions between the two polymer blocks, and decreasing the confinement diameter. For the case of immiscible polymer blends, decreasing the solvent evaporation rate has already been shown to speed up the phase separation during electrospinning.[38] By improving BCP self-assembly during the process, slow and costly thermal annealing post-treatments could be eliminated, increasing the commercial viability of advanced ordered BCP nanofiber materials.

3.5 Supplemental information

3.5.1 Effect of cylindrical wall selectivity on BCP morphology

To illustrate the effect of the wall selectivity on the BCP morphology, we studied the case of a nonselective wall instead of the selective wall used in the main work. All other parameters were kept the same.

Figure 3.9 shows the equilibrium morphology for the nonselective case. The BCP forms a stacked disc structure. However, the simulation time to form this morphology is longer than the time needed to form concentric cylindrical lamellae because there is no longer a template for the ordered assembly in the form of the selective wall. In Figures 3.10 and 3.11, the morphologies for the low strain rate of 0.001 are shown. The morphologies are far from equilibrium, but there are regions which show the beginnings of stacked disc morphology, especially in Figure 3.10. In Figure 3.12, the high strain rates prevents any stacked disc morphology and instead results in long domains stretched in the flow direction, illustrating the competing effect of the extensional deformation.

Like the cylindrical lamellae results, these results suggest that for the stacked disc morphology a similar interplay between assembly time and extension rate can occur. In addition, the results show the importance of the selective wall in promoting the cylindrical lamellar morphology. We plan to study the dynamics of the nonselective case further in the future.

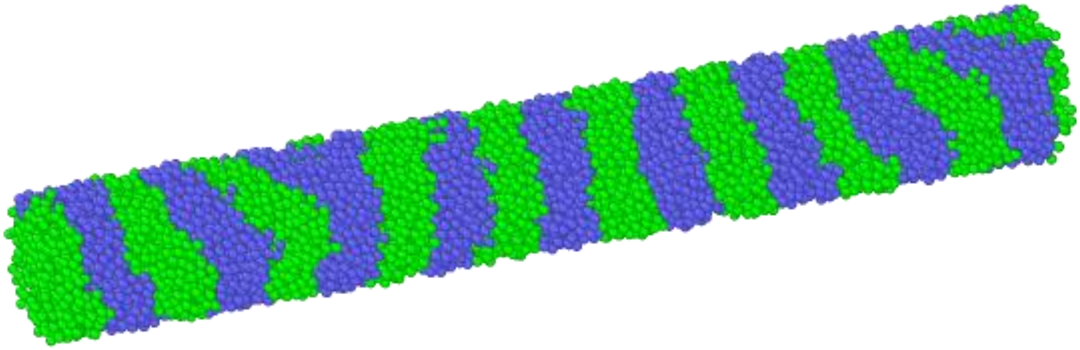

Figure 3.9 Equilibrium morphology for nonselective cylindrical confinement: $\dot{\varepsilon} = 0.0$, final diameter = 16.4, 200000 timesteps.

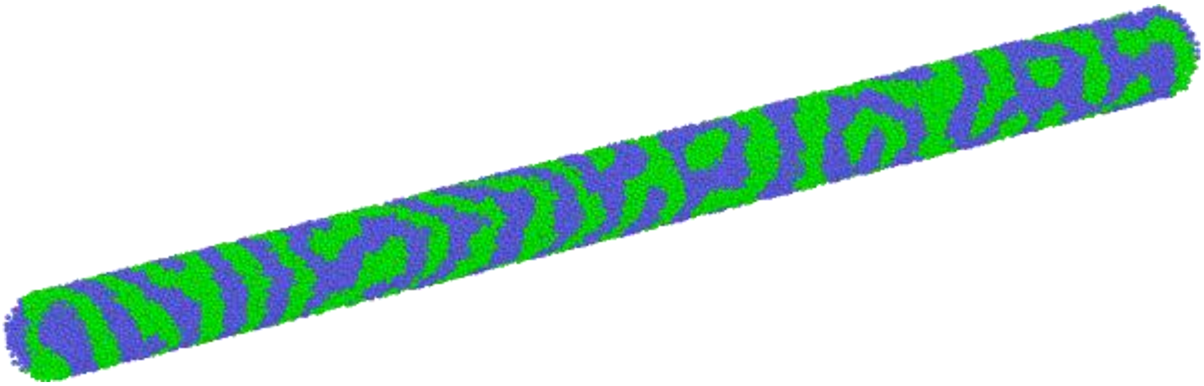

Figure 3.10 Nonequilibrium morphology for nonselective cylindrical confinement: $\dot{\varepsilon} = 0.001$, final diameter = 16.4, 100000 timesteps.

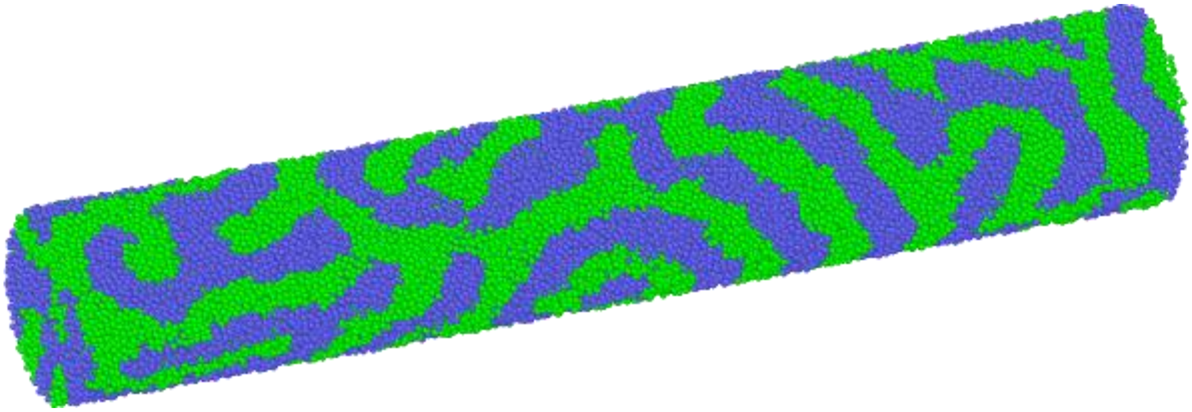

Figure 3.11 Nonequilibrium morphology for nonselective cylindrical confinement: $\dot{\varepsilon} = 0.001$, final diameter = 27.5, 100000 timesteps.

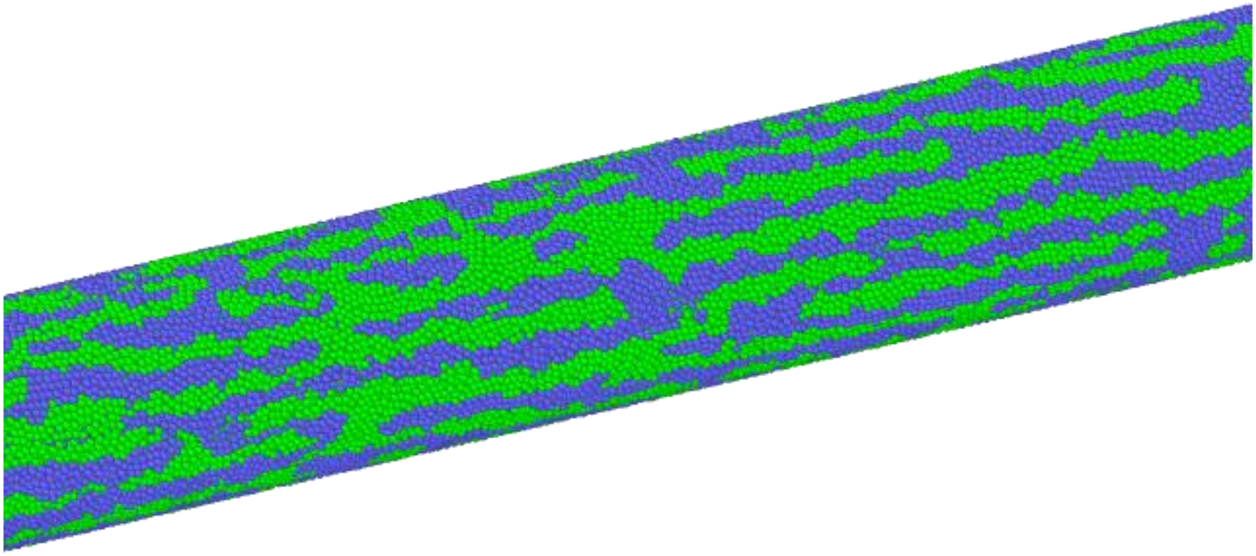

Figure 3.12 Nonequilibrium morphology for nonselective cylindrical confinement: $\dot{\varepsilon} = 0.009$, final diameter = 27.5, 100000 timesteps.

3.5.2 Relaxation of BCP after strain

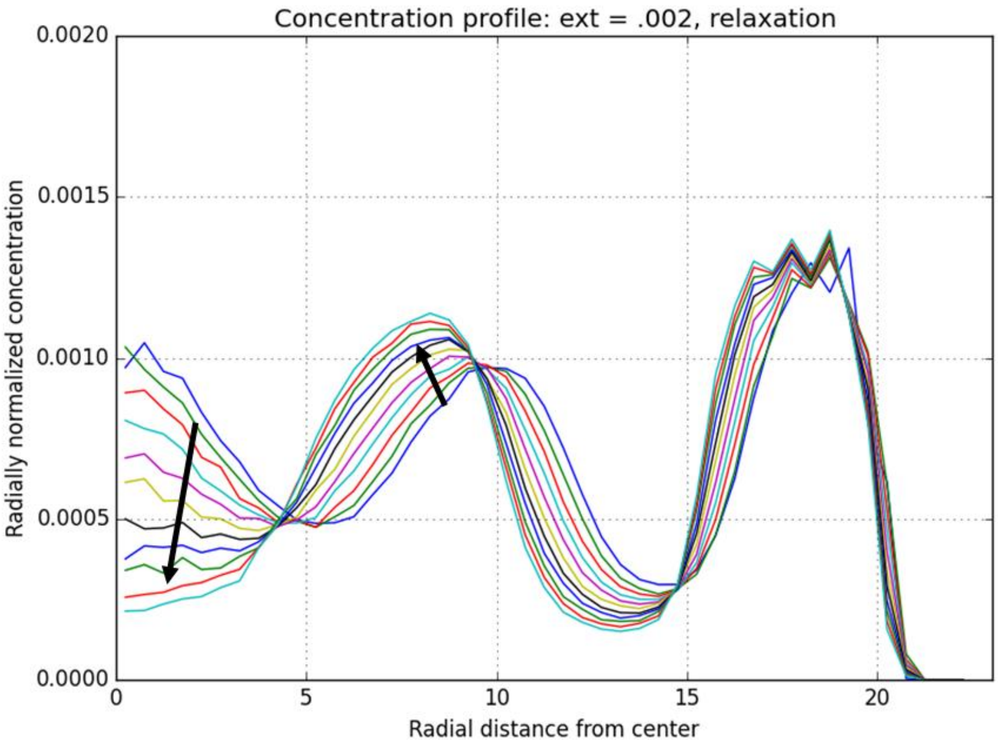

Figure 3.13 Relaxation concentration profile of one of the BCP phases starting at the end of uniaxial extensional deformation which occurred at $\dot{\varepsilon}$ = 0.002. The curve at the start of the arrow represents profile at the end of deformation, and each successive curve is plotted as the simulations continues at $\dot{\varepsilon}$ = 0.

In Figure 3.13, the cylindrically confined BCP is allowed to relax after extensional deformation. Following the arrows, each curve has relaxed a longer amount of time. This results in the initial nonequilibrium morphology of 3 lamellae slowly self-correcting into a 2 lamellae morphology. The result in Figure 3.13 provides clear evidence that the extensional deformation results in transient morphologies which will revert to equilibrium after sufficient time, and also identifies that the driving force of self-assembly towards equilibrium morphology occurs even after the disruptive extensional deformation.

3.5.3 Polymer blend under uniaxial extensional flow and cylindrical confinement

To investigate the behavior of immiscible polymer blends, we repeat the same procedure as for BCP but instead use two polymer chains in equal ratio. The beads within the polymer chains each are equivalent to one of the BCP phases, along the lines of Chapter 2, and each polymer is length 10.

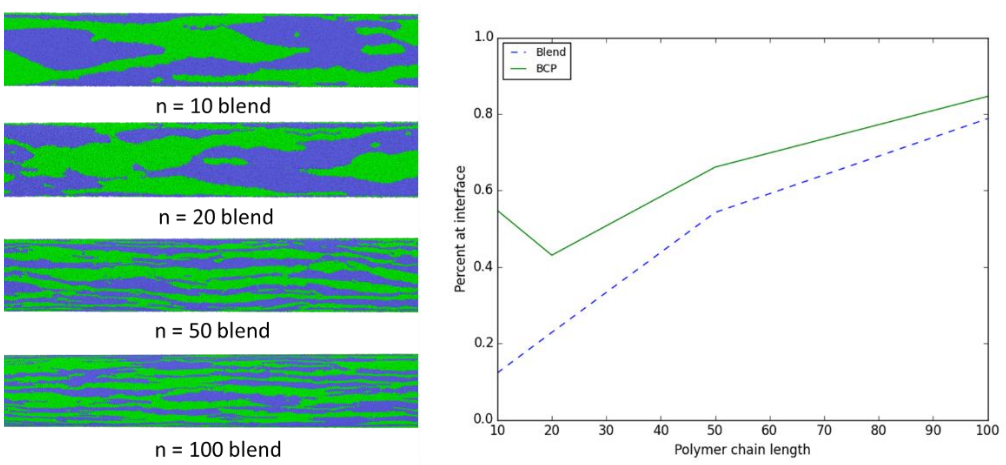

Figure 3.14 Left: Axial morphologies for polymer blend system for different polymer chain lengths n. Right: percent of polymer beads at the interface between domains for blend and BCP systems. $\dot{\varepsilon} = 0.01$, wall is nonselective.

Figure 3.14 shows that the blend systems forms large disordered morphologies at short chain lengths, and forms long thin domains aligned towards the flow direction at high chain lengths. The figure shows that as the polymer length increases, surface area between the domains increases for both blend and BCP due to the smaller domain size. This could be useful for designing sacrificial polymer systems where one polymer type will be removed after electrospinning to leave pores. Based on the simulation, the short chain polymer system would form larger pores and the longer chain would form smaller pores, allowing the tuning of pore size distribution using material properties.

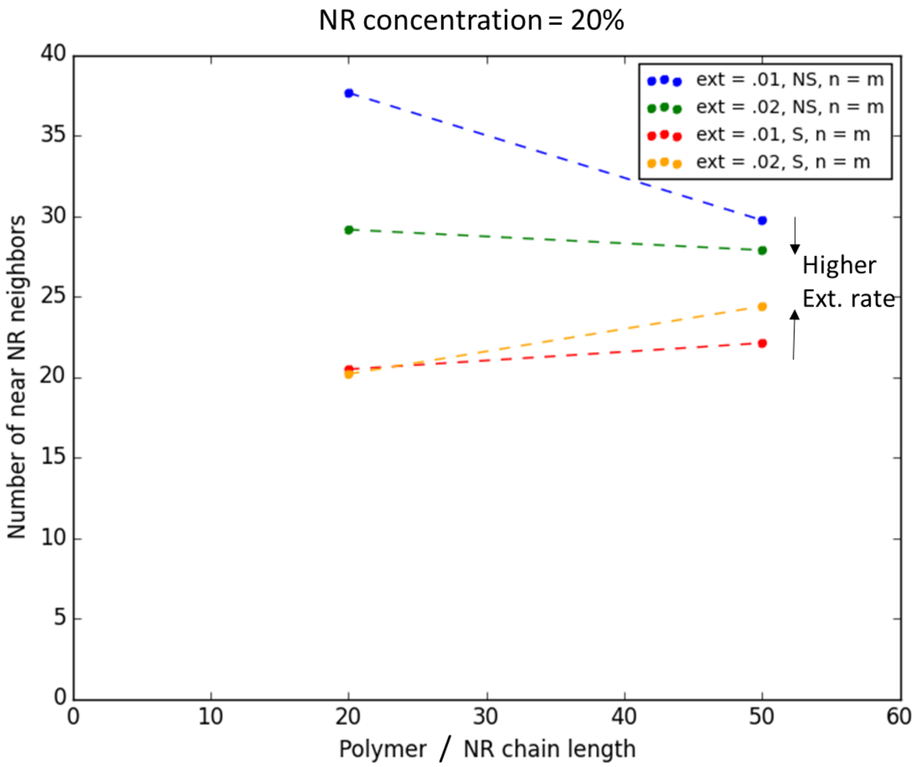

Figure 3.15 Effect of nanorod (NR) aggregation when added to the polymer blend system under cylindrical confinement and uniaxial extension rate $\dot{\varepsilon}$. NS and S stand for nonselective nanorod and selective nanorod, respectively. n = polymer chain length and m = nanorod chain length.

In Figure 3.15, nanorods (NR) were added to the polymer blend system. The NR consist of the same beads as a polymer but are kept rigidly linear. This represents materials like carbon nanotubes and zinc oxide NR. The NR are either selective to one polymer phase or are nonselective towards both, similar to the nanoparticles in Chapter 2. The number of near NR neighbors is a measure of the aggregation of the NR, where a larger value corresponds to higher aggregation. It is preferable for the NR to be dispersed to maximize the nanocomposite material properties, so it important to investigate how electrospinning conditions will influence the dispersion. Figure 3.15 shows that for selective NR, dispersion is worsened at high strain rates. This is because the selective polymer domains become smaller at the higher strain, encouraging NR to form their own domains instead of joining the selective polymer phase. However, for nonselective NR, the opposite occurs. This is because there is an enthalpic benefit for nonselective NR to place at the interface between polymer domains, so by creating additional domain interfaces at higher strain rate more nonselective NR will place at the interface. These trends held true for both the polymer and NR length of 20 and the polymer/NR length of 50. In summary, by minimizing the polymer domain size through increasing the deformation rate and using nonselective nanoadditives, the dispersion of the nanoadditve can be maximized.

3.5.4 Self-assembly time scale of confined block copolymers without deformation

Previous molecular dynamics work has investigated the self-assembly of block copolymers under cylindrical confinement and equilibrium conditions.[10,28,39] These works consider the characteristics of the final assembled morphology without deformation but do not investigate the time scales involved. As seen in section 3.3.1, the time scale of cylindrically confined self-assembly is relevant to the final morphology in the combined uniaxial extension and cylindrical confinement simulations. In this section, this time scale is investigated for multiple confinement diameters and polymer block ratios without any deformation involved.

Block copolymer polymer chain lengths of 10 were used with varying ratios of the two immiscible polymer blocks. The diameter of the cylinder was varied to be an integer ratio of the block copolymer lamellae width L_0. For different block ratios, it is known that block copolymers will form a variety morphologies including cylindrical lamellae, helical, and small spherical domains in increasing block ratio. In the extensional deformation study in section 3.3.1, only 1:1 ratio was considered.

To measure the self-assembly time, the simulation was run from an isotropic starting condition until the intermolecular energy reached within 1% of the final minimum value, at which point the simulation time was recorded. It was found that based on different randomly generated isotropic starting conditions, the self-assembly time could vary significantly. Therefore, 10 randomly generated initial conditions were simulated for each test, and the 10 self-assembly times were averaged together.

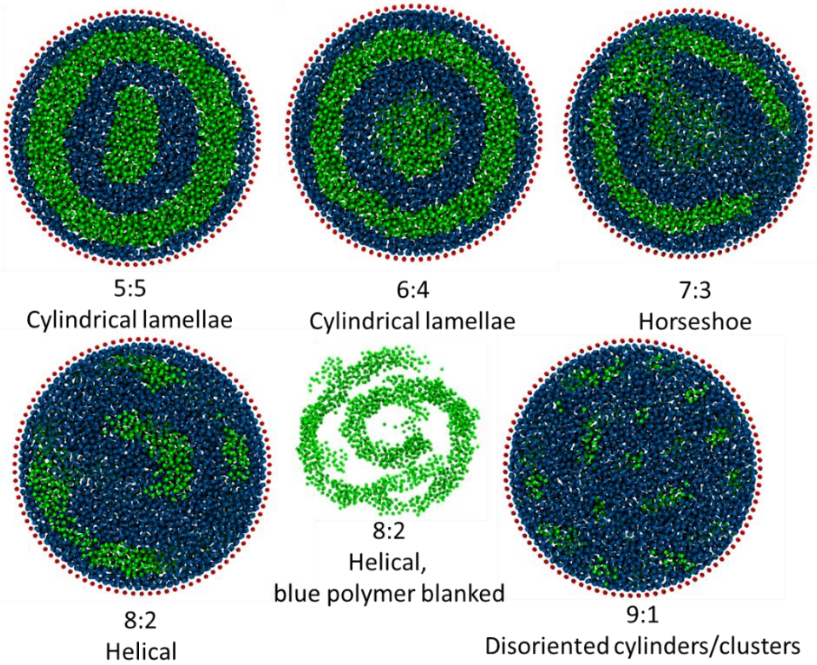

5:5
Cylindrical lamellae

6:4
Cylindrical lamellae

7:3
Horseshoe

8:2
Helical

8:2
Helical,
blue polymer blanked

9:1
Disoriented cylinders/clusters

Figure 3.16 Equilibrium morphology for cylindrical confined BCP with different block ratios.

For reference, Figure 3.16 shows the equilibrium morphologies for the different block ratios simulated. Figure 3.17 shows the self-assembly time results for the varying ratios. For ratios 5:5, 6:4, and 7:3, which form the lamellae and horseshoe structures, the assembly time is smallest for low diameters and increases roughly linearly for increasing diameter. This is due to the additional number of lamellae that must be formed and the long range order that is required. Long range order refers to the fact that the lamella forms a ring in which polymers on one side of the cylinder are interacting indirectly with polymers on the other side in order to form the ordered structure. Essentially, these morphologies only have a single morphological conformation that will satisfy the equilibrium condition. For the skewed block ratios of 8:2 and 9:1, scaling with diameter is not observed. This is because these morphologies have little long range order, resulting in assembly only needing to occur in the local area. Without the requirement of long range order, the self-assembly time does not scale with system size.

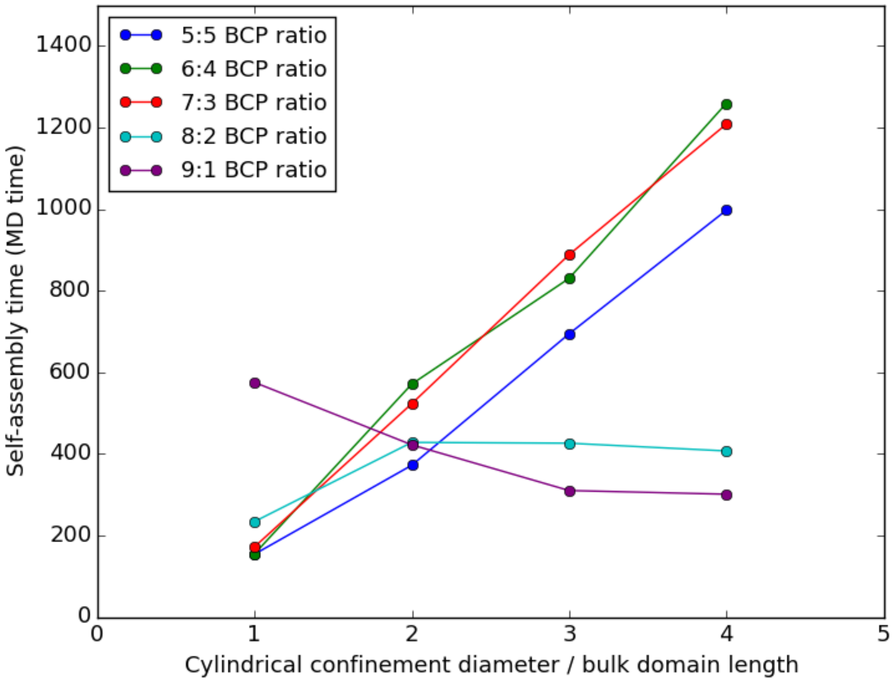

Figure 3.17 Self-assembly time of varying types of BCP in cylindrical confinement plotted against the confinement diameter. Simulations were repeated 10 times and their self-assembly times were averaged to obtain the final values plotted.

These results can also be interpreted by considering the amount of molecular movement required to shift from the initial random condition to the final state. For the concentric cylindrical lamellae for the 5:5 ratio, an entire half of the polymer beads are in the wrong location at the beginning of the simulation. For the 9:1 ratio, at most 20% of the beads are in incorrect location. Therefore, for the larger diameters, the 5:5 ratio has much longer self-assembly time than the 9:1 ratio due to the larger degree of reorganization necessary. For the smallest diameter, this behaviour does not hold true due to the selective cylindrical wall surrounding the simulation. Since the smallest diameter has only two domains, 1 of each block, it is directly and rapidly formed by the direct contact of the domain with the cylindrical wall. This template effect diminishes as diameter grows, as additional domains far from the wall must form without a strong driving force.

3.6 References

1. Shebert, G. L. & Joo, Y. L. Simultaneous uniaxial extensional deformation and cylindrical confinement of block copolymers using non-equilibrium molecular dynamics. *Soft Matter* **14**, 1389–1396 (2018).
2. Darling, S. B. Directing the self-assembly of block copolymers. *Prog. Polym. Sci.* **32**, 1152–1204 (2007).
3. Dong, Y. *et al.* Synthesis of mesoporous carbon fibers with a high adsorption capacity for bulky dye molecules. *J. Mater. Chem. A* **1**, 7391–7398 (2013).
4. Shenhar, R., Norsten, T. B. & Rotello, V. M. Polymer-Mediated Nanoparticle Assembly: Structural Control and Applications. *Adv. Mater.* **17**, 657–669 (2005).
5. Park, C., Yoon, J. & Thomas, E. L. Enabling nanotechnology with self assembled block copolymer patterns. *Polymer.* **44**, 6725–6760 (2003).
6. Kim, J. K., Yang, S. Y., Lee, Y. & Kim, Y. Functional nanomaterials based on block copolymer self-assembly. *Prog. Polym. Sci.* **35**, 1325–1349 (2010).
7. Pryamitsyn, V. & Ganesan, V. Strong segregation theory of block copolymer-nanoparticle composites. *Macromolecules* **39**, 8499–8510 (2006).
8. Jeong, S.-J., Kim, J. Y., Kim, B. H., Moon, H.-S. & Kim, S. O. Directed self-assembly of block copolymers for next generation nanolithography. *Mater. Today* **16**, 468–476 (2013).

9. Schultz, A. J., Hall, C. K., Genzer, J. & Carolina, N. Computer Simulation of Block Copolymer / Nanoparticle Composites. *Macromolecules* **38**, 3007–3016 (2005).

10. Park, J. H., Kalra, V. & Joo, Y. L. Cylindrically confined assembly of asymmetrical block copolymers with and without nanoparticles. *Soft Matter* **8**, 1845 (2012).

11. He, X., Song, M., Liang, H. & Pan, C. Self-assembly of the symmetric diblock copolymer in a confined state: Monte Carlo simulation. *J. Chem. Phys.* **114**, 10510 (2001).

12. Park, J. H. & Joo, Y. L. Formation of interconnected morphologies via nanorod inclusion in the confined assembly of symmetric block copolymers. *Phys. Chem. Chem. Phys.* 8865–8871 (2014). doi:10.1039/c4cp00352g

13. Xiang, H. *et al.* Block Copolymers under Cylindrical Confinement. *Macromolecules* **37**, 5660–5664 (2004).

14. Kalra, V. *et al.* Self-Assembled Structures in Electrospun Poly (styrene-b lock-isoprene) Fibers. *Macromolecules* **39**, 5453–5457 (2006).

15. Kalra, V. *et al.* Confined assembly in coaxially electrospun block-copolymer fibers. *Adv. Mater.* **18**, 3299–3303 (2006).

16. Kalra, V. *et al.* Controlling nanoparticle location via confined assembly in electrospun block copolymer nanofibers. *Small* **4**, 2067–2073 (2008).

17. Ma, M. *et al.* Gyroid-forming diblock copolymers confined in cylindrical geometry: A case of extreme makeover for domain morphology. *Macromolecules* **43**, 3061–3071 (2010).

18. Huang, Z. M., Zhang, Y. Z., Kotaki, M. & Ramakrishna, S. A review on polymer nanofibers by electrospinning and their applications in nanocomposites. *Compos. Sci. Technol.* **63**, 2223–2253 (2003).

19. Sun, G., Sun, L., Xie, H. & Liu, J. Electrospinning of Nanofibers for Energy Applications. *Nanomaterials* **6**, 129 (2016).

20. Greenfeld, I. & Zussman, E. Polymer entanglement loss in extensional flow: Evidence from electrospun short nanofibers. *J. Polym. Sci. Part B Polym. Phys.* **51**, 1377–1391 (2013).

21. Kim, Y. H. *et al.* Phase structure development in poly (styrene-co-acrylonitrile)/ poly (methyl methacrylate) blend under elongational flow. *Polymer.* **41**, 4747–4749 (2000).

22. Kwon, Y. K., Ko, Y. S. & Okamoto, M. Elongation flow-induced morphological change of a diblock copolymer melt of polystyrene and poly(ethylene propylene). *Polymer.* **49**, 2334–2341 (2008).

23. Kalra, V. & Joo, Y. L. Coarse-grained molecular dynamics study of block copolymer/nanoparticle composites under elongational flow. *J. Chem. Phys.* **131**, 214904 (2009).

24. Pan, Z., He, L., Zhang, L. & Liang, H. The dynamic behaviors of diblock copolymer/nanorod mixtures under equilibrium and nonequilibrium conditions. *Polymer.* **52**, 2711–2721 (2011).

25. Vananroye, A., Van Puyvelde, P. & Moldenaers, P. Structure development in confined polymer blends: Steady-state shear flow and relaxation. *Langmuir* **22**, 2273–2280 (2006).

26. Weeks, J., Chandler, D. & Andersen, H. C. Role of Repulsive Force in Determining the Equilibrium Structure of Simple Liquids. *J. Chem. Phys.* **54**, 5237 (1971).

27. Horsch, M. a., Zhang, Z., Iacovella, C. R. & Glotzer, S. C. Hydrodynamics and microphase ordering in block copolymers: Are hydrodynamics required for ordered phases with periodicity in more than one dimension? *J. Chem. Phys.* **121**, 11455–11462 (2004).

28. Park, J. H., Yin, J., Kalra, V. & Joo, Y. L. Role of nanoparticle selectivity in the symmetry breaking of cylindrically confined block copolymers. *J. Phys. Chem. C* **118**, 7653–7668 (2014).

29. Kalra, V., Mendez, S., Escobedo, F. & Joo, Y. L. Coarse-grained molecular dynamics simulation on the placement of nanoparticles within symmetric diblock copolymers under shear flow. *J. Chem. Phys.* **128**, 1–11 (2008).

30. Chremos, A., Nikoubashman, A. & Panagiotopoulos, A. Z. Flory-Huggins parameter χ, from binary mixtures of Lennard-Jones particles to block copolymer melts. *J. Chem. Phys.* **140**, 054909 (2014).

31. Daivis, P. J. & Todd, B. D. A simple, direct derivation and proof of the validity of the SLLOD equations of motion for generalized homogeneous flows. *J. Chem. Phys.* **124**, (2006).

32. Shinoda, W., Shiga, M. & Mikami, M. Rapid estimation of elastic constants by molecular dynamics simulation under constant stress. *Phys. Rev. B - Condens. Matter Mater. Phys.* **69**, 16–18 (2004).

33. Daivis, P. J. & Todd, B. D. A new algorithm for unrestricted duration

nonequilibrium MD simulation of planar elongational flow. *Comput. Phys. Commun.* **117**, 191–199 (1999).

34. Dobson, M. Periodic boundary conditions for long-time nonequilibrium molecular dynamics simulations of incompressible flows. *J. Chem. Phys.* **141**, 184103 (2014).

35. Plimpton, S. Fast Parallel Algorithms for Short – Range Molecular Dynamics. *J. Comput. Phys.* **117**, 1–19 (1995).

36. Montinaro, M. *et al.* Sub-ms dynamics of the instability onset of electrospinning. *Soft Matter* **11**, 3424–3431 (2015).

37. Park, W. I. *et al.* Directed self-assembly with sub-100 degrees celsius processing temperature, sub-10 nanometer resolution, and sub-1 minute assembly time. *Small* **8**, 3762–3768 (2012).

38. Williams, B. P. & Joo, Y. L. Tunable Large Mesopores in Carbon Nanofiber Interlayers for High-Rate Lithium Sulfur Batteries. *J. Electrochem. Soc.* **163**, A2745–A2756 (2016).

39. Park, J. H., Kalra, V. & Joo, Y. L. Controlling the dispersion and orientation of nanorods in polymer melt under shear: Coarse-grained molecular dynamics simulation study. *J. Chem. Phys.* **140**, (2014).

CHAPTER 4

LITHIUM-SULFUR NUMERICAL SIMULATIONS OF CATHODE MATERIAL PROPERTIES AND ELECTROCHEMICAL FAILURE MECHANISMS

As a potential alternative to the prevalent lithium-ion chemistry, lithium-sulfur (Li-S) batteries have received increasing attention due to their higher capacities and cheaper material costs. Despite these advantages, Li-S faces challenges such as polysulfide crossover, large volume changes in the cathode, and passivation of reaction sites which limit the capacity and capacity retention. To better understand these mechanisms and aid in the design of improved Li-S cathodes, a continuum-level Li-S numerical simulation was developed which includes reaction, mass transport, nucleation, and adsorption. The model was then used to investigate the effect of insulating lithium sulfide discharge precipitates on a two-region representation of the carbon cathode is studied. It is found that the cathode structure influences the deposition location of lithium sulfide precipitates, which can lead to incomplete utilization of the cathode if access to the interior of porous carbon particles is blocked off. The cathode adsorption of soluble polysulfide intermediates is then considered, which is critical for limiting the diffusion of intermediates and controlling deposition. Finally, the failure mechanisms at the end of discharge were investigated. It is found that when the discharge rate is varied within a single discharge, different carbon cathode processing can lead to different behavior due to passivation vs. mass transport failure mechanisms.

4.1 Introduction

New applications for energy storage technology in electric transportation have led researchers to search for alternatives to the current state-of-the-art lithium-ion (Li-ion) batteries.[1] Numerous possible research directions are plausible, including improving Li-ion battery anodes by adding silicon nanoparticles and aqueous chemical flow batteries like vanadium and zinc bromine.[2–5] Among these, lithium-sulfur batteries (Li-S) stand out as one of the most promising options due to their high theoretical specific energy of 2510 W H kg^{-1} and similarities in cell design to Li-ion that can ease commercialization.[6] Li-S also benefits from low cost and plentiful supply of sulfur which removes the need for the relatively scarce cobalt frequently used in Li-ion battery cathodes.

Despite their promise, Li-S batteries must overcome a number of challenges in order to reach commercial viability. First, intermediate lithium polysulfide species formed during the electrochemical conversion of sulfur have high solubility in the battery electrolyte, allowing movement away from reaction sites in the cathode and leading to side reactions at the anode.[7–11] Second, lithium sulfide discharge products are insulating, requiring the use of conductive carbon host materials and limiting the sulfur loading and energy density of the battery.[12–14] Third, the sulfur to lithium sulfide conversion during discharge also involves a 79% volume expansion which can damage the cathode structure over many cycles.[15,16] Li-S research has focused in large part in developing strategies that reduce or eliminate these challenges.

Towards this end, researchers have focused on the material properties of the sulfur-carbon composite host. The carbon must have high surface area and porosity to achieve good battery performance and capacity retention.[2,17] In addition to providing reaction sites for charge transfer reactions and volume for lithium sulfide expansion, well-designed carbon hosts can also limit the diffusion of the polysulfide intermediates out of the cathode. Such carbon structures include hollow carbon nanofibers, hollow carbon spheres, carbon bowls, and nitrogen-doped carbon, all of which demonstrate improved battery performance.[12,16,18,19] These carbons act as a trap for polysulfides and prevent them from undergoing side reactions at the anode or depositing as lithium sulfide in an inefficient location. Other work has focused on finding non-carbon adsorption agents which can be added to the carbon host to improve the adsorption properties. Wu et al. investigated a large variety of candidate metal oxide materials and determined MnO_2 as an effective polysulfide adsorbent.[20] Lui et al. used a SnO_2 interlayer which showed improved capacity retenetion.[21] Other groups used CoS_2 mixed into the carbon cathode, which showed strong affinity for lithium polysulfide species in density functional theory simulations.[22,23]

Numerical simulations provide a valuable tool for understanding Li-S battery behavior, but the effect of cathode structure and adsorption properties has not been adequately explored.[24,25] In this study, a two region cathode structure combined with adsorption kinetics is used with a passivation-based discharge failure condition to better model these aspects of the Li-S battery. The passivation failure condition follows the method proposed by Andrei et al., who built on the work of previous Li-S and Li-air simulations.[26–28]

In addition to investigating structural and adsorption properties, we build on the work of Andrei et al. and Zhang et al., who have proposed two contrasting failure mechanism explanations.[29] Understanding the reason why Li-S cannot reach their full theoretical capacity is critical for improving their performance. Andrei et al. contends with experiments and simulation that end-of-discharge is triggered by the passivation of the cathode with insulating lithium sulfide, while Zhang et al. proposes a mass transport limited model related to the clogging of the cathode with lithium sulfide deposits. These two mechanisms show different characteristic behaviors when discharge rate is varied during a single discharge. We show that based on the cathode processing method and properties, both behaviors can be observed, implying that both failure mechanisms are correct under certain circumstances and the prevalence of one failure mechanism over another depends on the cathode properties.

4.2 Theoretical model

4.2.1 Electrochemical and precipitation reactions

During discharge, elemental sulfur (S_8) is converted into successive lithium polysulfides (Li_2S_x) until finally forming lithium sulfide (Li_2S) The full diversity of lithium polysulfides that may exist in the battery is not fully understood; however, it has been shown by previous models that the characteristic discharge behavior can be captured with a limited subset of electrochemical reactions.[24] In our model, we use four polysulfide electrochemical reactions and consider the dissolution of S_8 and the precipitation of Li_2S as additional separate reactions. The remaining polysulfide species are assumed have negligible precipitation, which is supported by experimental work.[30] The electrochemical and precipitation reactions occurring at the cathode are listed below:

$$\mathrm{S}_8^{(\mathrm{s})} \rightleftharpoons \mathrm{S}_8^{(\mathrm{l})}$$

$$\mathrm{S}_8^{(\mathrm{l})} + \mathrm{e}^- \rightleftharpoons \mathrm{S}_8^{2-}$$

$$\frac{3}{2}\mathrm{S}_8^{2-} + \mathrm{e}^- \rightleftharpoons 2\mathrm{S}_6^{2-}$$

$$\mathrm{S}_6^{2-} + \mathrm{e}^- \rightleftharpoons \frac{3}{2}\mathrm{S}_4^{2-}$$

$$\frac{1}{3}\mathrm{S}_4^{2-} + \mathrm{e}^- \rightleftharpoons \frac{4}{3}\mathrm{S}^{2-}$$

$$\mathrm{S}^{2-} + 2\mathrm{Li}^+ \rightleftharpoons \mathrm{Li}_2\mathrm{S}^{(\mathrm{s})}$$

The first two reaction occur at the beginning of discharge in the first plateau region of the typical Li-S discharge curve. The third and fourth reactions then occur in the downward sloping region after the first plateau once the elemental sulfur is consumed, and the fifth and sixth reactions occur during the second plateau region once the longer chain polysulfides are consumed.

At the anode, lithium ions are produced at a rate determined by the applied current *I* with the following reaction:

$$\mathrm{Li}_\mathrm{s} \rightleftharpoons \mathrm{Li}^+ + \mathrm{e}^-$$

The lithium salt anion is denoted as A^-, which would be bis(trifluoromethanesulfonyl) imide in our electrolytes. As solid species are dissolved or precipitated, their volume fractions ε_i change with time *t* according to Equation 1:

$$\frac{\partial \varepsilon_i}{\partial t} = \frac{M_i}{\rho_i} \sum_m a_s v_{i,m} r_m \quad (1)$$

where M_i is molecular weight of solid species i, ρ_i is the density, a_s is the specific surface area, $v_{i,m}$ is the stoichiometric coefficient for species *i* in reaction m, r_m is the reaction rate of reaction m for the two precipitation reactions (reactions 1 and 6 in Table 4.1). We use subscript *i* to denote species and subscript *m* to denote reactions Values of density and molecular weight are listed in Table 4.1, and stoichiometric coefficients are taken from the coefficients in the reactions with reactant side values being negative. Values of surface area and other structural parameters can be found in Table 4.2. The volume fraction of electrolyte, ε, is calculated directly from volume fraction of all precipitated species plus the volume fraction of carbon subtracted from 1, seen in Equation 2:

$$\varepsilon = 1 - \varepsilon_c - \sum \varepsilon_i \qquad (2)$$

where ε_c is the volume fraction of solid carbon or separator in the cell. Reaction rates for each electrochemical cathode reaction (reactions 2-5) are defined by a modified passivation limited Butler-Volmer equation in Equation 3:

$$r_m = k_m \left(a_{re} a_{prod}\right)^{0.5} (1-\theta)\left(e^{-\frac{1}{2RT}\Delta\mu_m} - e^{\frac{1}{2RT}\Delta\mu_m}\right) \qquad (3)$$

where r_m is the reaction rate, k_m is a reaction constant, $r_{l,c}$ is a limiting reactino rate, R is the gas constant, T is temperature, θ is the surface coverage fraction of lithium sulfur, and $\Delta\mu_m$ is the change in chemical potential for reaction m. As θ approaches 1, reactions will be unable to progress due to the nonconductivity of the entire cathode. It should be noted that r_m is scaled by the cathode surface area with units of mol $m^{-2}s^{-}$

[1]. a_{re} and a_{prod} represent the activities of reactants and products respectively, as used in Danner et. al.[31] Symmetry and acitivity coefficients were assumed to be 0.5 and 1 respectively. This form of the Bulter-Volmer equation was adapted from Bazant.[31,32]

For electrochemical reactions, the change in chemical potential and equilibrium voltage is given in Equations 4 and 5 [31,32]:

$$\Delta\mu_m = n_m F(\phi_{cathode} - U_{eq,m}) \qquad (4)$$

$$U_{eq,m} = U_{eq0,m} + RTln(\frac{a_{re}}{a_{prod}}) \qquad (5)$$

where n_m is the number of electrons per reaction, F is the Faraday constant, $\phi_{cathode}$ is the voltage of the carbon cathode, $U_{eq,m}$ is the open circuit potential for reaction *m*, and $U_{eq0,m}$is the open circuilt potential at reference conditions. Sulfur (S_8) and lithium sulfide (Li_2S) undergo precipitation/dissolution reactions with $\Delta\mu_m$ given by Equation 6 instead:

$$\Delta\mu_m = RTln(K_{sp,m}\frac{a_{prod}}{a_{re}}) \qquad (6)$$

where $K_{sp,m}$ is the solubility product for precipitation reaction *m*. Parameters used in reactions are listed in Table 4.1.

4.2.2 Governing equation and mass transport

Changes in concentration of each species depend on mass transport and reaction terms, as shown in Equation 7:

$$\frac{\partial}{\partial t}(\varepsilon c_i) = -\frac{\partial N_i}{\partial z} + \sum_m a_s v_{i,m} r_m \qquad (7)$$

where N_i is the mass flux of species *i* and *z* is the distance dimension between anode and cathode. Our model assumes that transport is purely diffusive due to the computational difficulty of including migration with the inner-outer discretization approach (Section 4.2.4). This assumption has been also used by a previous model with a similar discretization scheme.[33] With this assumption, the flux is given Fick's Law in Equation 8:

$$N_i = -D_{eff,i}\frac{\partial c_i}{\partial z} \qquad (8)$$

where $D_{eff,i}$ is the effective diffusion coefficient. This value is found by adjusting the diffusion coefficient based on porosity using the Bruggeman correlation in Equation 9 [24,34]:

$$D_{eff,i} = D_{0,i}\ \varepsilon^{\beta} \qquad (9)$$

where $D_{0,i}$ is the bulk diffusion coefficient and β is the Bruggeman coefficient.

4.2.3 Cell voltages

The total current I, which is determined externally by the rate of discharge, can be found by integrating all electrochemical reactions over the total cell length l_c:

$$I = \int_0^{l_c} \left(\sum_m -n_m F a_{s,m} v_{i,m} r_m\right) dz \qquad (10)$$

Equation 11 can be solved numerically to find $\phi_{cathode}$ using I and the current concentrations of species. The total cell voltage can be found from the difference of cathode and anode voltages:

$$V_{cell} = \phi_{cathode} - \phi_{anode} \qquad (11)$$

The anode voltage is estimated in Equation 13 using Nernst's equation for lithium metal oxidation[33]:

$$\phi_{anode} = \frac{RT}{F} ln(\frac{c_{Li+,anode}}{c_{Li+,ref}}) \qquad (12)$$

where $c_{Li+,ref}$ is the reference concentration for lithium ion.

4.2.4 Cell structure and numerical implementation

We use a 1-dimensional + time numerical approach which models the Li-S full cell. Due to symmetry in the cell structure, we assume that only the dimension separating the anode and the cathode is relevant. The governing equations are discretized using Finite Difference Method (FDM) to form N=11 segments using Equation 13:

$$\frac{d^2}{dz^2}(C_i) = c_{i,j}\frac{c_{i,j+1}-2c_{i,j}+c_{i,j-1}}{dzdz} \qquad (13)$$

where j is the discretized box index and dz is the distance between boxes. For box j=1, no-flux boundary conditions are applied in the negative z direction using an FDM variant:

$$\frac{d^2}{dz^2}(C_i) = c_{i,j}\frac{c_{i,j+1}-c_{i,j}}{dzdz} \qquad (14)$$

Variants of this form are also used for box N=1 and for the diffusion occurring between the inner and outer regions.

The system of equations for concentration, porosity, nuclei growth rate, and nuclei was solved in Matlab using the ode15s stiff solver. The stiff solver was necessary to handle the large number of varying reaction and diffusion timescales present in the system. Initial conditions for concentration and volume fraction are listed in Table 4.2. The cell structure is characterized by its porosity, specific surface area, and Bruggeman coefficient, with parameters given in Table 4.3. In order to represent the spherical nature of carbon particles, we construct inner boxes in the cathode region that are each connected to a single outer box, shown in Figure 4.1, which are separated from each other by distance l_{io}. The inner box represents the interior of a porous carbon particle, and the outer box represents the exterior of the carbon particle and the surrounding electrolyte. Therefore, species must first travel through the outer boxes and then may travel from an outer box in the cathode into an inner box. The inner boxes have high surface area and tortuosity reflecting the nm-sized pores present in the Ketjen Black carbon used in our experiments. Solid sulfur exists only in the inner cathode region at time 0 to reflect impregnation into porous carbon material. A related discretization approach was published previously by Thangeval et al.[33]

Parameters for the model are taken from experimental sources where possible, but many parameters are not accurately known. In these cases, we assume parameters based on agreement between simulation discharge curves and previously published experimental discharge curves.[26]

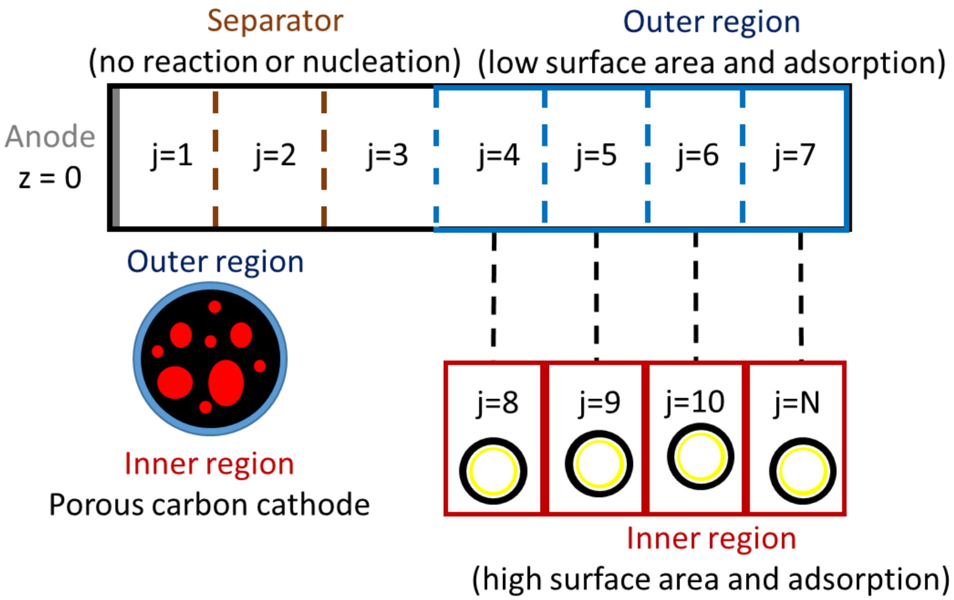

Figure 4.1 Numerical discretization of a lithium-sulfur cell. Diffusion to inner regions only occurs from the corersponding outer region. Inner regions have higher surface area and adsorption or polysulfides compared to outer regions, and transport from outer regions to inner regions diminishes as the outer region becomes passivated.

Table 4.1 Reaction parameters k_m (reaction rate constant), n_m (electrons per reaction), $U_{eq0,m}$ (open circuit voltage at reference conditions), and $K_{sp,m}$ (solubility product) in the passivation limited model. ^{a}Assumed parameters.

Reaction	**Index *m***	**k_m (mol m^{-2} s^{-1})**	**n_m**	**$U_{eq0,m}$ (V)**	**$K_{sp,m}$**
$S_8^{(s)}$ to $S_8^{(l)}$	1	6.72^{a}	0	-	1/19[31]
$S_8^{(l)}$ to S_8^{2-}	2	$2\cdot10^{-8,a}$	1	2.39 ^{a}	-
S_8^{2-} to S_6^{2-}	3	$2\cdot10^{-9,a}$	1	2.37 ^{a}	-
S_6^{2-} to S_4^{2-}	4	$2\cdot10^{-9,a}$	1	2.24 ^{a}	-
S_4^{2-} to S^{2-}	5	$2\cdot10^{-9,a}$	1	2.04 ^{a}	$1\cdot10^{-4}$[31]
S^{2-} to $Li_2S^{(s)}$	6	$1.2464\cdot10^{-4,a}$	0	-	-

Table 4.2 Bulk diffusion coefficient ($D_{0,i}$), molecular weight (M_i), density (ρ_i), initial concentration ($c_{0,i}$), and initial volume fraction ($\varepsilon_{0,i}$) for molecular species in the passivation limited model. [a]Assumed parameters.

Species i	**$D_{0,i}$ (m^2s^{-1})**	**M_i (kg mol^{-1})**	**ρ_i (kg m^{-3})**	**$c_{0,i}$ (mol m^{-3})**	**$\varepsilon_{0,i}$**
S_8 (s)	0	0.2565[31]	2070.4[31]	-	0.2 [a]
S_8	$1\cdot10^{-9}$[a]	-	-	17.0 [a]	-
S_8^{2-}	$2.6\cdot10^{-10}$[35]	-	-	$1\cdot10^{-7}$[a]	-
S_6^{2-}	$1.7\cdot10^{-10}$[35]	-	-	$1\cdot10^{-7}$[a]	-
S_4^{2-}	$1\cdot10^{-10}$[a]	-	-	0.02416 [a]	-
S^{2-}	$8.6\cdot10^{-11}$[a]	-	-	$1\cdot10^{-9}$[a]	-
Li_2S (s)	0	0.0459 [31]	1659.9 [31]	-	0.0001 [a]
Li^+	$4\cdot10^{-10}$[a]	-	-	1000	-
A^-	$1.24\cdot10^{-10}$ [36]	-	-	1000	-

Table 4.3 Structural and miscellaneous parameters for the passivation limited model. [a]Assumed parameters.

Symbol	**Description**	**Value**	**Units**
N	Total number of discretized segments	11	-
N (inner)	Number of segments in the outer cathode region	4	-
N (outer)	Number of segments in the inner cathode region	4	-
l_c	Length of cell	$4\cdot10^{-5}$[a]	m
l_{io}	Distance between inner and outer regions	$1\cdot10^{-6}$[a]	m
$a_{s0,in}$	Specific surface area in the inner region	$3.6\cdot10^{8}$[a]	m^2m^{-3}
a_s(outer)	Specific surface area in the outer region	$4\cdot10^{7}$[a]	m^2m^{-3}
β (inner)	Bruggeman coefficient in the inner region	10[a]	-
β (outer)	Bruggeman coefficient in the outer region	1.5[24]	-
ε_c	Carbon volume fraction in cell	0.2[a]	-
R	Gas constant	8.314	J K^{-1} mol^{-1}
T	Temperature	298.15	K
F	Faraday constant	96485	A mol^{-1}

4.2.5 Nucleation and growth of lithium sulfide

In general, the passivation limited model is based upon the work of Andrei et al. and Ren et al. and was expanded to be used with the inner-outer model.[26,27] During the second plateau of the lithium sulfur discharge curve, lithium sulfide is produced at the cathode and deposits soon after due to its low solubility in the organic electrolyte. Lithium sulfide has low conductivity which causes layers greater than 10nm thick to be fully insulating towards electrons.[33] Therefore, electrochemical charge transfer reactions will not be able to take place on regions of the cathode covered with lithium sulfide deposits, leading to complete passivation of the cathode in the extreme case. This means that the nucleation and growth of lithium sulfide nuclei could be important in the behavior of the cell near the end of discharge. We assume that lithium sulfide is the only depositing and nucleating sulfur species for simplicity, although in reality solid Li_2S_2 is also likely to be present.

The location of lithium sulfide deposition in the porous carbon cathode structure will affect the passivation process. In the inner-outer model, a spherical porous carbon particle is represented by a low surface area outer region and a high surface area inner region. Sulfur and lithium species can only travel from the outer region to reach the inner region. Depending on where lithium sulfide deposits, either portion of the cathode could become passivated first. If too much lithium sulfide covers the outer region of the particle, the inner regions will become completely blocked off, preventing further reactions. By combining the inner-outer model and nucleation and growth behavior, the structure and geometry of the carbon cathode can be more realistically modeled.

Table 4.4 Nucleation and adsorption parameters for the passivation limited model. [a]Assumed parameters.

Symbol	**Description**	**Value**	**Units**
P_0	Base nucleation rate	1.5[a]	nuclei m^{-2}s^{-1}
λ	Boundary layer mass transport parameter	$1\cdot10^{-16,a}$	s m^{-1}
N_0	Nucleation exponential fitting parameter	1.2[a]	-
φ	Adsorption fraction parameter	0 to 1[a]	-
k_a	Langmuir adsorption rate constant	$1\cdot10^{-6}$ to $1\cdot10^{-9,a}$	m^3 s^{-1}
k_d	Langmuir desorption rate constant	$1\cdot10^{-9,a}$	s^{-1}
c_{max} (outer)	Maximum adsorbed polysulfide concentration in outer region	100	mol m-^{3}
c_{max} (inner)	Maximum adsorbed polysulfide concentration in inner region	700	mol m-^{3}

To model the nucleation and growth of lithium sulfide nuclei during discharge, we rely on the overstaturation model proposed by Andrei et al[26]:

$$P = a_s V P_0 \left(\left[C_{Li^+}^2 (C_{S^{2-}} - \lambda R_{S^{2-}prod.}) K_{sp}\right]^{N_0} - 1\right)\frac{1}{1-\theta} \qquad (15)$$

where P = nucleation rate (nuclei/s), a_s is the specific surface area, V is the volume of the discretized box, P_0 is the initial nucleation rate, θ is the lithium sulfide surface coverage, K_{sp} is the solubility product, N_0 is a fitting parameter, λ is a boundary layer parameter, and R is the S^{2-} reaction rate. Values for nucleation parameters are listed in Table 4.4. In this model, the nucleation rate is governed by the oversaturation of S^{2-} ions at the cathode surface. In addition to solubility, this oversaturation is dependent on the difference between the bulk concentration and the rate the S^{2-} is being produced at the cathode surface. If mass transport of S^{2-} in the boundary layer is fast compared to reaction, oversaturation will be minimal leading to slower nucleation. Otherwise, as $\mathrm{S}^{2-}$is produced quickly at the surface it will be forced to deposit in a new nuclei instead of having sufficient time to diffuse to an existing nuclei to precipitate. This allows the model to predict variations in nuclei size for varying discharge rates, which has been observed in experiment for Li-S batteries.[27] At high C-rates higher than 0.5C or 1.0C, thin films of lithium sulfide have been observed due to the fast reaction and nucleation, while at lower C-rates large individual nuclei have been observed instead. The prefactor for the equation reflects that the nucleation rate is also influenced by the number of nucleation sites on the carbon surface, which scale with surface area.

Once nuclei are created, they are assumed to be hemispherical. It is also assumed that nuclei grow evenly and that all nuclei that exist in the cathode grow at the same radial rate.[28] These assumptions are necessary to limit the complexity of the problem. Each individual nuclei's radius *r* is tracked in the simulation, and their radius' change based on the following equation[27]:

$$\frac{dr}{dt} = \frac{V}{2(1-\theta)\pi \sum_{all\, nuclei} r^2} \qquad (16)$$

which follows from the assumption that all nuclei grow at the same rate. The surface coverage θ can be found from the following equation[28]:

$$\theta = 1 - e^{-\frac{\pi}{a_s}\sum_{all\, nuclei} r^2} \qquad (17)$$

This equation is based off of Kolmogorov's 2d phase transformation, which accounts for the portion of hemispherical nuclei that will overlap as they grow in size. θ is calculated separately for each finite difference discretization box, and cell failure due to passivation will begin to occur as it approaches 1. To model the inaccessibility of inner region reaction sites as the outer region is covered with lithium sulfide, we use the following equation to adjust the inner region θ_{in}:

$$a_{s,in} = a_{s0,in}(1 - \theta_{out})(1 - \theta_{in}) \qquad (18)$$

where θ_{out} is the outer region surface coverage. Thefore, if the outside of the spherical particle is completely coated with lithium sulfide, the entire particle will be regarded as inactive due to the inabiality of lithium ions to reach the inner region reaction sites.

4.2.6 Adsorption model

Adsorption of polysulfide species was added to the passivation limited model to investigate how the location of polysulfides in the cathode influences the lithium sulfide deposition and the battery performance. First, a crude adsorption model was used that assumes that adsorption is fast compared to diffusion and reaction and that the quantity polysulfide adsorbed is proportional to the bulk concentration. This can be represented by the following equation:

$$c_{i,ads} = \varphi c_i \qquad (19)$$

where $c_{i,ads}$ is the amount of mol per unit volume of sulfur anion adsorbed to the cathode carbon surface and φ is the proportionality parameter. As φ is challenging to calculate experimentally due to the sensitivity of polysulfides to air and water, we instead varied the parameter in simulation to investigate the effect of weakly and strongly adsorbing cathode materials. Concentration that is adsorbed is considered to be the same as bulk concentration except that it does not participate in diffusion calculations due to its immobility. In addition, lithium ions are adsorbed at a concentration of twice the adsorbed sulfur anion concentration to represent the charge-neutral polysulfide molecule.

To improve upon the simplistic model above, time dependence was added by implementing a Langmuir adsorption differential equation:

$$\frac{dc_{tot,ads}}{dt} = k_a c_{tot}\left(c_{max} - c_{tot,ads}\right) - k_d c_{tot,ads} \qquad (20)$$

Where c_{tot} total amount of sulfur anion concentration, is the c_{max} is the maximum possible adsorbed concentration in the carbon, k_a is the rate constant for adsorption, and k_d is the rate of desorption. As k_a and k_d are not known, a range of values were tested. Values for adsorption parameters are listed in Table 4.4. Due to most experimental researchers relying on pseudo first-order or pseudo second –order models, it is difficult to find parameters to compare to k_a and k_d. The equation is applied only to the soluble S_4^{2-}, S_6^{2-}, and S_8^{2-} species. For simplicity the rate of adsorption for each individual species compared to the total rate of adsorption $\frac{dc_{tot,ads}}{dt}$ is assumed to be proportional to their relative concentrations. c_{max} was estimated roughly based on polysulfide adsorption experiments perfomred by Song et al., who found a maximum adsorption of 0.2g polysulfide per g carbon.[37] The a inner-outer c_{max} ratio was assumed to be the same as the inner-outer surface area ratio.

4.3 Experimental methods

4.3.1 Lithium sulfide slurry cast cathode preparation and testing

Sulfur powder (S, 1.5 g) was ground with Ketjen Black EC600JD (KB, 0.5g, AkzoNobel) to get a 75:25 S:KB mixture. Then the mixture was heat treated at 155°C for at least 12 h to ensure sulfur impregnation into the porous KB particles.[38] The active material S/KB was then thoroughly mixed for 3h with Super C-65 (MTI Corp.) and the binder polyvinylidene fluoride (PVDF, Aldrich) in N-methyl-2-pyrrolidone (NMP, BDH), in the weight ratio of 70:20:10, respectively. The slurry was cast onto aluminum foil using doctor blade and the sheets were dried in a fume hood at room temperature overnight followed by heat treatment at 60°C oven. The total thickness of aluminum + cathode was 54 microns, and sulfur areal loading was around 1mg cm^{-2} for all cells.

All cells (2032 type) were assembled in an argon filled glovebox. A typical cell consisted of a lithium metal disc (Alfa Aesar) as anode, a S/KB slurry cast as cathode, and a Celgard 2400 separator (25 micron thickness). The electrolyte was 1M (LiTFSI, Sigma-Aldrich) and 0.1M $LiNO_3$ (Sigma-Aldrich) in a 1:1 volume ratio of dioxolane (DOL, Sigma-Aldrich) and dimethoxyethane (DME, Sigma-Aldrich).[39] Galvanostatic charge-discharge measurements were performed using a MTI Corporation battery cycler at room temperature. The cycling was conducted using a multi C-rate discharge method after the 20th cycle. The battery was first discharged at 0.2C until it reached half of its total capacity. Then, the battery was discharged at 1.0C until it reached 1.8V, after which it was discharged at 0.2C again until 1.8V. Charging was then conducted normally at 0.2C.

4.3.2 Air-assisted electrospray cathode preparation

In contrast to the slurry cast method, cathodes were produced by electrospraying the S/KB material with polymer binder. The S/KB material was prepared using the same impregnation procedure as for the slurry cast. The KB/S mixture, graphene for conductivity, and polyacrylic acid as binder were dispersed at a 7:2:1 mass ratio in water and IPA at 7:3 volume ratio to yield a 6% solid content. The solution was then sonicated for one hour to disperse. The dispersed sulfur-carbon solution was allowed to rest for 24 hours at room temperature before use.

Air controlled electrospray is a process which uses air flow and high voltage to atomize a jet of liquid ejected from a nozzle. Using this process the Li-S cathode solution was sprayed onto a carbon coated aluminum foil using a coaxial needle (12-guage inside, 16-guage outside). The infusion rate and needle to collector were 0.04 ml min^{-1} and 10 cm, respectively. The voltage and air pressure were 25 kV and 10 psi, respectively. After the first layer was sprayed, the cathode was dried under room temperature conditions for approximately 4 hours. To add the additional graphene layer, a graphene-water solution (4 wt%) was sprayed using the same coaxial needle at an infusion rate and distance of 0.05 ml min^{-1} and 20 cm, respectively. The voltage and air pressure conditions were 25 kV and 25 psi, respectively. The finished cathode was dried under room temperature conditions for four hours and subsequently heat treated in a 60 degrees Celsius oven.

4.3.3 Lithium polysulfide adsorption test

Under an argon atmosphere, elemental sulfur and lithium sulfide were mixed in a 5:1 molar ratio. The mixture was then added to a 1:1 volume ratio of DME and DOL to form a 0.2M lithium sulfide solution. The solution was heated on a hot plate at 80C for 12hrs to produce a deep orange/brown polysulfide solution. According to the 5:1 stoichiometric ratio, Li_2S_6 should be the reaction product. However, in reality a mixture of longer and shorter polysulfides will be formed with an average size of size sulfur atoms. To conduct the adsorption test, the 0.2M solution was diluted to 4mM, and 10mg of carbon were added to 5mL of the 4mM solution. After allowing to rest for 24hrs, the solution color was compared to evaluate the carbon adsorption of polysulfides. It is also important to note that the polysulfides will degrade under air and water and even in the argon atmosphere only lasted 1-2 weeks.

4.4 Results and Discussion

4.4.1 Simulated effect of cathode structural properties on Li-S discharge

First, the passivation limited model without adsorption was tested for multiple carbon cathode surface areas, shown in Figure 4.2. The capacity is scaled by the mass of sulfur in the system. The C-rate determines the rate of discharge, and is equal to the numer of discharges per hour.

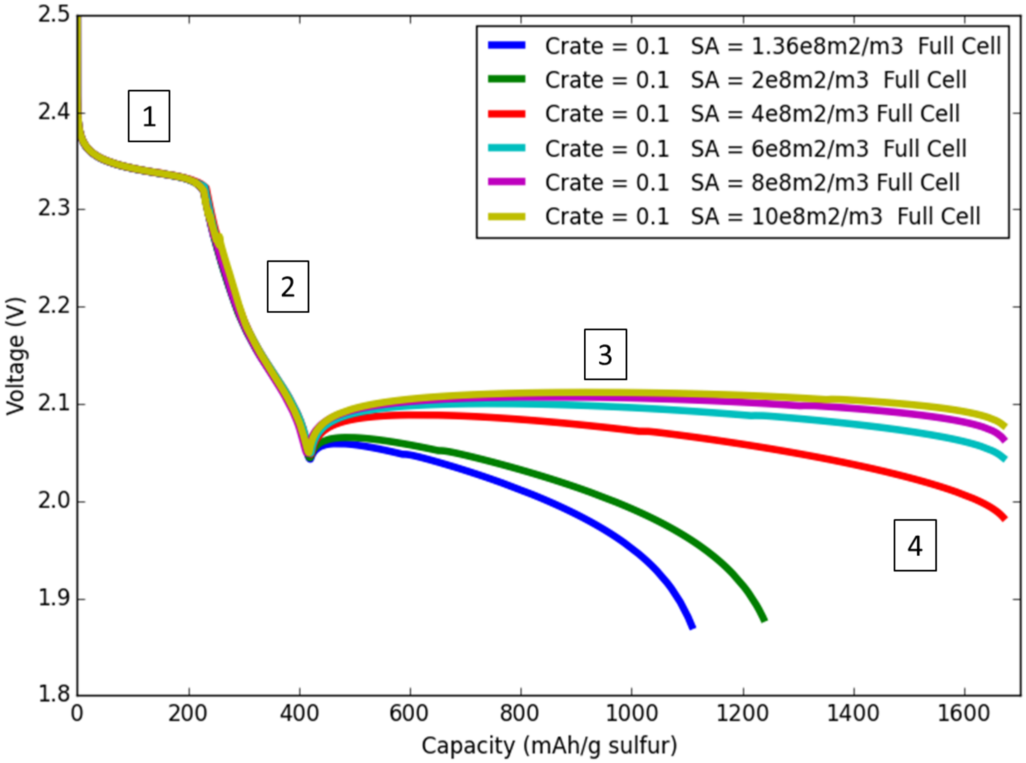

Figure 4.2 Passivation limited model at 0.1C discharge for varying cathode surface areas. Marked numbers correspond to different discharge regions.

The discharge voltage vs. capacity curves in simulation reproduce the general shape of Li-S curves. This consists of an initial plateau in region 1 with voltage around 2.3-2.4V corresponding to elemental sulfur conversion, followed by region 2 with a steep voltage decline corresponding to long chain polysulfides Li_2S_{6-8} conversion into the shorter Li_2S_4. The dip in voltage around 400 mAg/g sulfur is caused by the onset of nucleation, and is often seen in experimental results as well. As Li_2S_4 is converted into Li_2S, initially the Li_2S concentration increases despite its insolubility due to the energy barrier in creating the first Li_2S nuclei on the carbon surface. After these first nuclei are formed, the voltage recovers and remains relatively constant through region 3 until the end of discharge region 4, reflecting the continual deposition of Li_2S. Comparing the varying surface areas, it can be immediately seen that the first two discharge regions show almost no difference with varying surface area. This is due to the low overpotentials in our model for these reactions. In region 3, surface area has a greater effect due to its importance for the passivation condition. The surface coverage θ depends on the surface area, so with a large surface area passivation is negligible in the model. This leads specific surface areas of $4 \cdot 10^8$ m^2m^{-3} and greater to achieve the full sulfur theoretical capacity of 1672mAh/g. Surface areas smaller than this cannot achieve their full capacity due to the premature passivation of the cathode which prevents further electrochemical reactions. Figure 4.2 confirms that passivation is not the only mechanism responsible for the difficulty of experimental Li-S batteries to achieve their full theoretical capacity, as even batteries constructed with very high carbon surface areas and low sulfur loading still fall short of the theoretical capacity.

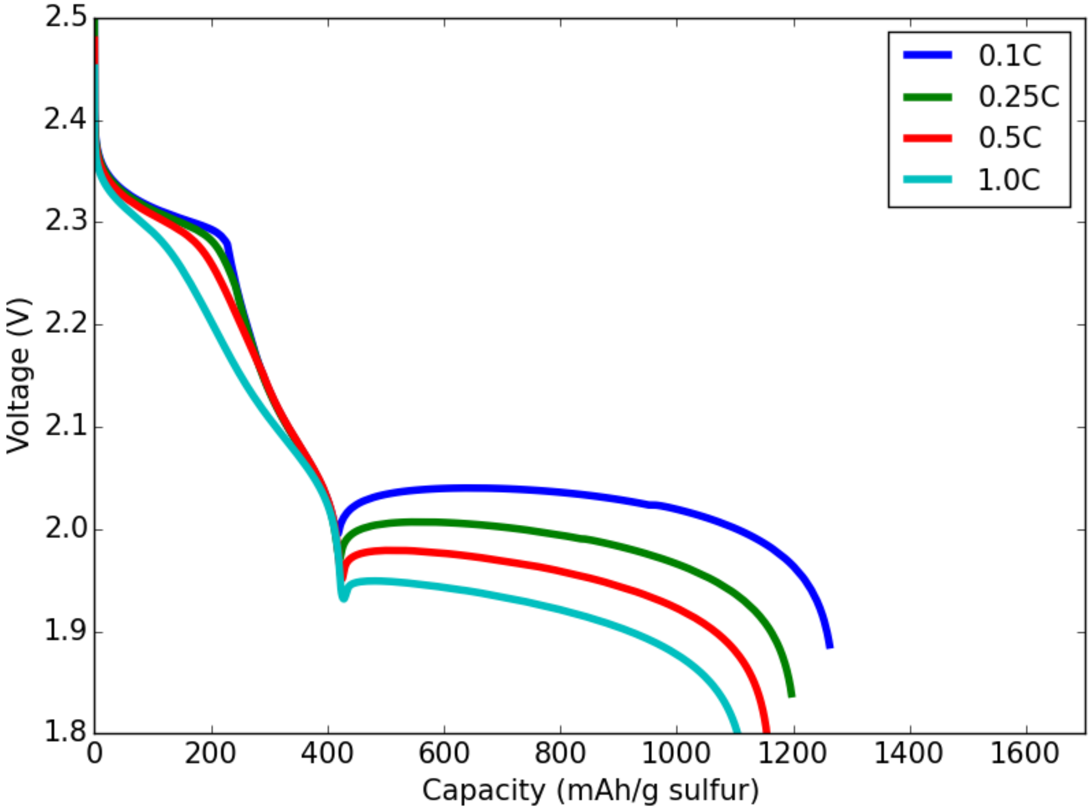

Figure 4.3 Passivation limited model at varying discharge rates.

Further refinement of the model led to Figure 4.3, which is plotted for four different C-rates. In agreement with typical experimental results and electrochemical theory, at faster C-rates voltages are lower due to higher overpotential. In addition, the passivation model predicts decreasing capacity at faster C-rates due to the increased number of nuclei formed, which leads to faster passivation.[27] The total capacity depends on the values of the nucleation parameters in Table 4.4. As these are unknown experimentally and assumed in the model, the model cannot make quantitative predictions of capacity. However, it can still be used to show the effects of varying cathode compositions and properties.

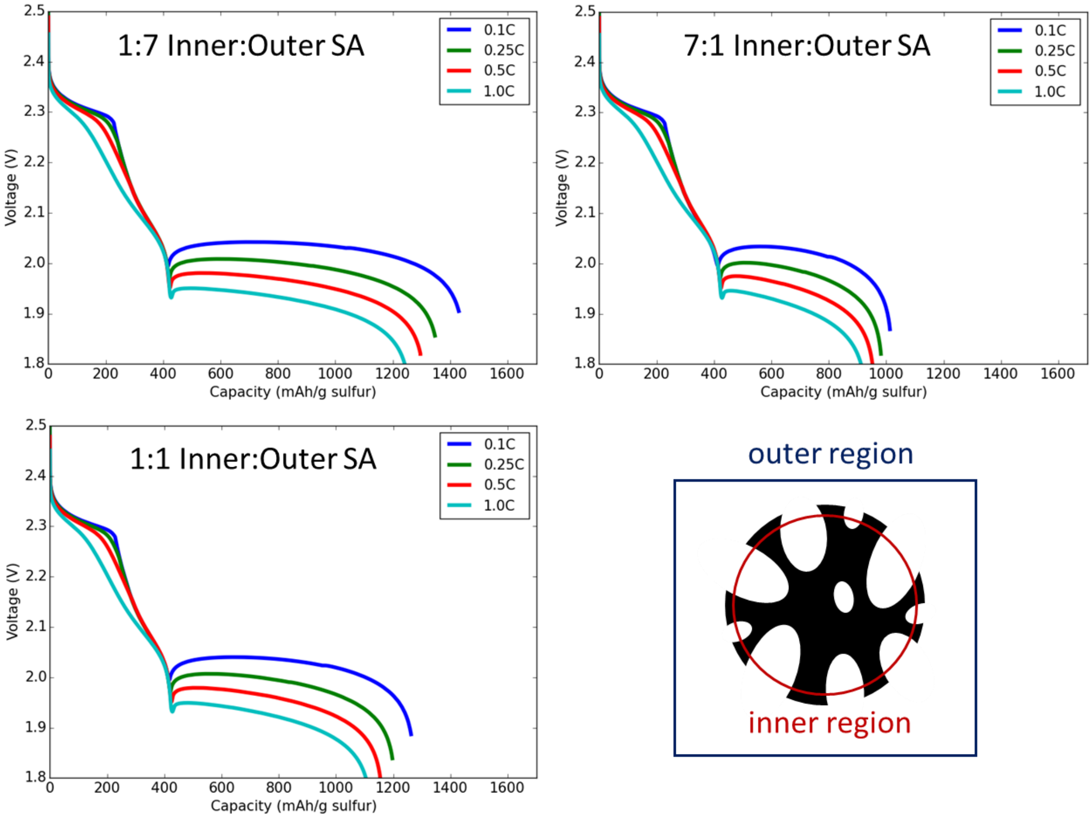

Figure 4.4 Passivation limited model for varying inner:outer surface area ratios and multiple C-rates. The total surface area is kept constant.

Using the inner-outer model, hypothetical carbon cathode materials with inner:outer surface area ratios can be simulated. For example, a large inner:outer ratio corresponds to a highly porous spherical carbon particle. A smaller inner:outer ratio corresponds to a less porous carbon particle. Figure 4.4 shows that when surface area is kept constant, higher capacity is achieved when surface area predominantly in the outer surface area rather than inner surface area. This is due to the blockage of the carbon particle when the outer region becomes passivated. If the outer region has very low surface area, it will become passivated quickly and prevent full utilization of the inner region.

However, it is important to note that for a real material, a decrease in the inner surface would likely correspond to a decrease in the total surfae area of the particle.

4.4.2 Adsorption model

A promising approach towards preventing the passivation of the outside of cathodes particles is to prevent polysulfides from leaving the inner pores. This can be achieved by designing carbon materials that have strong adsorptive properties towards polysulfides, which will trap the polysulfide in the inner region for the duration of the discharge. This has been achieved using hollow carbon nanospheres with sulfur inside, for example.[12] Therefore, it is relevant to include this behavior in the model, which to the author's best knowledge has not been done before for Li-S numerical simulations.

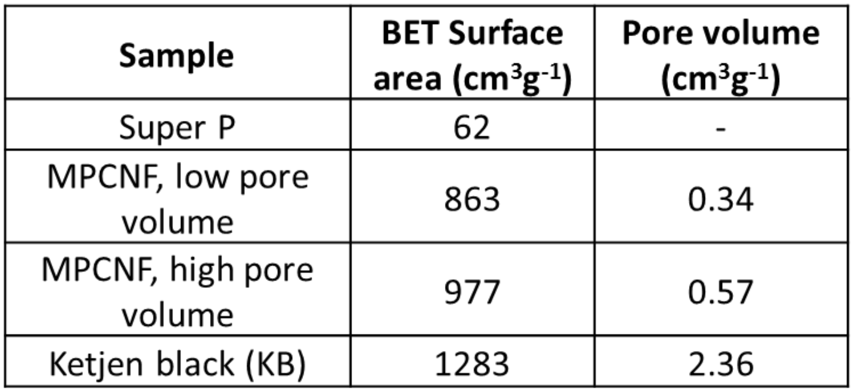

Sample	BET Surface area (cm^3g^{-1})	Pore volume (cm^3g^{-1})
Super P	62	-
MPCNF, low pore volume	863	0.34
MPCNF, high pore volume	977	0.57
Ketjen black (KB)	1283	2.36

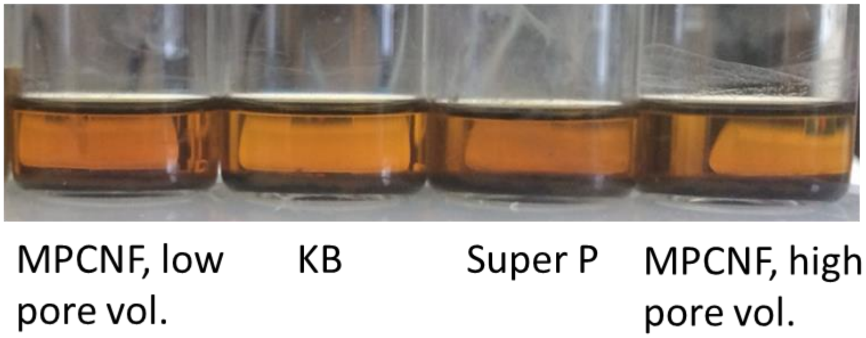

Figure 4.5 Polysulfide adsorption test for varying carbon materials and corresponding surface area and pore volume from N_2 physisorption measurements.

As an example of adsorption behavior for different polysulfides, a qualititive adsorption test was performed in the lab. The resulting polysulfide solution after 24hr exposure to various carbon materials is shown in Figure 4.5. The mesoporous carbon nanofiber (MPCNF) was synthesized using a polymer electrospinning method with subsequent heat treatments.[40] The Ketjen Black sample shows the best adsorption due to its high surface area and pore volume. Interestingly, despite their similar surface area the two MPCNF samples showed different adsorption properties. This suggests that pore volume is more important than raw surface area for polysulfide adorption in carbon hosts.

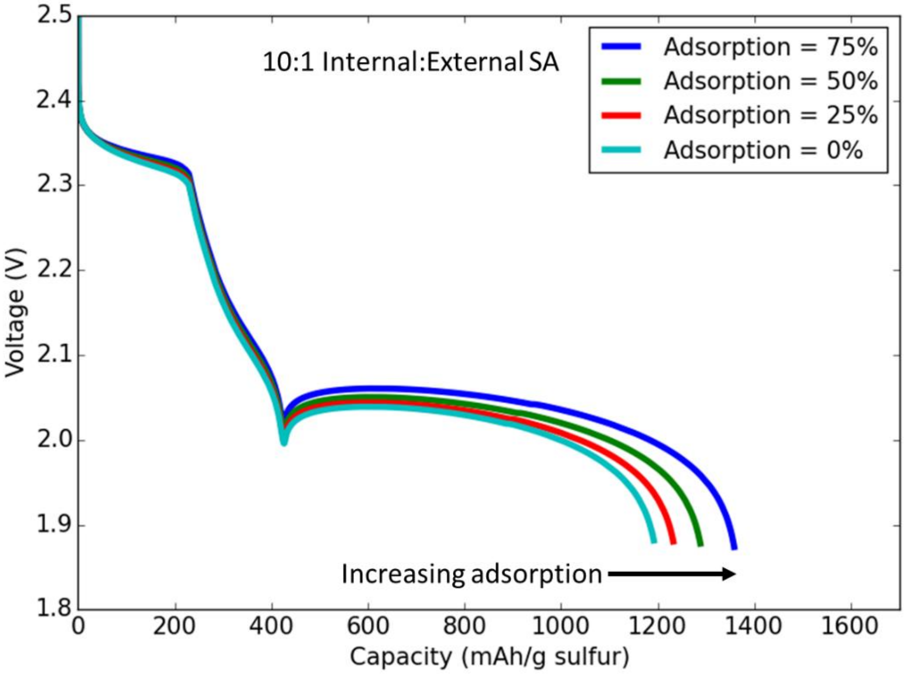

Figure 4.6 Simulated discharge curves for the passivation limited model + time independent adsorption model for different adsorption percents at 0.1C.

Using a time independent adsorption model, the effect of adsorption when combined with inner-outer geometry can be seen in Figure 4.6. When 75% of the total concentration of polysulfides in the inner region are considered to be adsorbed and trapped, superior capacity is achieved. By trapping the polysulfides in the high surface area interior, the particle will not become blocked by the external region passivatino and the cathode can be most efficiently utilized.

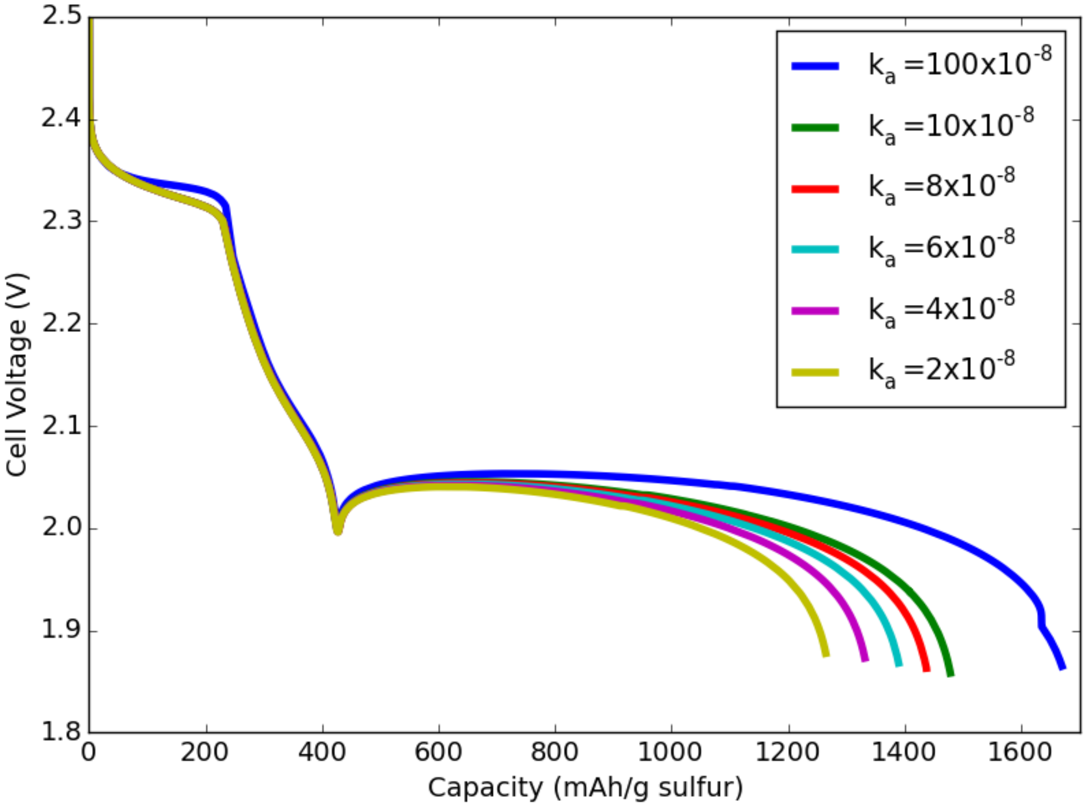

Figure 4.7 Simulated discharge curves for the passivation limited model + time dependent adsorption model for adsorption rate constants at 0.1C.

When the Langmuir time dependent adsorption model is used, the behavior depends partly on the adsorption and desorption rate constants k_a and k_d. k_a is varied in Figure 4.7, and it is observed that faster adsorption can improve discharge capacity due to better retention of polysulfides in the high surface area and high adsorption capacity inner region.

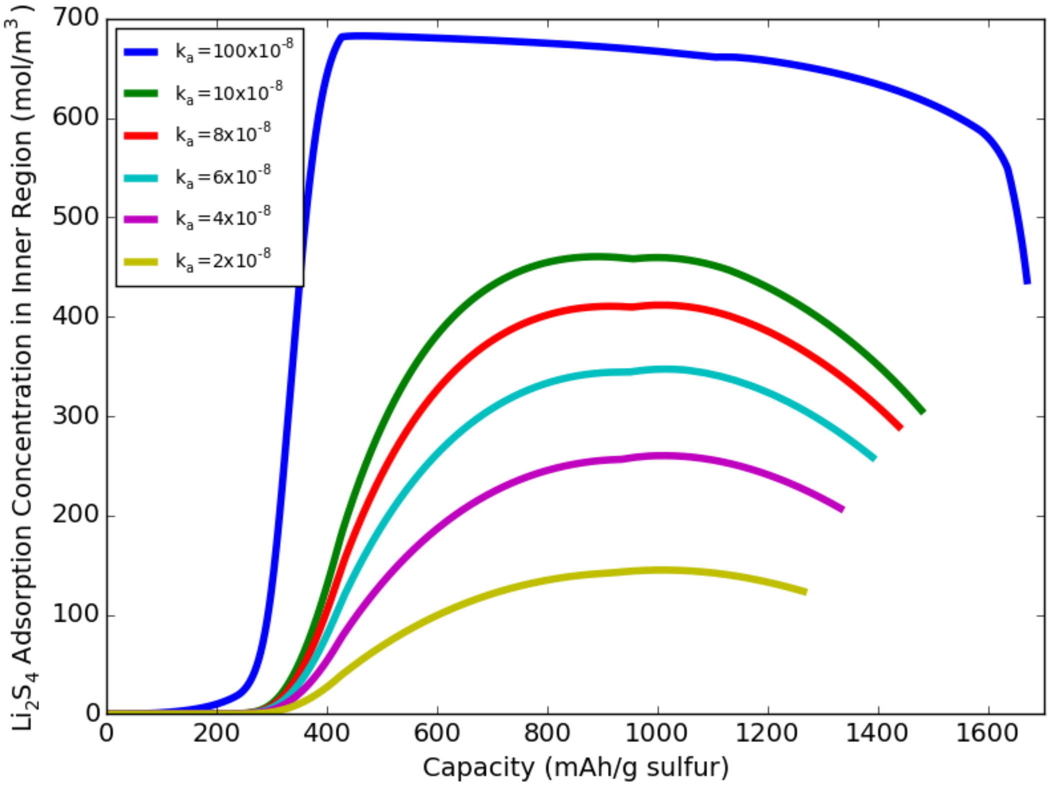

Figure 4.8 Li_2S_4 concentration in the internal region for varying values of the adsorption rate constant at 0.1C.

The time dependent Li_2S_4 adsorption behavior can be seen in Figure 4.8 for the same simulations as in Figure 4.7. For the fastest adsorption rate, the maximum amount of polysulfide is adsorbed very quickly. For slower adsorption rates, there is not enough time for full adsorption to occur, allowing some Li_2S_4 to diffuse out of the inner region. This results in more Li_2S_2 deposition in the outer region later in discharge, reducing capacity.

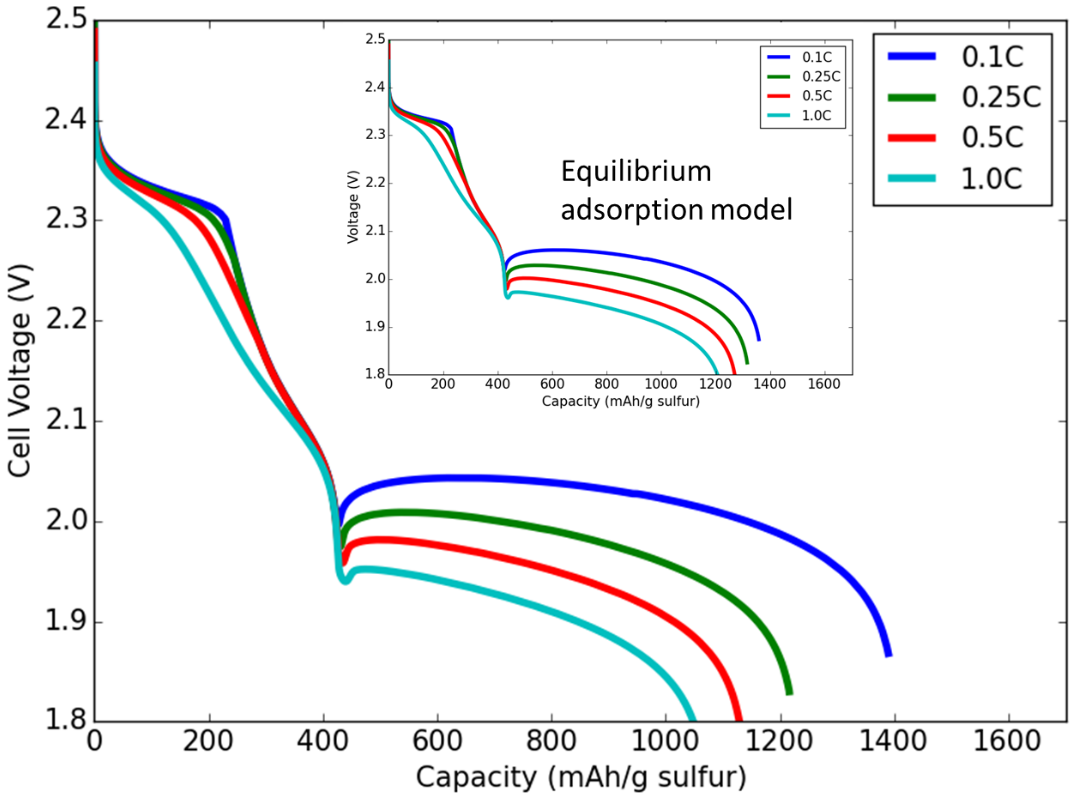

Figure 4.9 Time dependent adsorption model discharge curves for varying C-rates. k_a = $6 \cdot 10^8$ m^3 s^{-1}. The insert shows results for the time-independent adsorption model.

In Figure 4.9, the C-rate is varied for the time dependent adsorption model. Compared to the time-independent adsorption model in the insert, the time-dependent adsorption model shows worsened behavior at higher C-rates. Essentially, the time independent model overestimates the benefits from adsorption by ignoring that the higher C-rates have a shorter discharge time scale and thus less time for adsorption to occur. The time dependent model is more realistic than ignoring adsorption or using the time independent mode, but further improvement could be made if accurate parameters are found from experimental adsorption testing.

4.4.3 End-of-discharge failure mechanism for Li-S batteries

To examine Li-S battery behavior at the end of discharge, multi C-rate tests were performed with different cathodes. The cathodes were prepared with the same materials and loading but with either a slurry cast processing method or an electrospray processing method. These processes result in a different cathode morphology, including porosity, macropore size, thickness, particle size, and surface cracking. In addition, some cathodes were post-treated with a layer of graphene on the surface facing the separator and anode. Figure 4.10 shows the multi C-rate discharge results for the graphene coated and bare electrosprayed cathodes.

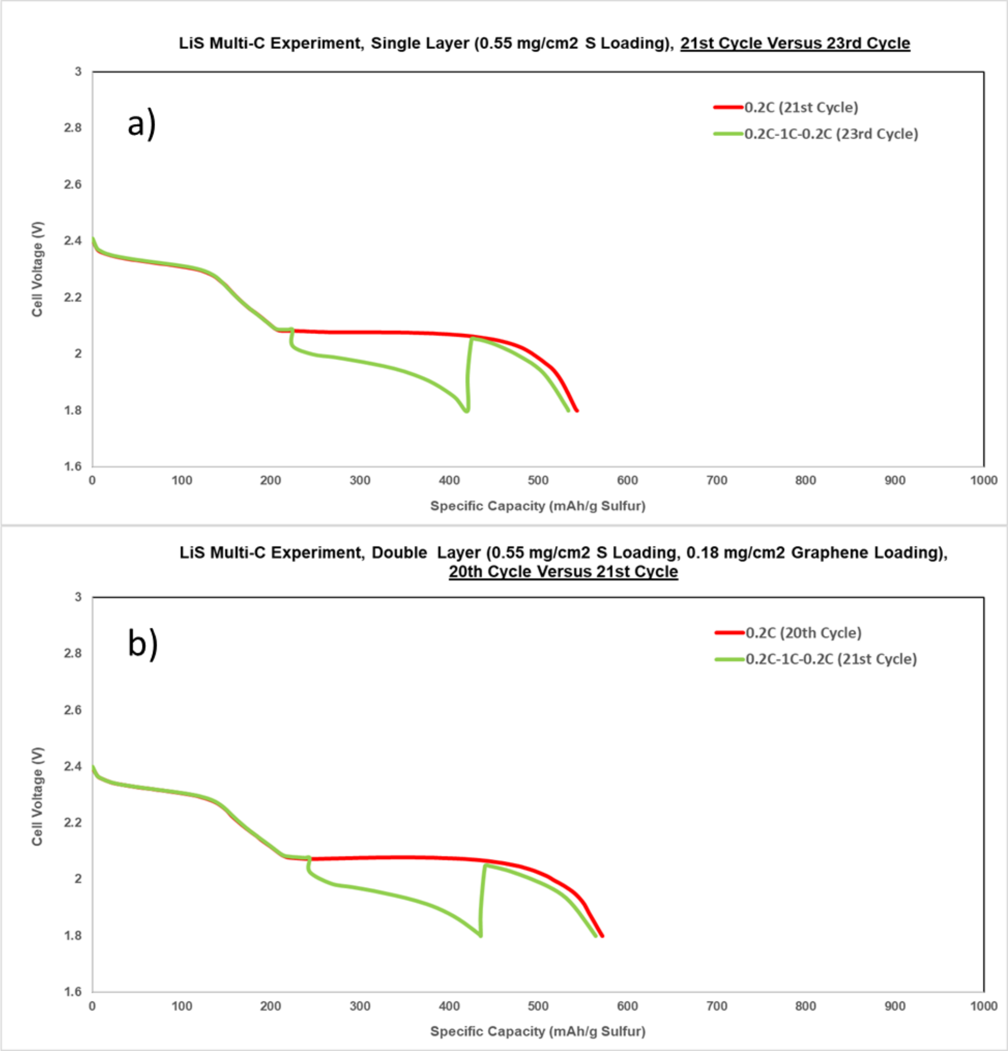

Figure 4.10 Multi C-rate results for electrosprayed carbon cathodes with a) no graphene coating and b) graphene coating. Experiments performed by Caspar Yi.

Both the graphene coated and uncoated electrosprayed cathodes show full recovery in capacity after the 1.0C intermediate section. This demonstrates that the failure at the end of the 1.0C discharge was not due to complete passivation of the cathode. If it was, the battery would not be able to continue discharging normally after the 1.0C region. In addition, it shows that the 1.0C region did not affect the nucleation structure of the lithium sulfide deposits. Previous investigations have shown that the size of lithum sulfide nuclei in experiment depends on the discharge rate, which was implemented into the passivation limited simulation.[27] However, if this was the case, its effect was not significant enough to impact the performance of these cells: the total capacity including the 1.0C region was the same as without any 1.0C portion. This suggests that the faster discharge during 1.0C did not alter the nucleation structure enough to reduce the capacity in the final 0.2C segment. The experimental results suggest that instead the 1.0C failure was caused by mass transport limitations, as is discussed in more detail in Chapter 5. The graphene layer also did not affect the failure condition, with both coated and uncoated cathodes showing similar discharge curves and multi C-rate behavior.

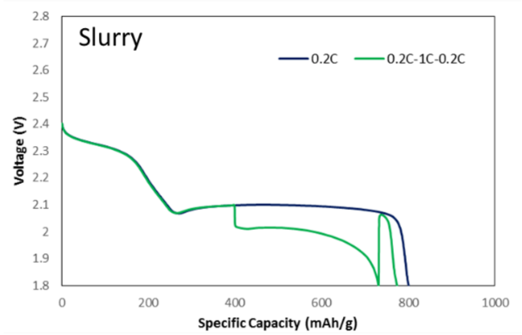

Figure 4.11 Multi C-rate test for slurry cast Li-S coin cells.

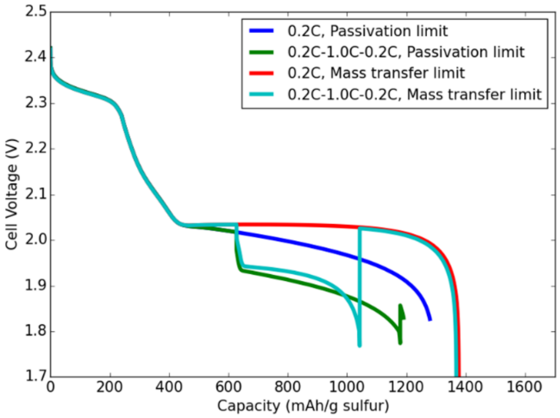

Figure 4.12 Comparison of mass transport limited and passivation limited models.

In Figure 4.11, the same multi C-rate test for slurry cast cathodes results in less than full capacity for the 0.2C-1.0C-0.2C test, implying passivation failure. This shows that both failure conditions can be seen in experiment depending on the cathode properties. For comparison, the two simulated failure condition mechanisms are plotted side by side in Figure 4.12 with the same multi C-rate discharge behavior. The passivation limited model is not able to achieve capacity after the 1.0C failure due to the near complete coverage of the cathode with lithium sulfide. However, the mass transport limited model introduced in Chapter 5 is able to replicate the behavior observed in experiment. This provides further evidence to support that both failure mechanisms are present in Li-S batteries, and must be taken in to account when designing new materials.

4.5 Conclusions

Expanding upon literature Li-S nucleation and passivation models, an inner-outer two region cathode is developed and used to investigate passivation of Li-S cathodes. It is found that if polysulfides are free to leave the cathode, lithium sulfide deposits will coat the outside of the cathode particles and limit the utilization of the inner cathode regions. The model was then expanded to include adsorption of polysulfides using a simplistic time-independent model and a time-dependent kinetic model. The addition of adsorption allows a more accurate treatment of carbon materials that improve performance by containing polysulfides within the cathode. In a response to discussion in literature over the end-of-discharge failure mechanism, two processing techniques were used to produce cathodes that were tested using a multi C-rate test. Surprisingly, the failure mechanism was dependent on whether electrospray and slurry cast processing was used. The effect of the mass transport and passivation mechanisms was then illustrated through simulations under the same multi C-rate conditions. It is suspected that the different porosity of the cathodes is responsible for the occurrence of different failure mechanisms. The more porous electrosprayed cathode has greater area and volume available for lithium sulfide deposition, mitigating the passivation failure. However, its porosity also allows polysulfides to escape easily which promotes the mass transport failure. For the less porous slurry cast cathode, smaller sized pores likely promote better adsorption and retain polysulfides in the cathode. However, it suffers from passivation due to its more limitd volume and surface area. These results suggest that either or both of the competing models of Li-S failure might occur in a battery depending on the material properties.

4.6 Supplemental information

4.6.1 Simulated diffusion through clogged nanopores

To investigate how different nuclei structures could affect the diffusion of polysulfides in the Li-S battery cathode, a simplified molecular dynamics (MD) simulation was designed. In the simulation, a static structure of hemispheres representing lithium sulfide nuclei that consist of MD beads is created inside of a cylindrical structure representing a carbon nanopore. The cylindrical structure is open at one end and closed on the other end. Before the simulation begins, the nuclei centerpoints are placed at random on the inner walls of the pore, and then lithium sulfide beads with 0.25nm spacing are added to create the hemispheres. Additional nuclei are added continously until the porosity is equal to 0.5, and they are allowed to overlap. All the nuclei within the pore have the same radius, although its is possible to have a distribution of radii as well.

The radius of the cylindrical pore is set to 5nm, a typical value for mesoporous carbon, and its length is chosen as 100nm. The cylindrical pore is made of up of 1 layer of MD beads with spacing of 1 nm. Lastly, diffisive beads each representing a single polysulfide are created outside of the mouth of the pore.

Diffusive polysulfide beads and hemisphere beads with each other with the Weeks-Chandler-Anderson (WCA) potential,[41]

$$u(r) = 4\varepsilon\left[\left(\frac{\sigma}{r}\right)^{12} - \left(\frac{\sigma}{r}\right)^{6}\right] + \varepsilon, \qquad r \leq 2^{\frac{1}{6}}$$

$$u(r) = 0, \quad r > 2^{\frac{1}{6}}$$

where r is the distance between two beads and $\boldsymbol{\varepsilon}$ and σ are Lennard-Jones parameters. The cutoff distance of $2^{\frac{1}{6}}$ nm eliminates the attractive portion of the function, resulting in a purely repulsive potential. For polysulfide interaction with the wall, the same potential is used but with a 2.5nm cutoff, which results in an attractive potential. Values for parameters used in the simulation are given in Table 4.5.

Table 4.5 Parameters for MD diffusion simulation.

Parameter	**Value**	**Units**
Pore length	100	Nm
Pore radius	5	Nm
Porosity	0.5	-
Wall bead spacing	1	Nm
Hemisphere bead spacing	0.25	Nm

Temperature	300	K
Lennard-Jones ε	1	Kcal mol^{-1}
Lennard-Jones σ	1	Nm
Polymer aspect ratio	10	10
Timestep	0.005	femtosecond
Number of timesteps	300000	-

At the start of the simulation, polysulfide beads will begin to move randomly. As they travel through the pore, they must navigate the internal structure created by the hemispherical lithium sulfide deposits. This is visualized in Figure 4.13.

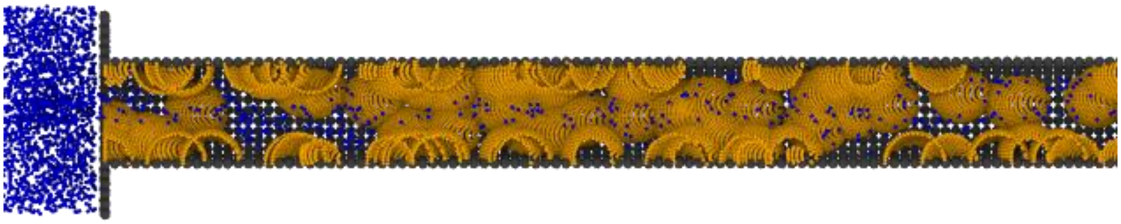

Figure 4.13 Visualization of the axial cross section of the Li-S diffusion simulation. Blue beads are polysulfide, yellow beads are lithium sulfide deposits, and grey beads are the carbon pore walls.

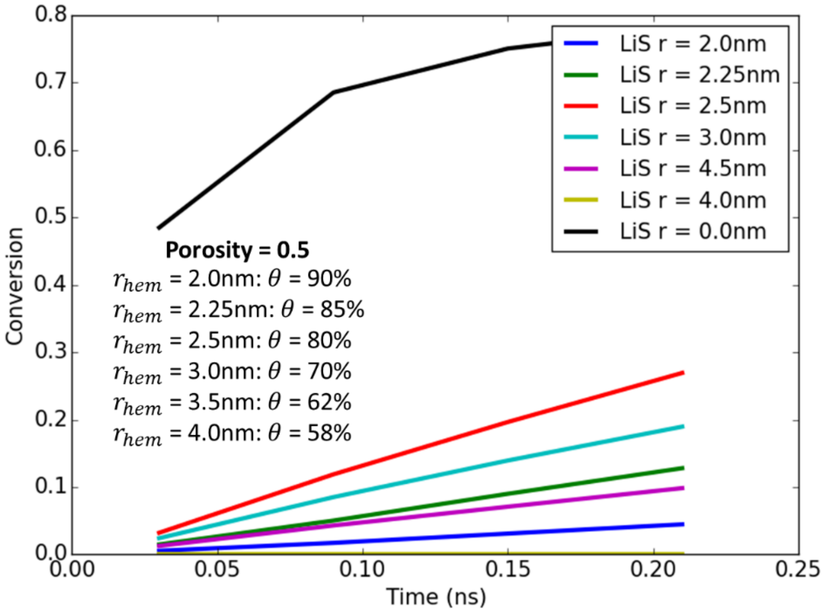

Figure 4.14 Simulated conversion of diffusion polysulfide species at the walls of a lithium sulfide-clogged pore plotted against time. r_{hem} is the radius of the lithium sulfide hemisphere and θ is the surface coverage of lithium sulfide in the pore.

When the polysulfide beads reach a wall of the pore, they react and are removed from the simulation. The amount of reacted beads over time as recorded and expressed as conversion, the fraction of polysulfides that have reacted. The results are plotted in Figure 4.14 for a variety of hemisphere radii. In these plots, the slope of the line is roughly proportional to the diffusion coefficient. For r_{hem} = 0, which represents an open pore with no lithium sulfide hemispheres, the conversion is fastest as there are no obstructions for polysulfides to reach the walls and react. At a r_{hem} of 2nm, conversion is very slow due to the high θ of 90%, which requires polysulfides to diffuse far to reach an available reaction site. From r_{hem} = 2.5nm to r_{hem} = 3.0nm, however, the conversion rate begins to decline despite the decreasing surface coverage. This is because instead of the passivation of the carbon walls limiting the reaction, as is the case for the smaller r_{hem}, the larger r_{hem} approach the length scale of the pore radius and begin to clog the pore physically. This mass transfer limited effect is most exagerated for r_{hem} = 4.0nm, for which the pore is fully clogged allowing no polysulfide conversion. These results suggest that for constant porosity, surface coverage and pore bloackage trade off as lithium sulfide deposit size varies. When deposits form a thin film with high θ, passivation is responsible for slow reaction. When deposits form a few large deposits with sizes approaching that of the pore, they can block the movement of molecules in and out of the pore, limiting reaction as well. Therefore, pores size in carbon cathodes should be controlled so that they are small enough to maintain high surface area but still larger than the typical lithium sulfide desposit radius, which varies based on the battery properties and the discharge rate.

4.7 References

1. Hannan, M. A., Hoque, M. M., Mohamed, A. & Ayob, A. Review of energy storage systems for electric vehicle applications: Issues and challenges. *Renew. Sustain. Energy Rev.* **69**, 771–789 (2017).
2. Lee, J. T., Zhao, Y., Kim, H., Cho, W. Il & Yushin, G. Sulfur infiltrated activated carbon cathodes for lithium sulfur cells: The combined effects of pore size distribution and electrolyte molarity. *J. Power Sources* **248**, 752–761 (2014).
3. Wang, W. H. & Wang, X. D. Investigation of Ir-modified carbon felt as the positive electrode of an all-vanadium redox flow battery. *Electrochim. Acta* **52**, 6755–6762 (2007).
4. Fei, L. *et al.* Graphene Folding in Si Rich Carbon Nanofibers for Highly Stable, High Capacity Li-Ion Battery Anodes. *ACS Appl. Mater. Interfaces* **8**, 5243–5250 (2016).
5. Yin, Y. X., Xin, S., Wan, L. J., Li, C. J. & Guo, Y. G. Electrospray synthesis of silicon/carbon nanoporous microspheres as improved anode materials for lithium-ion batteries. *J. Phys. Chem. C* **115**, 14148–14154 (2011).
6. Manthiram, A., Fu, Y., Chung, S.-H., Zu, C. & Su, Y.-S. Rechargeable Lithium–Sulfur Batteries. *Chem. Rev.* **114**, 11751–11787 (2014).
7. Liu, J. *et al.* Minimizing Polysulfide Shuttle Effect in Lithium-Ion Sulfur Batteries by Anode Surface Passivation. *ACS Appl. Mater. Interfaces* **10**, 21965–21972 (2018).

8. Wang, Q. *et al.* A shuttle effect free lithium sulfur battery based on a hybrid electrolyte. *Phys. Chem. Chem. Phys.* **16**, 21225–21229 (2014).

9. Liu, M. *et al.* Suppressing Self-Discharge and Shuttle Effect of Lithium-Sulfur Batteries with V 2 O 5 -Decorated Carbon Nanofiber Interlayer. *Small* **13**, 1602539 (2017).

10. Hofmann, A. F., Fronczek, D. N. & Bessler, W. G. Mechanistic modeling of polysulfide shuttle and capacity loss in lithium-sulfur batteries. *J. Power Sources* **259**, 300–310 (2014).

11. Mikhaylik, Y. V & Akridge, J. R. Polysulfide Shuttle Study in the Li/S Battery System. *J. Electrochem. Soc.* **151**, A1969 (2004).

12. Liu, S. *et al.* Hollow carbon spheres with nanoporous shells and tailored chemical interfaces as sulfur host for long cycle life of lithium sulfur batteries. *Electrochim. Acta* **279**, 10–18 (2018).

13. Gueon, D. *et al.* Spherical Macroporous Carbon Nanotube Particles with Ultrahigh Sulfur Loading for Lithium-Sulfur Battery Cathodes. *ACS Nano* **12**, 226–233 (2018).

14. Lu, D. *et al.* Enabling High-Energy-Density Cathode for Lithium-Sulfur Batteries. *ACS Appl. Mater. Interfaces* **10**, 23094–23102 (2018).

15. He, X. *et al.* Expansion and shrinkage of the sulfur composite electrode in rechargeable lithium batteries. *J. Power Sources* **190**, 154–156 (2009).

16. Zhang, K., Zhao, Q., Tao, Z. & Chen, J. Composite of sulfur impregnated in porous hollow carbon spheres as the cathode of Li-S batteries with high performance. *Nano Res.* **6**, 38–46 (2013).

17. Li, X. *et al.* Optimization of mesoporous carbon structures for lithium-sulfur battery applications. *J. Mater. Chem.* **21**, 16603–16610 (2011).

18. Zhang, X. Q., He, B., Li, W. C. & Lu, A. H. Hollow carbon nanofibers with dynamic adjustable pore sizes and closed ends as hosts for high-rate lithium-sulfur battery cathodes. *Nano Res.* **11**, 1238–1246 (2018).

19. Pei, F. *et al.* From Hollow Carbon Spheres to N-Doped Hollow Porous Carbon Bowls: Rational Design of Hollow Carbon Host for Li-S Batteries. *Adv. Energy Mater*. **6**, 1–8 (2016).

20. Wu, D. S. *et al.* Quantitative investigation of polysulfide adsorption capability of candidate materials for Li-S batteries. *Energy Storage Mater.* **13**, 241–246 (2018).

21. Liu, J. *et al.* SnO2 as a high-efficiency polysulfide trap in lithium-sulfur batteries. *Nanoscale* **8**, 13638–13645 (2016).

22. Yuan, Z. *et al.* Powering Lithium-Sulfur Battery Performance by Propelling Polysulfide Redox at Sulfiphilic Hosts. *Nano Lett.* **16**, 519–527 (2016).

23. Ma, Z. *et al.* The enhancement of polysulfide absorbsion in Li-S batteries by hierarchically porous CoS2/carbon paper interlayer. *J. Power Sources* **325**, 71–78 (2016).

24. Kumaresan, K., Mikhaylik, Y. & White, R. E. A Mathematical Model for a Lithium–Sulfur Cell. *J. Electrochem. Soc.* **155**, A576 (2008).

25. Marinescu, M., Zhang, T. & Offer, G. J. A zero dimensional model of lithium-sulfur batteries during charge and discharge. *Phys. Chem. Chem. Phys.* **18**, 584–593 (2016).

26. Andrei, P., Shen, C. & Zheng, J. P. Theoretical and experimental analysis of precipitation and solubility effects in lithium-sulfur batteries. *Electrochim. Acta* **284**, 469–484 (2018).

27. Ren, Y. X., Zhao, T. S., Liu, M., Tan, P. & Zeng, Y. K. Modeling of lithium-sulfur batteries incorporating the effect of Li 2 S precipitation. *J. Power Sources* **336**, 115–125 (2016).

28. Lau, S. & Archer, L. A. Nucleation and Growth of Lithium Peroxide in the Li-O2 Battery. *Nano Lett.* **15**, 5995–6002 (2015).

29. Zhang, T., Marinescu, M., Walus, S., Kovacik, P. & Offer, G. J. What Limits the Rate Capability of Li-S Batteries during Discharge: Charge Transfer or Mass Transfer? *J. Electrochem. Soc.* **165**, A6001–A6004 (2018).

30. Pan, H. *et al.* On the Way Toward Understanding Solution Chemistry of Lithium Polysulfides for High Energy Li-S Redox Flow Batteries. *Adv. Energy Mater.* **5**, 1–7 (2015).

31. Danner, T., Zhu, G., Hofmann, A. F. & Latz, A. Modeling of nano-structured cathodes for improved lithium-sulfur batteries. *Electrochim. Acta* **184**, 124–133 (2015).

32. Bazant, M. Z. Theory of chemical kinetics and charge transfer based on nonequilibrium thermodynamics. *Acc. Chem. Res.* **46**, 1144–1160 (2013).

33. Thangavel, V. *et al.* A Microstructurally Resolved Model for Li-S Batteries Assessing the Impact of the Cathode Design on the Discharge Performance. *J. Electrochem. Soc.* **163**, A2817–A2829 (2016).

34. Tjaden, B., Cooper, S. J., Brett, D. J., Kramer, D. & Shearing, P. R. On the

origin and application of the Bruggeman correlation for analysing transport phenomena in electrochemical systems. *Current Opinion in Chemical Engineering* **12**, 44–51 (2016).

35. Lu, Y. C., He, Q. & Gasteiger, H. A. Probing the lithium-sulfur redox reactions: A rotating-ring disk electrode study. *J. Phys. Chem. C* **118**, 5733–5741 (2014).

36. Valøen, L. O. & Reimers, J. N. Transport Properties of LiPF6-Based Li-Ion Battery Electrolytes. *J. Electrochem. Soc.* **152**, A882 (2005).

37. Song, J. *et al.* Strong lithium polysulfide chemisorption on electroactive sites of nitrogen-doped carbon composites for high-performance lithium-sulfur battery cathodes. *Angew. Chemie - Int. Ed.* **54**, 4325–4329 (2015).

38. Halim, W. *et al.* Directly deposited binder-free sulfur electrode enabled by air-controlled electrospray process. *ACS Appl. Energy Mater.* **2**, 678–686 (2019).

39. Lee, J. H. *et al.* Effective Suppression of the Polysulfide Shuttle Effect in Lithium-Sulfur Batteries by Implementing rGO-PEDOT:PSS-Coated Separators via Air-Controlled Electrospray. *ACS Omega* **3**, 16465–16471 (2018).

40. Williams, B. P. & Joo, Y. L. Tunable Large Mesopores in Carbon Nanofiber Interlayers for High-Rate Lithium Sulfur Batteries. *J. Electrochem. Soc.* **163**, A2745–A2756 (2016).

41. Weeks, J., Chandler, D. & Andersen, H. C. Role of Repulsive Force in Determining the Equilibrium Structure of Simple Liquids. *J. Chem. Phys.* **54**, 5237 (1971).

CHAPTER 5

END-OF-DISCHARGE FAILURE AND RECOVERY OF LI-S BATTERIES WITH LIQUID AND GEL ELECTROLYTE: MODELING AND EXPERIMENTS

The effect of gel electrolyte on lithium-sulfur (Li-S) battery behavior near the end of discharge is investigated using both experimental and simulation methods. To probe the end of discharge, a modified discharge procedure was used where the cell is first paused after discharge and then discharged a second time before recharging normally. Coin cell tests for two gel electrolytes in addition to liquid electrolyte show up to 7% capacity recovered after the pause, which indicates that diffusion of species during the pause is responsible for the failure recovery. Additionally, recovery is higher for gel electrolytes compared to liquid, for higher C-rates, and for longer pause times. To understand this behavior, a Li-S numerical model with mass transport limited reactions was used to examine different polysulfide diffusion coefficients expected in different electrolyte systems. The model is able to reproduce the trends seen in experiment and yields higher recovery for smaller Li_2S_4 diffusion coefficients, suggesting that insufficient Li_2S_4 mass transport is responsible for failure at end of discharge.

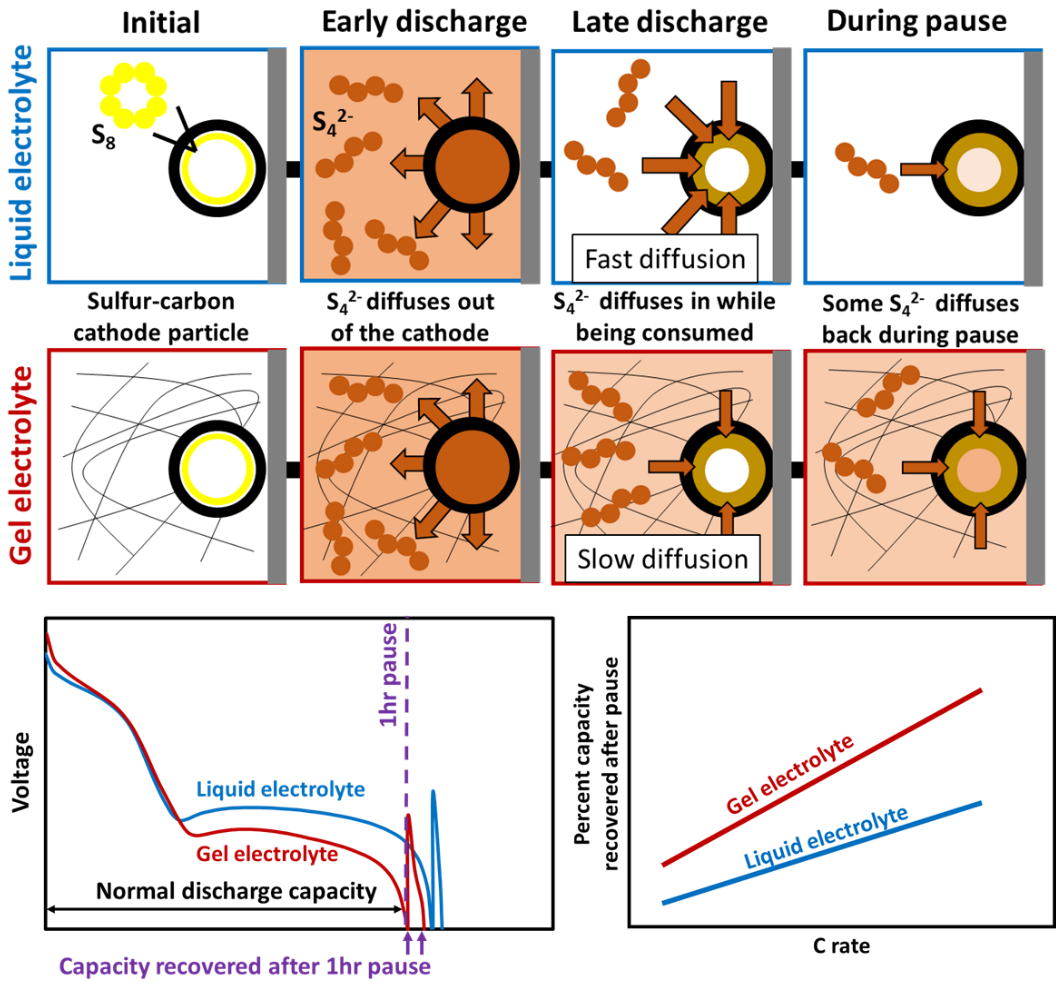

Abstract Figure Summary of key results from numerical simulation and experiments of end-of-discharge Li-S failure behavior.

5.1 Introduction

As interest in renewable energy grows and demand for electric vehicles strengthens, it is crucial for energy storage technology to improve beyond the currently used lithium-ion (Li-ion) batteries.[1] Lithium-sulfur batteries (Li-S) are one of the most promising battery candidates to replace Li-ion batteries due to their high theoretical specific energy of 2510 W H kg^{-1}.[2] In addition, the low cost and plentiful supply of sulfur preferred to the expensive and relatively scarce cobalt frequently used in Li-ion battery cathodes. However, Li-S batteries still suffer from a number of challenges that limit their viability. First, intermediate lithium polysulfide species formed during the electrochemical conversion of sulfur have high solubility in the battery electrolyte, allowing movement away from reaction sites in the cathode and leading to side reactions at the anode.[3–7] Second, lithium sulfide discharge products are insulating, requiring the use of conductive carbon host materials and limiting the sulfur loading and energy density of the battery.[8–10] The sulfur to lithium sulfide conversion during discharge also involves a 79% volume expansion which can damage the cathode structure over many cycles.[11,12] Li-S research has focused in large part in developing strategies that reduce or eliminate these challenges.

To limit the movement of polysulfide out of the cathode, many researchers have developed carbon or other materials that can trap or adsorb the polysulfides. These materials have shown improved cycle performance and capacity, but can add significant costs due to complex material synthesis and sulfur impregnation processes.[13,14] Another approach is to use gel polymer electrolyte (GPE) or gelled liquid electrolyte instead of the traditional liquid electrolyte (LE), which has already proven successful in Li-ion battery research.[15–17] By trapping solvent molecules in a polymerized or crosslinked gel network, the transport and solubility of polysulfides can be suppressed. Gel electrolyte also reduces flammability and suppresses the formation of dendrites on the lithium metal surface that can puncture the battery separator, which are crucial safety concerns.[18] Previous work has shown promising results in the application of gel electrolyte to Li-S systems. Natarajan used a polyethylene oxide GPE with plasticizer additives to improve the gel’s ionic conductivity and showed preliminary Li-S results.[19] Chen et al. used a polyethylene oxide GPE which enabled lower electrolyte to sulfur ratios, and they identified passivation of the cathode as the failure mechanism.[20] Liu et al. used a pentaerythritol tetraacrylate GPE which limited polysulfide diffusion, improved interfacial contact, and showed better rate capability than liquid electrolytes.[21]

While gel electrolytes have been shown to limit polysulfide diffusion, the complexity of the Li-S system makes fundamental understanding difficult with experimental methods alone. Li-S numerical simulations have aided Li-S research by demonstrating good experimental agreement and proposing mechanisms for behavior observed in experiment without the need for complex characterization methods. Kumaresan et al. first proposed a 1-dimensional + time Li-S simulation which showed that the Li-S discharge curve could be accurately represented by a series of five sulfur reactions in combination with dissolution and precipitation effects.[22] More recently, simulations have attempted to address the mechanism of cell failure at the end of discharge. Ren et al. proposed a nucleation and passivation mechanism where insulating lithium sulfide precipitates onto the carbon cathode during discharge and eventually covers all of the surface area, resulting in no further ability perform electrochemical reactions.[23] This has been disputed by Zhang et al., whose experiments and simulations support a mass transport limited mechanism.[24]

For the case of gel electrolytes, no simulations have yet attempted to model the Li-S battery performance. As gel electrolytes further restrict the movement of lithium ions and polysulfides, mass transport limitations that limit discharge capacity may become even more pronounced. In this paper, we use a combination of simulations and experiments in order to investigate the effect of electrolyte choice on fundamental Li-S behavior. We first compare experimental results for liquid electrolyte and gelled liquid electrolyte systems. To probe the end of discharge behavior, we use a specialized discharge method where the cell discharges until 1.8V, pauses for a chosen amount of time, and then attempts to continue discharge. By examining the capacity recovered after the pause, the reason for the cell's original failure at discharge can be elucidated. We then use numerical simulation with the same pause discharge procedure to explain and gain further insight into the experimental results. In our simulations, we specifically focus on the effect of slower polysulfide diffusion caused by the gelled electrolyte by directly varying the Li_2S_4 diffusion coefficient. Understanding the end-of-discharge behavior for gel and liquid electrolyte systems is crucial in the effort to improve battery capacity through rational cathode and electrolyte design.

5.2 Theoretical model

5.2.1 Electrochemical and precipitation reactions

During discharge, elemental sulfur (S_8) is converted into successive lithium polysulfides (Li_2S_x) until finally forming lithium sulfide (Li_2S) The full diversity of lithium polysulfides that may exist in the battery is not fully understood; however, it has been shown by previous models that the characteristic discharge behavior can be captured with a limited subset of electrochemical reactions.[22] In our model, we use four polysulfide electrochemical reactions and consider the dissolution of S_8 and the precipitation of Li_2S as separate reactions. The remaining polysulfide species are assumed have negligible precipitation, which is supported by experimental work.[25] The electrochemical and precipitation reactions occurring at the cathode are listed below:

$$\mathrm{S}_8^{(\mathrm{s})} \rightleftharpoons \mathrm{S}_8^{(\mathrm{l})}$$

$$\mathrm{S}_8^{(\mathrm{l})} + \mathrm{e}^- \rightleftharpoons \mathrm{S}_8^{2-}$$

$$\frac{3}{2}\mathrm{S}_8^{2-} + \mathrm{e}^- \rightleftharpoons 2\mathrm{S}_6^{2-}$$

$$\mathrm{S}_6^{2-} + \mathrm{e}^- \rightleftharpoons \frac{3}{2}\mathrm{S}_4^{2-}$$

$$\frac{1}{3}\mathrm{S}_4^{2-} + \mathrm{e}^- \rightleftharpoons \frac{4}{3}\mathrm{S}^{2-}$$

$$\mathrm{S}^{2-} + 2\mathrm{Li}^+ \rightleftharpoons \mathrm{Li}_2\mathrm{S}^{(\mathrm{s})}$$

The first two reaction occur at the beginning of discharge in the first plateau region of the typical Li-S discharge curve. The third and fourth reactions then occur in the downward sloping region after the first plateau once the elemental sulfur is consumed, and the fifth and sixth reactions occur during the second plateau region once the longer chain polysulfides are consumed.

At the anode, lithium ions are produced at a rate determined by the applied current *I* with the following reaction:

$$\mathrm{Li_s} \rightleftharpoons \mathrm{Li^+} + \mathrm{e^-}$$

The lithium salt anion is denoted as A^-, which is bis(trifluoromethanesulfonyl)imide in our electrolytes. As solid species are dissolved or precipitated, their volume fractions ε_i change with time *t* according to Equation 1:

$$\frac{\partial \varepsilon_i}{\partial t} = \frac{M_i}{\rho_i} \sum_m a_s v_{i,m} r_m \quad (1)$$

where M_i is molecular weight of solid species i, ρ_i is the density, a_s is the specific surface area, $v_{i,m}$ is the stoichiometric coefficient for species *i* in reaction m, r_m is the reaction rate of reaction m for the two precipitation reactions (reactions 1 and 6 in Table 5.1). We use subscript *i* to denote species and subscript *m* to denote reactions Values of density and molecular weight are listed in Table 5.1, and stoichiometric coefficients are taken from the coefficients in the reactions with reactant side values being negative. Values of surface area and other structural parameters can be found in Table 5.2. The volume fraction of electrolyte, ε, is calculated directly from volume fraction of all precipitated species plus the volume fraction of carbon subtracted from 1, seen in Equation 2:

$$\varepsilon = 1 - \varepsilon_c - \sum \varepsilon_i \qquad (2)$$

where ε_c is the volume fraction of solid carbon or separator in the cell. Reaction rates for each electrochemical cathode reaction (reactions 2-5) are defined by a modified mass transport limited Butler-Volmer equation in Equation 3:

$$r_m = k_m \left(a_{re} a_{prod}\right)^{0.5} \left(\left(1 - \frac{r_m}{r_{l,c}}\right) e^{-\frac{1}{2RT}\Delta\mu_m} - \left(1 - \frac{r_m}{r_{l,a}}\right) e^{\frac{1}{2RT}\Delta\mu_m}\right) \qquad (3)$$

where k_m is a reaction constant, $r_{l,c}$ is a limiting reactino rate, R is the gas constant, T is temperature, and $\Delta\mu_m$ is the change in chemical potential for reaction *m*. It should be noted that r_m is scaled by the cathode surface area with units of mol m^{-2}s^{-1}. a_{re} and a_{prod} represent the activities of reactants and products respectively, as used in Danner et. al.[26] Symmetry and activity coefficients were assumed to be 0.5 and 1 respectively. The $(1 - \frac{r_m}{r_{l,c}})$ term represents a mass transport limitation which reduces the reaction rate as the reaction rates approach some limit.[27] This limit represents the maximum rate at which reactants can be supplied to reaction sites in the cathode. Above this rate it is not possible for the cell meet the demanded external current. Excluding the mass transport limitation, this form of the Butler-Volmer equation was taken from Bazant.[26,28] The limiting reaction rate is given by Equation 4:

$$r_{l,c} = a_{mtl}\left(c_{Li^+}(c_{S_4^{2-}} + c_{S_6^{2-}})\right)(1 - \frac{\varepsilon_{Li_2S}}{\varepsilon_{max}})^{b_{mtl}} \qquad (4)$$

where a_{mtl} and b_{mtl} are fitting parameters chosen to match experimental data and c_i is concentration. The limiting reaction rate for the reverse reaction $r_{l,a}$is assumed to be the same as $r_{l,c}$. This term assumes that the maximum mass transport rate to reaction sites will decrease as the cathode is clogged with solid deposits and as the concentrations of reactants decreases in the bulk. The form of this limitation is similar to that used previously by Zhang et al.[24]

For electrochemical reaction, the change in chemical potential and equilibrium voltage is given in Equations 5 and 6 [26,28]:

$$\Delta\mu_m = n_m F(\phi_{cathode} - U_{eq,m}) \qquad (5)$$

$$U_{eq,m} = U_{eq0,m} + RTln(\frac{a_{re}}{a_{prod}}) \qquad (6)$$

where n_m is the number of electrons per reaction, F is the Faraday constant, $\phi_{cathode}$

is the voltage of the carbon cathode, $U_{eq,m}$ is the open circuit potential for reaction *m*, and $U_{eq0,m}$is the open circuit potential at reference conditions. Sulfur (S_8) and lithium sulfide (Li_2S) undergo precipitation/dissolution reactions with $\Delta\mu_m$ given by Equation 7 instead:

$$\Delta\mu_m = RTln(K_{sp,m}\frac{a_{prod}}{a_{re}}) \qquad (7)$$

where $K_{sp,m}$ is the solubility product for precipitation reaction *m*. Parameters used in reactions are listed in Table 5.1.

Table 5.1 Reaction parameters k_m (reaction rate constant), n_m (electrons per reaction), $U_{eq0,m}$ (open circuit voltage at reference conditions), and $K_{sp,m}$ (solubility product). [a]Assumed parameters.

Reaction	**Index *m***	$\boldsymbol{k_m}$ **(mol m^{-2} s^{-1})**	$\boldsymbol{n_m}$	$\boldsymbol{U_{eq0,m}}$ **(V)**	$\boldsymbol{K_{sp,m}}$
$S_8^{(s)}$ to $S_8^{(l)}$	1	6.72[a]	0	-	1/19[26]
$S_8^{(l)}$ to S_8^{2-}	2	$2\cdot10^{-9}$[a]	1	2.39 [a]	-
S_8^{2-} to S_6^{2-}	3	$2\cdot10^{-11}$[a]	1	2.37 [a]	-
S_6^{2-} to S_4^{2-}	4	$5\cdot10^{-12}$[a]	1	2.24 [a]	-
S_4^{2-} to S^{2-}	5	$5\cdot10^{-10}$[a]	1	2.1 [a]	$1\cdot10^{-4}$[26]
S^{2-} to $Li_2S^{(s)}$	6	$1.2464\cdot10^{-4}$[a]	0	-	-

5.2.2 Governing equation and mass transport

Changes in concentration of each species depend on mass transport and reaction terms, as shown in Equation 8:

$$\frac{\partial}{\partial t}(\varepsilon c_i) = -\frac{\partial N_i}{\partial z} + \sum_m a_s v_{i,m} r_m \qquad (8)$$

where N_i is the mass flux of species *i* and *z* is the distance dimension between anode and cathode. Our model assumes that transport is purely diffusive due to the computational difficulty of including migration with the inner-outer discretization approach (Section 2.4). This assumption has been also used by a previous model with a similar discretization scheme.[29] With this assumption, the flux is given Fick's Law in Equation 9:

$$N_i = -D_{eff,i}\frac{\partial c_i}{\partial z} \qquad (9)$$

where $D_{eff,i}$ is the effective diffusion coefficient. This value is found by adjusted based on porosity using the Bruggeman correlation in Equation 10 [22,30]:

$$D_{eff,i} = D_{0,i}\,\varepsilon^{\beta} \qquad (10)$$

where $D_{0,i}$ is the bulk diffusion coefficient and β is the Bruggeman coefficient.

5.2.3 Cell voltages

The total current I, which is determined externally by the rate of discharge, can be found by integrating all electrochemical reactions over the total cell length l_c:

$$I = \int_0^{l_c} \left(\sum_m -n_m F a_{s,m} v_{i,m} r_m\right) dz \qquad (11)$$

Equation 11 can be solved numerically to find $\phi_{cathode}$ using I and the current concentrations of species. The total cell voltage can be found from the difference of cathode and anode voltages:

$$V_{cell} = \phi_{cathode} - \phi_{anode} \qquad (12)$$

The anode voltage is estimated in Equation 13 using Nernst's equation for lithium metal oxidation[29]:

$$\phi_{anode} = \frac{RT}{F} ln\left(\frac{c_{Li+,anode}}{c_{Li+,ref}}\right) \qquad (13)$$

where $c_{Li+,ref}$ is the reference concentration for lithium ion.

Table 5.2 Bulk diffusion coefficient ($D_{0,i}$), molecular weight (M_i), density (ρ_i), initial concentration ($c_{0,i}$), and initial volume fraction ($\varepsilon_{0,i}$) for molecular species in the model. [a]Assumed parameters.

Species *i*	**$D_{0,i}$ ($m^2 s^{-1}$)**	**M_i (kg mol^{-1})**	**ρ_i (kg m^{-3})**	**$c_{0,i}$ (mol m^{-3})**	**$\varepsilon_{0,i}$**
S_8 (s)	0	0.2565 [26]	2070.4 [26]	-	0.2 [a]
S_8	$1\cdot10^{-9}$ [a]	-	-	17.0 [a]	-
S_8^{2-}	$2.6\cdot10^{-10}$ [31]	-	-	$1\cdot10^{-7}$ [a]	-
S_6^{2-}	$1.7\cdot10^{-10}$ [31]	-	-	$1\cdot10^{-7}$ [a]	-
S_4^{2-}	$1\cdot10^{-9}$ - $1\cdot10^{-13}$ [a]	-	-	0.02416 [a]	-
S^{2-}	$8.6\cdot10^{-11}$ [a]	-	-	$1\cdot10^{-9}$ [a]	-
Li_2S (s)	0	0.0459 [26]	1659.9 [26]	-	0.0001 [a]
Li^+	$4\cdot10^{-10}$ [a]	-	-	1000	-
A^-	$1.24\cdot10^{-10}$ [32]	-	-	1000	-

5.2.4 Cell structure and numerical implementation

We use a 1-dimensional + time numerical approach which models the Li-S full cell. Due to symmetry in the cell structure, we assume that only the dimension separating the anode and the cathode is relevant. The governing equations are discretized using Finite Difference Method to form N=11 segments and solved in Matlab using the ode15s stiff solver. Initial conditions for concentration and volume fraction are listed in Table 5.2. The cell structure is characterized by its porosity, specific surface area, and Bruggeman coefficient, with parameters given in Table 5.3. In order to represent the spherical nature of carbon particles, we construct inner boxes in the cathode region that are connected to a single outer box, shown in Figure 5.1, which are separated from each other by distance l_{io}. The inner box represents the interior of a porous carbon particle, and the outer box represents the exterior of the carbon particle and the surrounding electrolyte. Therefore, species must first travel through the outer boxes and then may travel from an outer box in the cathode into an inner box. The inner boxes have high surface area and tortuosity reflecting the nm-sized pores present in the Ketjen Black carbon used in our experiments. Solid sulfur exists only in the inner cathode region at time 0 to reflect impregnation into porous carbon material. A related discretization approach was published previously by Thangeval et al.[29]

Parameters for the model are taken from experimental sources where possible, but many parameters are not accurately known. In these cases, we assume parameters based on agreement between simulation discharge curves and previously published experimental discharge curves.[23]

Table 5.3 Structural and miscellaneous parameters for the mass transport limited model. [a]Assumed parameters.

Symbol	**Description**	**Value**	**Units**
N	Total number of discretized segments	11	-
N (inner)	Number of segments in the outer cathode region	4	-
N (outer)	Number of segments in the inner cathode region	4	-
l_c	Length of cell	$6\cdot10^{-5,a}$	m
l_{io}	Distance between inner and outer regions	$1\cdot10^{-6,a}$	m
a_s (inner)	Specific surface area in the inner region	$3.6\cdot10^{8,a}$	m^2m^{-3}
a_s(outer)	Specific surface area in the outer region	$4\cdot10^{7,a}$	m^2m^{-3}
β (inner)	Bruggeman coefficient in the inner region	20^a	-
β (outer)	Bruggeman coefficient in the outer region	1.5^{22}	-

ε_c	Carbon volume fraction in cell	0.2^{a}	-
$c_{Li+,ref}^{-}$	Lithium ion reference concentration	1007.64[29]	mol m^{-3}
a_{mtl}	Mass transport limitation prefactor	$1.3\cdot10^{-14,a}$	m^{6} mol^{-2}
b_{mtl}	Mass transport limitation exponential	5^{a}	-
R	Gas constant	8.314	J K^{-1} mol^{-1}
T	Temperature	298.15	K
F	Faraday constant	96485	A mol^{-1}

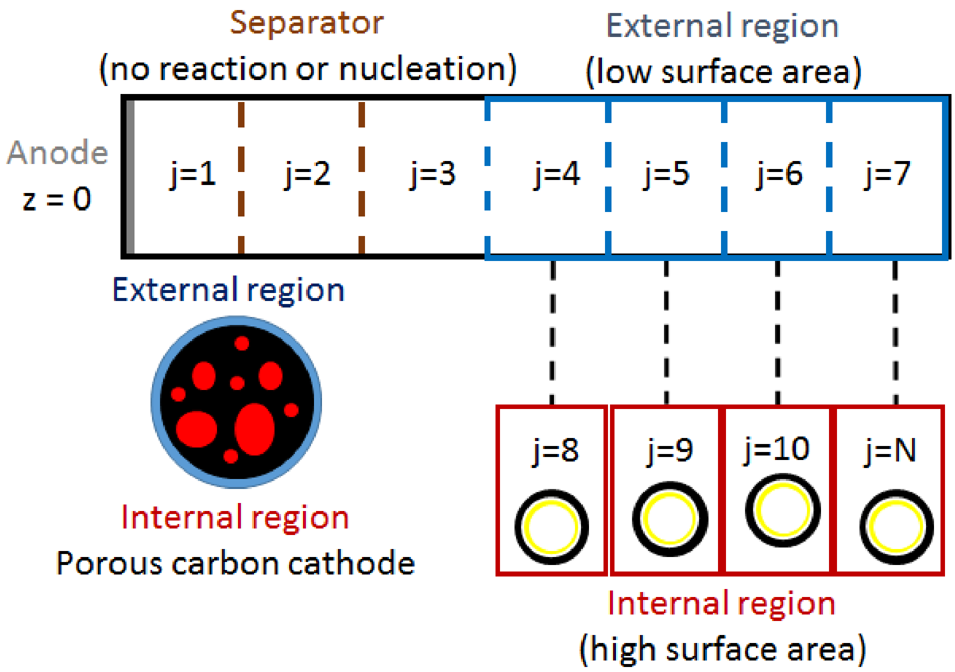

Figure 5.1 Numerical discretization of a lithium-sulfur cell. The cathode was split into an inner and outer region corresponding to the inside and outside of spherical carbon cathode particles. Mass transport from inner regions only travels to the corresponding outer region.

5.3 Li-S coin cell methods and materials

Sulfur powder (S, 1.5 g) was ground with Ketjen Black EC600JD (KB, 0.5g, AkzoNobel) to get a 75:25 S:KB mixture. Then the mixture was heat treated at 155°C for at least 12 h to ensure sulfur impregnation into the porous KB particles.[33] The active material S/KB was then thoroughly mixed for 3h with Super C-65 (MTI Corp.) and the binder polyvinylidene fluoride (PVDF, Aldrich) in N-methyl-2-pyrrolidone (NMP, BDH), in the weight ratio of 70:20:10, respectively. The slurry was cast onto aluminum foil using doctor blade and the sheets were dried in a fume hood at room temperature overnight followed by heat treatment at 60°C oven. The total thickness of aluminum + cathode was 54 microns, and sulfur areal loading was around 1mg cm^{-2} for all cells.

All cells (2032 type) were assembled in an argon filled glovebox. A typical cell consisted of a lithium metal disc (Alfa Aesar) as anode, a S/KB slurry cast as cathode, and a Celgard 2400 separator (25 micron thickness). The electrolyte was 1M (LiTFSI, Sigma-Aldrich) and 0.1M $LiNO_3$ (Sigma-Aldrich) in a 1:1 volume ratio of dioxolane (DOL, Sigma-Aldrich) and dimethoxyethane (DME, Sigma-Aldrich).[34] 10 wt% trimethylolpropane trimethacrylate (TPTA, Sigma-Aldrich) as crosslinker along with 1wt% azobisisobutyronitrile (AIBN, Sigma-Aldrich) as initiator was added to the abovementioned electrolyte for TPTA gel electrolyte cells and cells were assembled after complete dissolution of the components. 5wt% polyhedral oligomeric silsesquioxane methacrylate (POSS, Hybrid Plastic), a cage-like crosslinker, and 1wt% AIBN were used instead for the POSS gel electrolyte cells. A one-hour heat treatment at 60°C was applied to the cells after 3h of rest to gel the electrolyte *in situ*.

Galvanostatic charge-discharge measurements were performed using a MTI

Corporation battery cycler at room temperature. A discharge procedure was used where the cell is first discharged to 1.8V, then paused after discharge, and lastly then discharged a second time to 1.8V before recharging normally. The tests were run with 6 cycles at the same C-rate, with the first 3 cycles having no pause and the second 3 cycles having a pause. The 6 cycles were repeated at successively higher C-rates from 0.1C to 1.0C.

5.4 Results and Discussion

5.4.1 Effect of electrolyte and discharge rate on capacity recovered after pause

In order to investigate the behavior of Li-S cells at the end of discharge, we used a special discharge method in both experiment and simulation tests. This consisted of a normal discharge to the 1.8V lower cutoff, followed by a pause of variable length with zero current, followed lastly by a second discharge at the same rate as the first. At the end of the first discharge, we expect one of three scenarios to occur: first, all polysulfides have been consumed in the entire battery so no more reactants are available; second, insulating lithium sulfide deposits have fully passivated the cathode allowing no further transfer of electrons; or third, polysulfide or lithium ion reactants cannot reach reaction sites fast enough due to a mass transport limitation. Only in the third scenario would it be possible to see additional capacity during the second discharge after the pause.

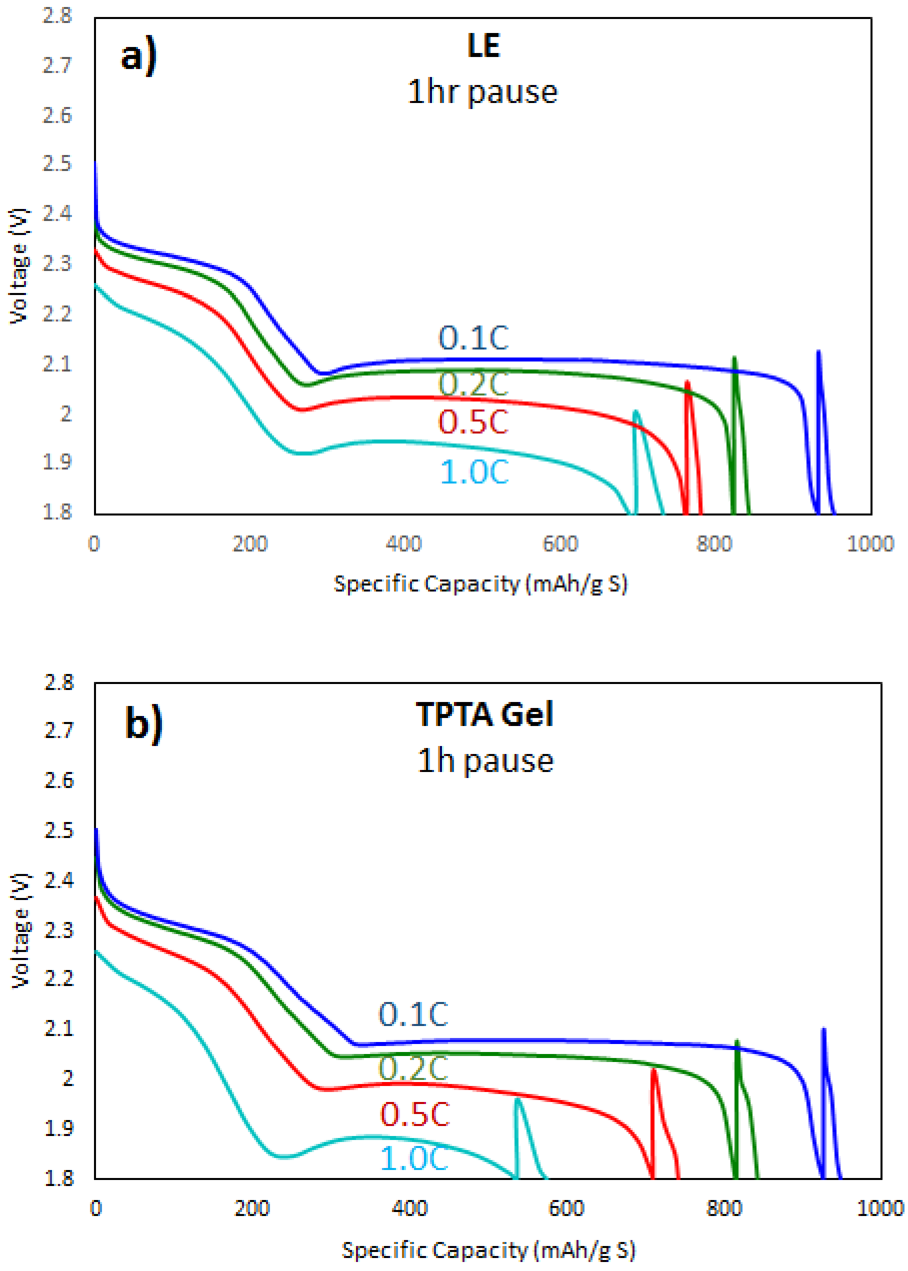

Figure 5.2 Li-S coin cell discharge curves with pause for four discharge rates. (a) shows liquid electrolyte and (b) shows TPTA gel polymer electrolyte. The batteries were discharged normally to 1.8V, paused for 1hr, and then discharged again to 1.8V before charging normally. Experiments performed by Dr. Somayeh Zamani.

The discharge curves for the liquid electrolyte and TPTA gel electrolyte systems for a 1 hour pause are shown in Figures 5.2a and 5.2b. Capacities are scaled by grams of sulfur used in the cell. The 1 hour pause occurs after the voltage reaches 1.8V the first time in the plot. A comparison of Figures 5.2a and 5.2b shows that liquid electrolyte has better performance and rate capability, which is due to the worsened ionic conductivity in the gelled system. After the pause, both liquid and gel electrolytes show recovered capacity, which demonstrates that some change happened within the cell during the 1 hour pause. The fact that any capacity is recovered suggests that passivation mechanisms are not the sole cause of discharge failure in these cells.[23] If passivation caused the discharge failure, we would expect to see little to no capacity recovered after pause, so a more likely explanation is that at end of discharge the cell faces a mass transport limitation.[24] Both gel and liquid electrolytes also show increased capacity after pause as the C-rate increases, which further suggests that mass transport plays an important role at the end of discharge. Similar results were also observed for the POSS gel system, shown in Figure 5.7 in section 5.6.1. Mass transport in the cathode is affected by the lithium sulfide deposition, which reduces porosity and constricts diffusion pathways, but will also be affected by the diffusion of species, raising questions regarding the mechanism behind the recovery and the effect of the gel electrolyte.

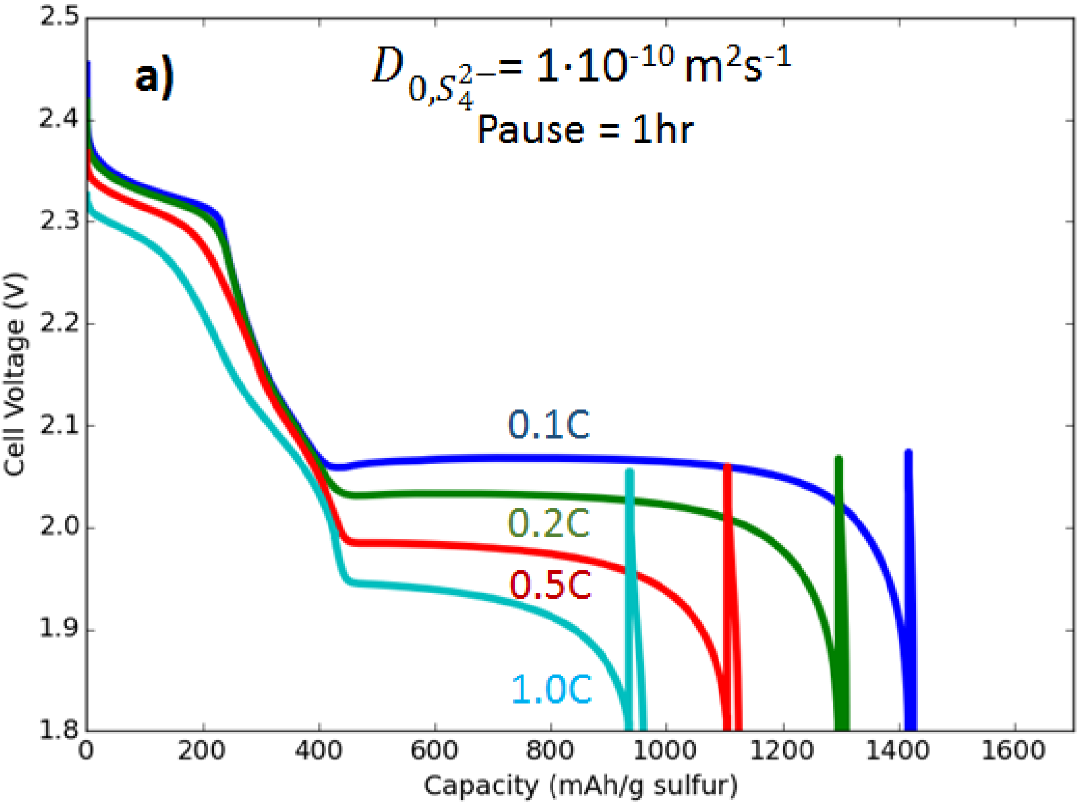
a)
$D_{0,S_4^{2-}} = 1\cdot10^{-10}\ m^2s^{-1}$
Pause = 1hr
0.1C
0.2C
0.5C
1.0C
Cell Voltage (V)
Capacity (mAh/g sulfur)
2.5
2.4
2.3
2.2
2.1
2.0
1.9
1.8
0
200
400
600
800
1000
1200
1400
1600

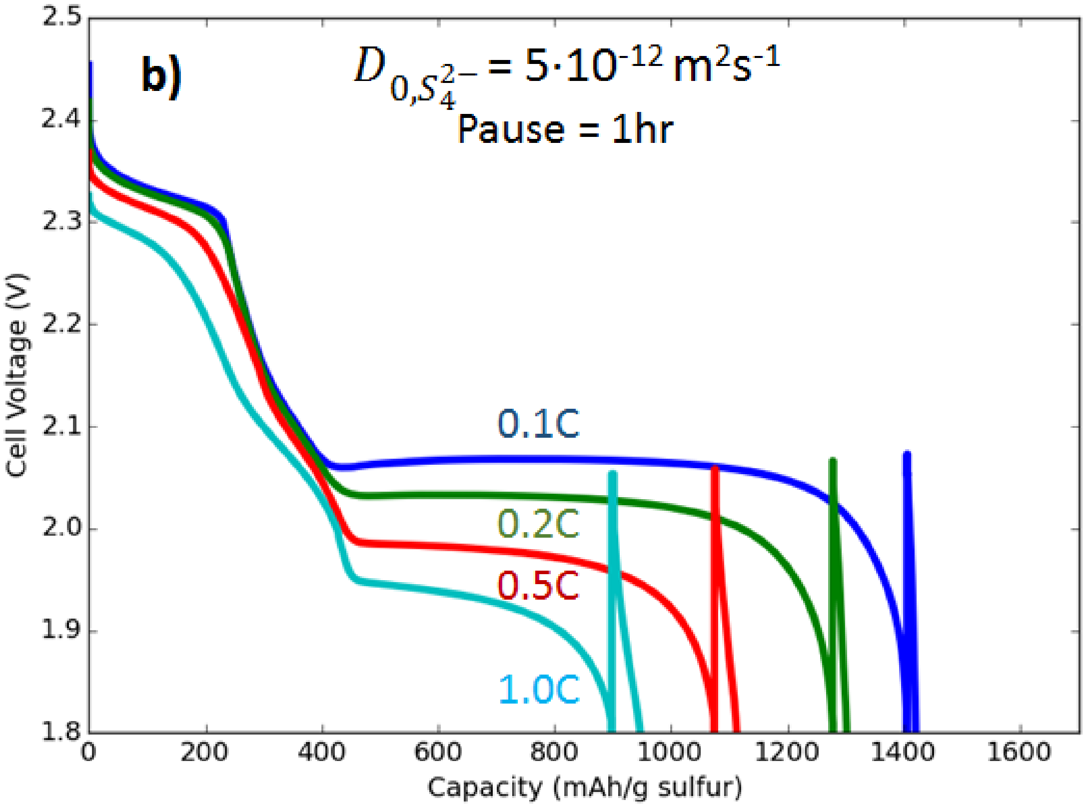

Figure 5.3 Li-S numerical simulation discharge curves with 1 hr pause for four discharge rates. (a) shows the case of faster S_4^{2-} diffusion which and (b) shows slower S_4^{2-} diffusion.

Using the numerical model presented in Section 5.2, we perform the same discharge procedure with 1 hour pause in order to investigate the behavior observed in experiment. As the 2nd plateau discharge region involves the conversion of Li_2S_4 and there is evidence of mass transport limitation, we use the model to investigate the effect of Li_2S_4 diffusion coefficient on the end of discharge performance. Figure 5.3 shows the simulation results for multiple C-rates and two Li_2S_4 diffusion coefficients. The numerical model reproduces the characteristic shape of the Li-S discharge profile, and its capacities are comparable with those predicted by Andrei et al.[23] Due to the assumptions in the model such as perfect carbon conductivity, full utilization of solid sulfur, and no shuttle effect, the model represents a more ideal case with higher discharges capacities compared to experiment. The simulation results show similar trends as experiment, with some capacity recovered after pause and increasing recovery at higher C-rates. In addition, with slower Li_2S_4 diffusion, the simulation predicts larger capacity recovery after pause, which corresponds to the gel system where diffusion is more difficult.

The trends in C-rate and Li_2S_4 diffusion can be explained by considering the transport of Li_2S_4 during cell discharge. Between the capacities of around 300 to 400 $mAhg^{-1}$ in Figure 3, Li_2S_4 is being produced at the cathode. This creates a concentration gradient from the cathode to anode leading to diffusion of Li_2S_4 away from the cathode inner regions to the cathode outer regions and separator. Later, as Li_2S_4 is consumed in the 2nd plateau region of Figure 5.3 with capacities greater than 400 $mAhg^{-1}$, Li_2S_4 that previously drifted away from the cathode begins to diffuse back. Based on the C-rate, which controls the amount of time for the process to occur, and the diffusion coefficient, differing amounts of Li_2S_4 may remain in the cell. The subsequent pause provides additional time for Li_2S_4 to diffuse back to the cathode where it can be converted to yield additional capacity once the second discharge begins. Therefore, at higher C-rates, Li_2S_4 has less time to return to the cathode during the 2nd plateau, leading to greater benefits after the pause. Likewise, slower diffusion in Figure 5.3b results in greater recovery after pause than in Figure 5.3a as fewer polysulfides were able to return to the cathode during the first discharge.

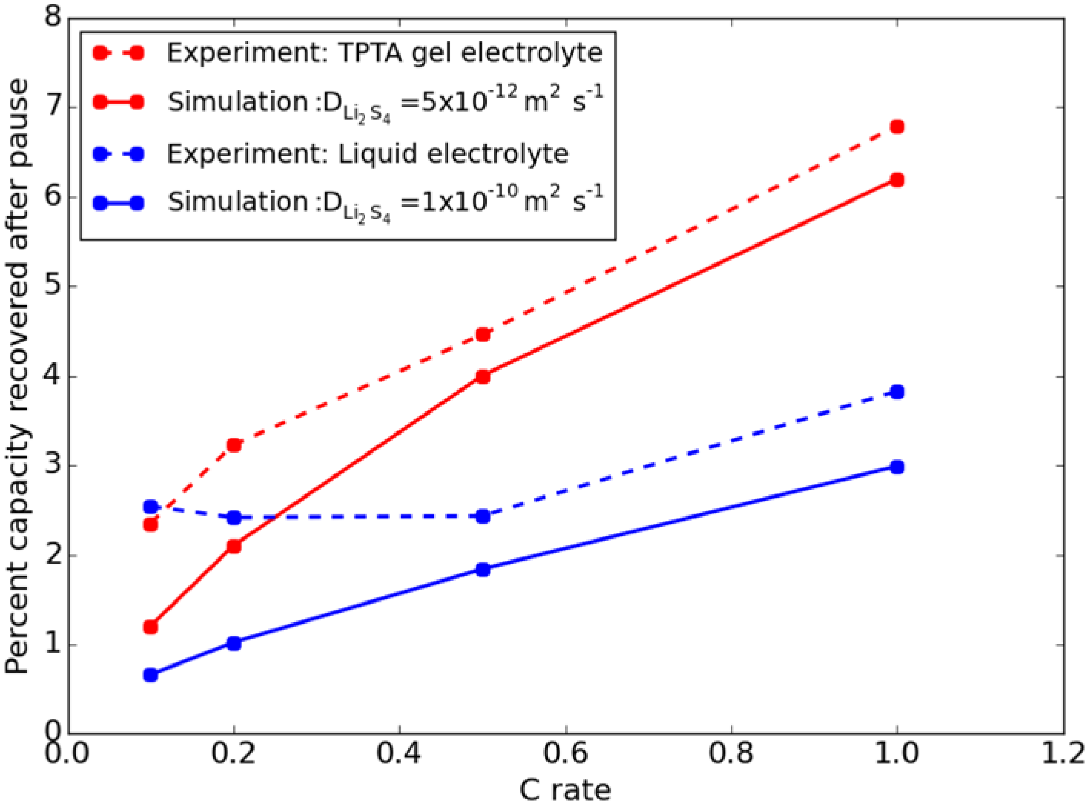

Figure 5.4 Percent recoveries for 1 hour pause discharge for experiment and simulation. Percent recovery after pause was calculated by dividing the capacity gained after pause by the total capacity.

To evaluate this explanation, we compared the experiment and model predictions. To do this we calculated the percent recovery after pause, which is equal to the capacity gained during the second discharge divided by the total discharge capacity. The percent recoveries for simulation and experiment for 1 hour pause time are shown in Figure 5.4. For experiment, the pause recovery presented is an average over three identical, consecutive cycles. Although the model underpredicts the percent capacity, likely due to the higher total capacity predicted in the model, the simulation and experiment show similar increasing recovery with C-rate. Also, the gel electrolyte percent recovery is higher than the liquid case. By reducing the Li_2S_4 diffusion coefficient, the simulation predicts a similar increase in recovery due to the inability of Li_2S_4 to return to the cathode fast enough near the end of discharge.

Although our model shows that it is possible to explain the experimental results by varying Li_2S_4 mass transport, it is difficult to separate the effect of lithium ion transport in the experimental results. To investigate lithium ion effects further, we tested liquid and gel systems with 1.5M LiTFSI instead of 1.0M. If the capacity recovery in experiment is due to a lithium ion mass transport limitation instead of Li_2S_4, we would expect to see some change in total capacity and recovered capacity with more plentiful lithium ions. In Figure 5.8 in section 5.6.1, the 1.5M LiTFSI results were nearly identical to the results in Figure 5.2a using 1.0M LiTFSI, indicating that lithium ion transport limitations cannot explain the capacity recovery effect.

Another point which should be considered is the effect of migration on the lithium and polysulfide ions. The numerical model does not include the effects of migration, which limits the simulation to only investigating diffusion driven effects. However, if migration was included, it would increase the movement of lithium ions towards the cathode and polysulfide ions toward the anode during discharge. Therefore, migration would decrease lithium ion mass transport problems and increase polysulfide mass transport problems compared to only considering diffusion.

5.4.2 Effect of pause time on capacity recovered after pause

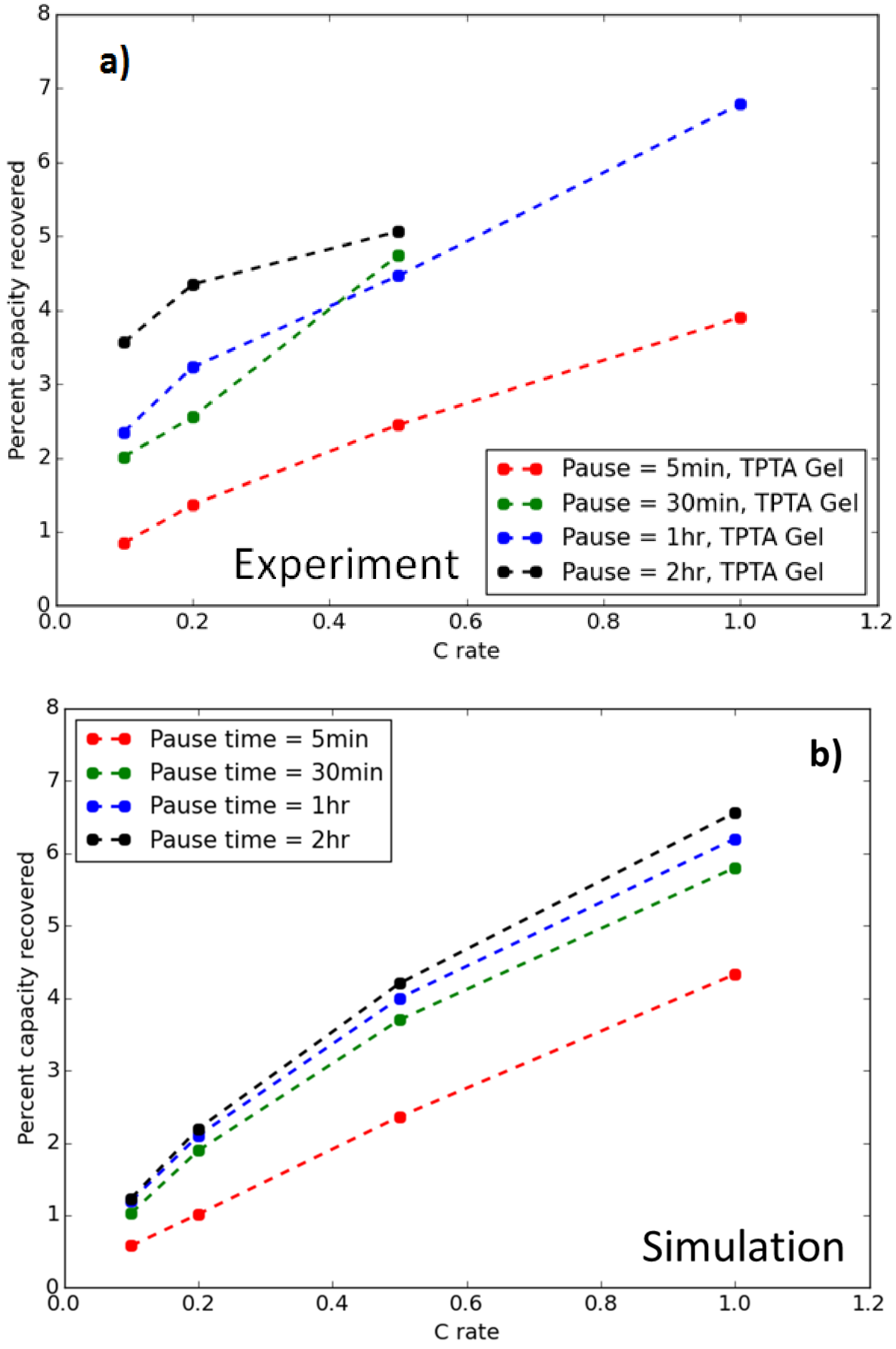

Figure 5.5 Effect of pause time on percent capacity recovered after pause for experiment (a) and simulation (b). $D_{0,S_4^{2-}}$= $1\cdot10^{-11}$ m^2s^{-1} for the simulation results.

The discharge with pause experiments and simulations were performed for pause durations between 5 minutes and 2 hours duration to investigate the time scale of the capacity recovery mechanism. The results for TPTA gel and simulation are shown in Figure. 5.5a and 5.5b, respectively. Similar results for LE and POSS gel can be found in Figure 5.9 in section 5.6.1. In Figure 5.5a, all pause times show similar increases with C-rate as was observed for the 1 hour tests discussed previously. In addition, longer pause times generally cause an increase in percent recovery due to the increased time provided for polysulfides to return to exhausted cathode reaction sites. In Fig. 5b, this mechanism is confirmed by simulations with varying pause times that show similar trends, although the model underestimates the recovery for long pauses with low C-rate. This is again likely due to the difference in total capacity between experiments and simulation influencing the percent capacity metric. It also suggests that in addition to diffusion, there is a longer time scale process occurring during discharge and pause. This could be a slow release of polysulfides trapped in the separator or gel electrolyte that is not included in the simulation model.

Surprisingly, even a short 5 minute pause is sufficient to recover approximately 1-4% capacity in the TPTA system. The 5 minute pause is quite short in comparison to the total discharge time of 10 hours at 0.1C or 1 hour at 1C. However, it is important to note that mass transport limitations will not come into effect until near the end of discharge when there is large deposits of lithium sulfide in the cathode and low Li_2S_4 concentrations, as modeled by Equation 4. The increasing recovery at longer times shows that the process of Li_2S_4 returning to the cathode has only partially completed at short times. As the recovery during pause is driven by diffusion, less marginal improvement is expected at long pause times where the diffusion gradients have become less steep. This explains why much of the recovery occurs in the first 5 minutes when the diffusion gradients are steepest. The results in Figures 5.5a and 5.5b further demonstrate that the pause recovery is driven by a mass transport mechanism with a time scale on the order of hours.

5.4.3 Cell voltage after pause

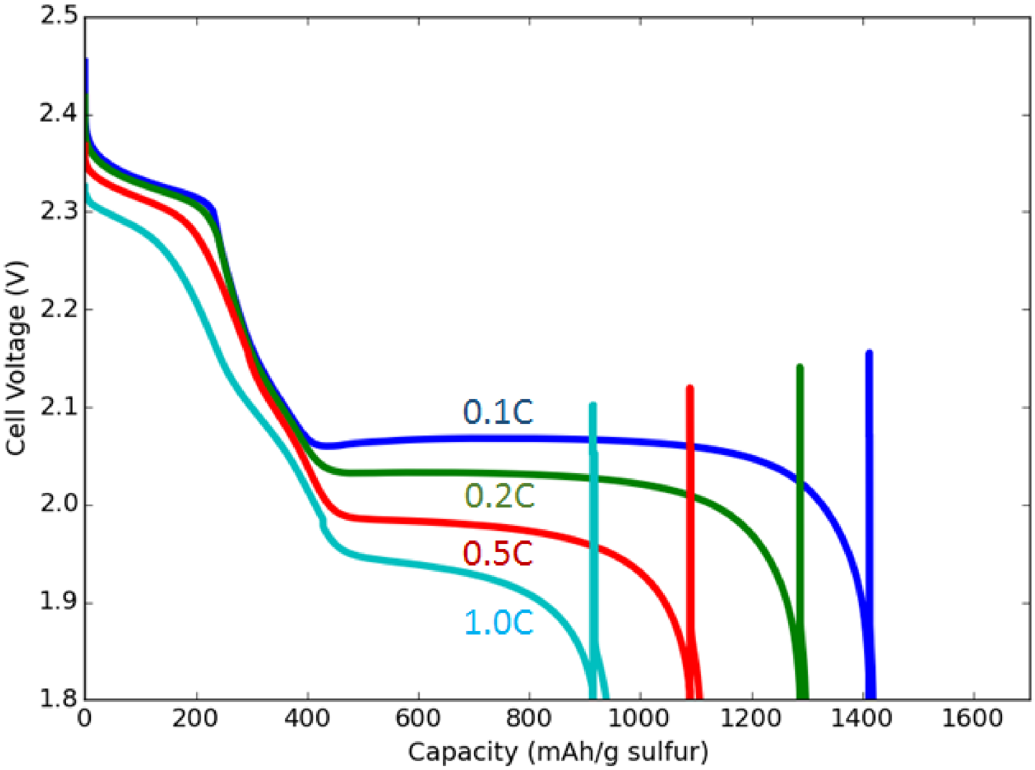

Figure 5.6 Simulated discharge curves with S_6^{2-} reactions disabled after the 1 hour pause. The lower voltages compared to Figure 2a suggest that S_6^{2-} is still present at the end of discharge. $D_{0,S_4^{2-}} = 1 \cdot 10^{-11}$ m^2s^{-1}.

Referring to Figure 5.2a and Figure 5.2b, the voltage immediately after the pause (2.1V-1.97V for different C-rates, TPTA) is higher than the voltage seen in the plateau region before the pause (2.08V to 1.89V). This is true for all C-rates and electrolytes but becomes more apparent at 0.5C and 1.0C. Although the voltage after the pause rapidly declines until 1.8V, a notable amount of capacity is produced at these higher voltages. This suggests that higher order polysulfide reactions could be taking place after pause, as they react at a higher open circuit voltage. The initial discharge voltages after pause are the same as corresponding voltages earlier during discharge when Li_2S_6 was being converted into Li_2S_4. Therefore, we performed a modified simulation where Li_2S_6 reactions were artificially disabled after the pause. The results are shown in Figure 5.6. Compared to the voltage profiles after pause in Figure 5.3a and Figure 5.3b, the simulation with Li_2S_6 reactions disabled after pause yields recovered capacity at a much lower voltage. This suggests that Li_2S_6 reactions are occurring after the pause and can explain the results seen in Figure 5.2. We propose that although much of the Li_2S_6 is consumed much earlier during discharge, some diffuses away from the cathode. This Li_2S_6 then gradually returns while the cell is in the plateau region and is instantly consumed alongside the predominant Li_2S_4 species due to its reaction having a higher open circuit voltage. During the pause, Li_2S_6 is able to return and begins to accumulate instead of instantly being consumed. Then, when the pause ends, the Li_2S_6 is consumed at higher voltage followed by the Li_2S_4 at lower voltage, leading to the observed behavior.

5.5 Conclusions

In summary, we have demonstrated that by pausing after discharge, additional capacity can be recovered for both liquid and gel systems. The recovery mechanism was explored using numerical simulation and determined to be related to mass transport limitations as Li_2S_4 diffusion to and from the cathode during discharge. Due to the slower diffusion in the gel electrolyte system compared to liquid, increased percent capacities were recovered. In addition, the higher voltages obtained after pause were proposed to be due to residual Li_2S_6 species still present in the cell at the end of discharge. These results suggest that Li-S battery discharge capacity can be improved by either limiting polysulfide escape from the cathode or speeding its return to the cathode, especially for gel electrolyte systems. This agrees with numerous experimental works that have shown improvements by limiting polysulfide diffusion.[35–41] To further expand upon these results, the role of lithium ion diffusion in the pause recovery must be better understood as well as polysulfide adsorption effects in the cathode, which play an important role in polysulfide mass transport away from the cathode.

5.6 Supplemental information

5.6.1 Additional gel and electrolyte with pause results

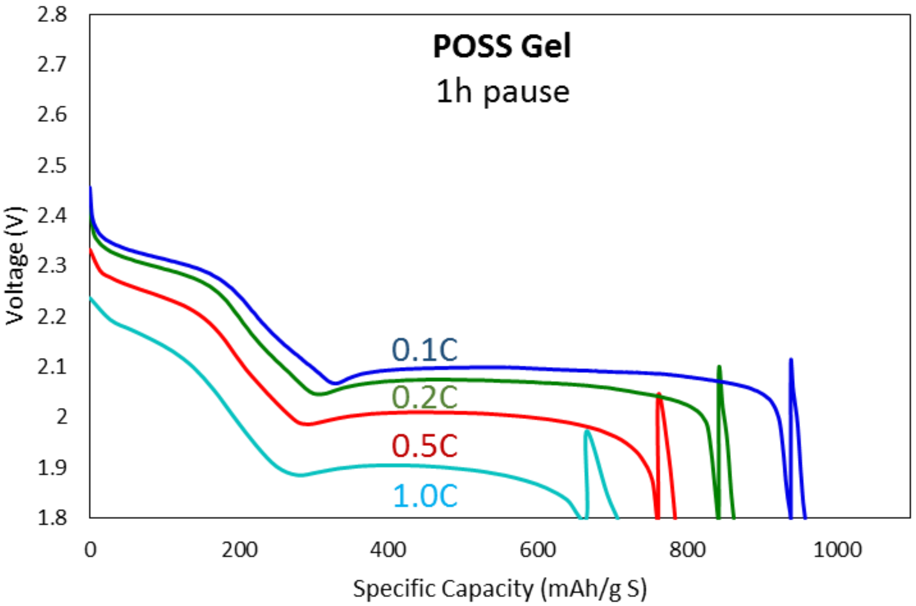

Figure 5.7 POSS gel polymer electrolyte coin cell discharge curves with 1hr pause for four discharge rates.

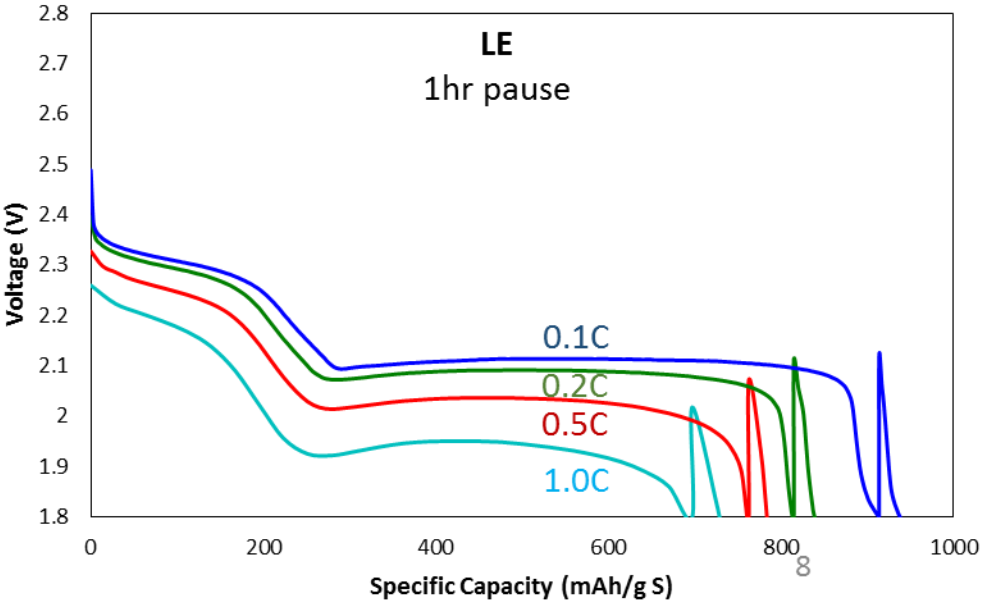

Figure 5.8 Liquid electrolyte coin cell discharge curves with 1hr pause for four discharge rates with increased LiTFSI concentration (1.0M to 1.5M).

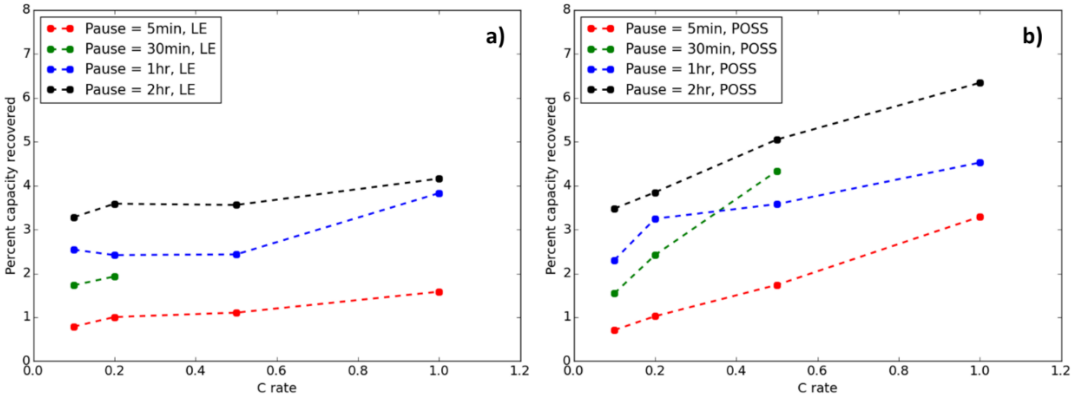

Figure 5.9 Coin cell results for the effect of pause time on percent capacity recovered after pause for liquid electrolyte (a) and POSS gel polymer electrolyte (b).

5.6.2 Effect of material properties using the mass transport limited model

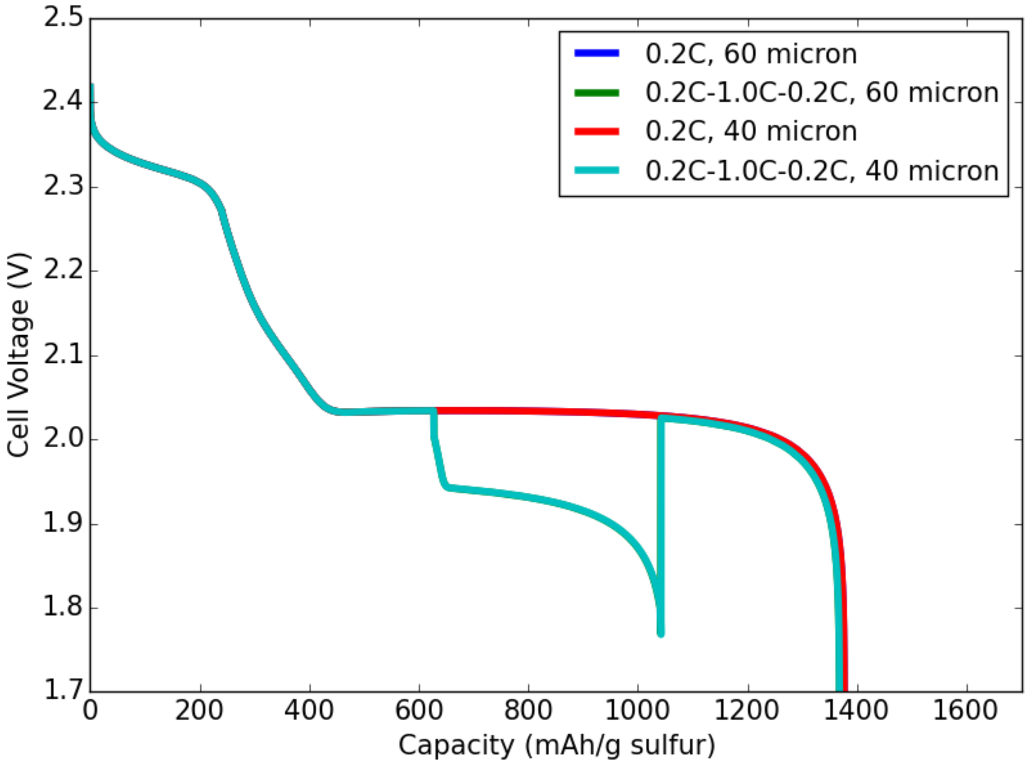

Figure 5.10 Simulated effect of cell thickness on discharge behavior for singe C-rate and multi C-rate discharge.

The effect of cell thickness (not including lithium metal) on performance is explored using the mass transport limited model in Figure 5.10. The multi C-rate test refers to discharging at 0.2C until half of maximum capacity, discharge at 1.0 C until 1.8V, and then discharging at 0.2C again until 1.8V. This test allows the failure mechanisms at the end of discharge to be investigated along the lines of Chapter 4.

Scaling up the cell thickness from 40 micron to 60 micron had no effect on the performance or the mass transport limitation. This demonstrates that in the model, mass transport limitations derive from the movement of polysulfide and lithium from the outer cathode regions into the inner cathode regions, and not from movement through the separator or the bulk electrolyte. This is because the deposition of lithium sulfide in the cathode greatly slows diffusion near the end of discharge, as opposed to the bulk electrolyte and separator where it is unlikely that lithium sulfide will deposit.

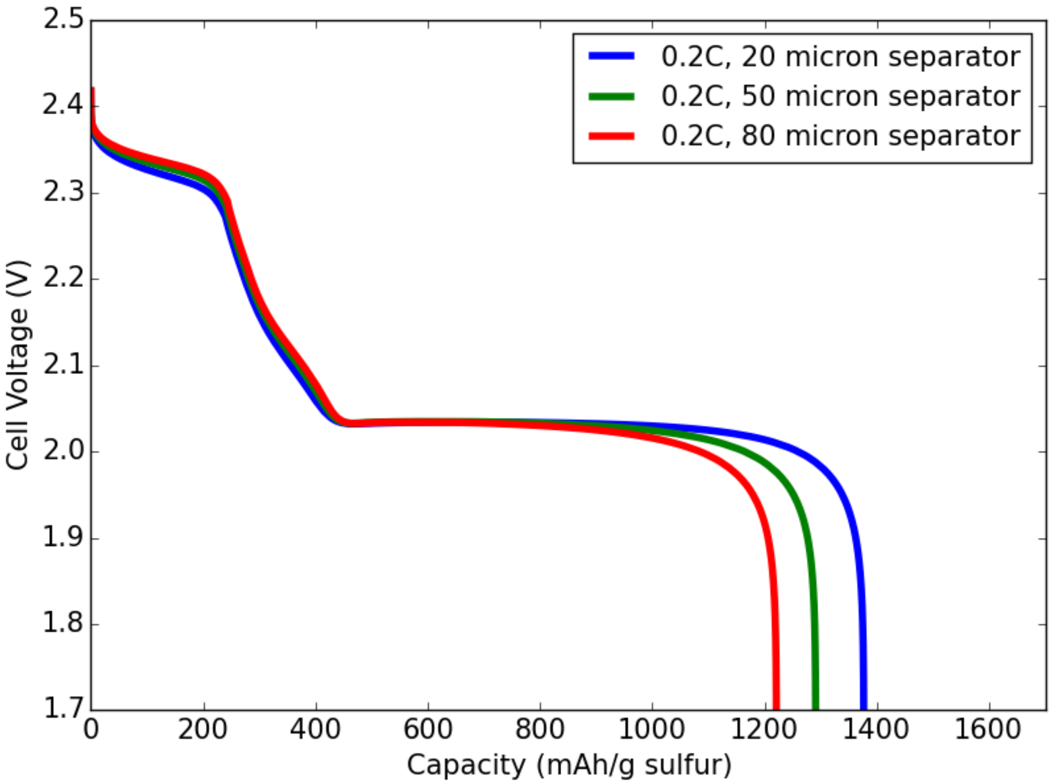

Figure 5.11 Mass transport limited model for different separator thicknesses at 0.2C. All other parameters were kept constant.

In Figure 5.11, instead of scaling up the entire cell as in Figure 5.10, the separator thickness is increased instead while keeping the cathode the same. This results in a larger total volume in the cell and effectively a larger electrolyte volume, diluting the lithium ions and polysulfides. This dilution results in a faster loss of polysulfides from the cathode during the initial stages of discharge. This actually slightly improves overpotentials in the Stage 1 and 2 regions due to the diminished buildup of reaction products. However, at the end of discharge the mass transfer limitation is reached sooner for larger separators leading to diminished capacity. The same dilution of polysulfides results in insufficient Li_2S_4 in the cathode, preventing full utilization of polysulfides in the battery.

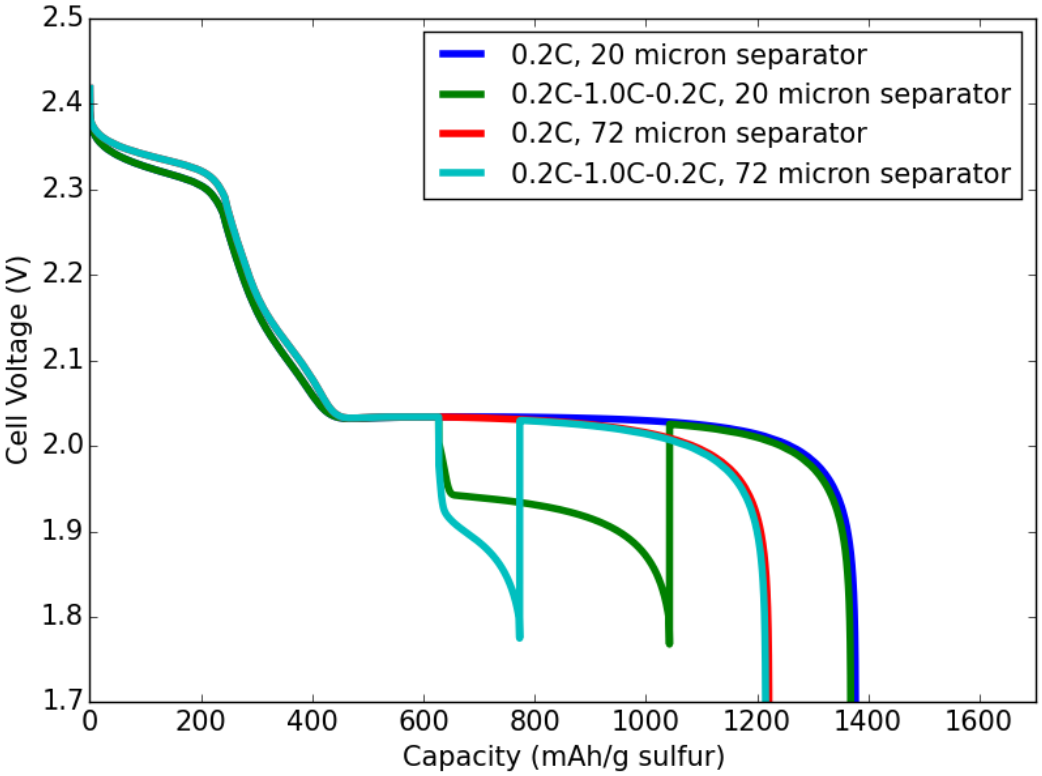

Figure 5.12 Multi C-rate mass transport limited model for different separator thicknesses at 0.2C. All other parameters were kept constant.

In Figure 5.12, larger separators and electrolyte volume are tested with the multi C-rate test. Although the larger separator has lower performance overall for the same reasons as Figure 5.11, it is especially worse at the higher C-rate. At the slower C-rate of 0.2, the dilution of polysulfides and lithium ions has less of an effect due to the large amount of time during the discharge. When discharge is fast, however, polysulfides that were diluted away earlier during discharge have much less time to return.

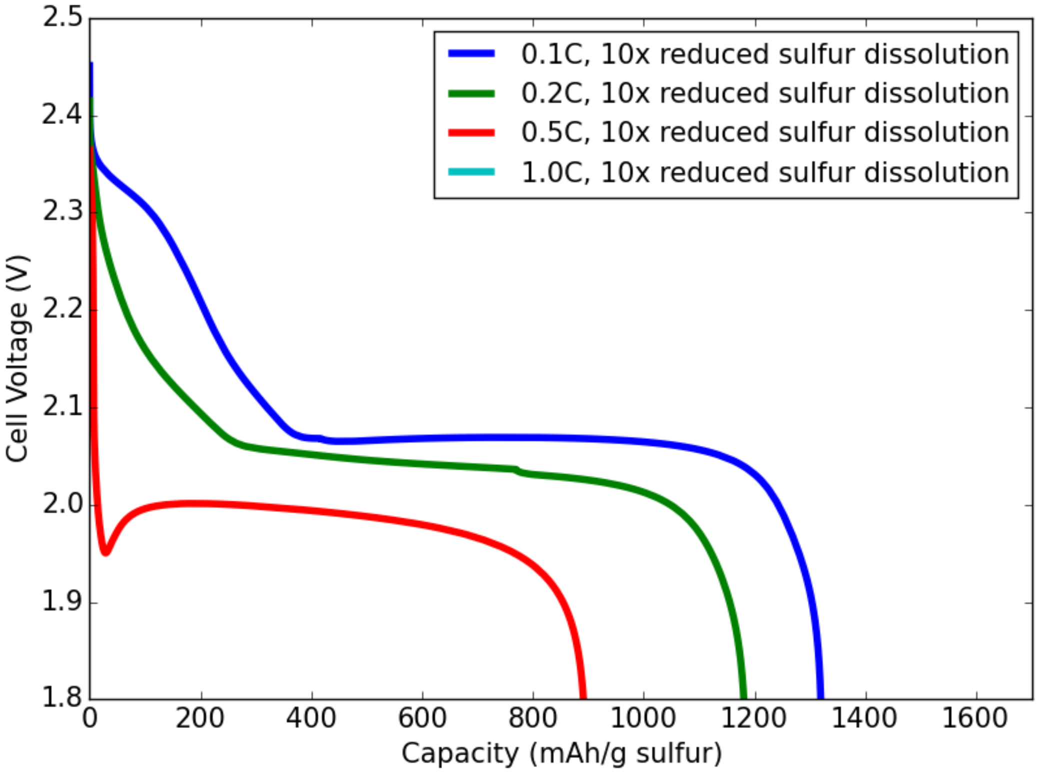

Figure 5.13 Mass transport limited model for slow sulfur dissolution.

Occasionally, poor performing lithium-sulfur batteries exhibit a reduced or completely missing region 1 and 2 of the discharge curve. In the simulation, this behavior is observed when the solid sulfur dissolution rate is too slow, which is plotted in Figure 5.13. If elemental sulfur cannot come into contact with the electrolyte and incoming lithium ions, it will not be converted into polysulfides. Under these conditions, the battery is forced to begin to convert Li_2S_8, Li_2S_6, and Li_2S_4 prematurely in order to satisfy the demanded output current. If all of the sulfur is dissolved eventually, capacities can still be high as elemental sulfur will continue to be converted throughout the entire discharge. In experiment, these poor-performing conditions could be caused by insufficient electrolyte wetting of the cathode, which could limit the dissolution of elemental sulfur.

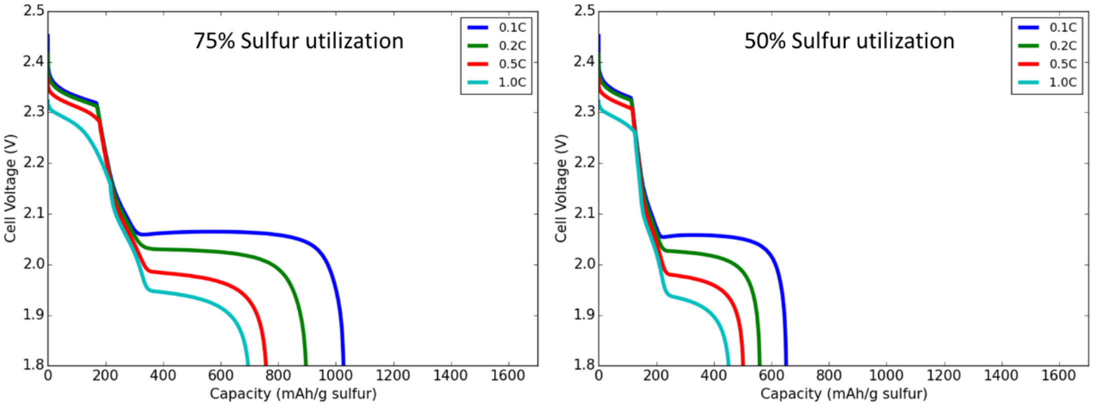

Figure 5.14 Effect of incomplete sulfur utilization using the mass transport limited model.

Referring to Figure 5.2a, the 0.1C discharge profile reaches about 950 mAh/g sulfur total capacity and about 300 mAh/g sulfur capacity at the beginning of region 3. With full conversion of long chain polysulfide, the capacity at the beginning of region 3 should be about 400 mAh/g as in Figure 5.12. This suggests that of the grams of sulfur added initially to the better, some portion has been lost. The lost sulfur could be due to inaccessible sulfur within the cathode, side reactions during cycling, and polysulfides trapped in edges of the separator. To address the case when some sulfur has becoming unusable within the battery, a sulfur utilization parameter is set where only a portion of sulfur is allowed to react in the simulation. This is plotted in Figure 5.14 for 75% sulfur utilization and 50% sulfur utilization. As expected, capacities of all discharge regions are scaled back to reflect the missing reactants. The 75% utilization results are especially comparable to Figure 5.2a, and demonstrates that a straightforward explanation of inaccessible sulfur can be used to explain some of the sub-theoretical Li-S battery performance.

5.7 References

1. Hannan, M. A., Hoque, M. M., Mohamed, A. & Ayob, A. Review of energy storage systems for electric vehicle applications: Issues and challenges. *Renew. Sustain. Energy Rev.* **69**, 771–789 (2017).
2. Manthiram, A., Fu, Y., Chung, S.-H., Zu, C. & Su, Y.-S. Rechargeable Lithium–Sulfur Batteries. *Chem. Rev.* **114**, 11751–11787 (2014).
3. Liu, J. *et al.* Minimizing Polysulfide Shuttle Effect in Lithium-Ion Sulfur Batteries by Anode Surface Passivation. *ACS Appl. Mater. Interfaces* **10**, 21965–21972 (2018).
4. Wang, Q. *et al.* A shuttle effect free lithium sulfur battery based on a hybrid electrolyte. *Phys. Chem. Chem. Phys.* **16**, 21225–21229 (2014).
5. Liu, M. *et al.* Suppressing Self-Discharge and Shuttle Effect of Lithium-Sulfur Batteries with V 2 O 5 -Decorated Carbon Nanofiber Interlayer. *Small* **13**, 1602539 (2017).
6. Hofmann, A. F., Fronczek, D. N. & Bessler, W. G. Mechanistic modeling of polysulfide shuttle and capacity loss in lithium-sulfur batteries. *J. Power Sources* **259**, 300–310 (2014).
7. Mikhaylik, Y. V & Akridge, J. R. Polysulfide Shuttle Study in the Li/S Battery System. *J. Electrochem. Soc.* **151**, A1969 (2004).
8. Liu, S. *et al.* Hollow carbon spheres with nanoporous shells and tailored

chemical interfaces as sulfur host for long cycle life of lithium sulfur batteries. *Electrochim. Acta* **279**, 10–18 (2018).

9. Gueon, D. *et al.* Spherical Macroporous Carbon Nanotube Particles with Ultrahigh Sulfur Loading for Lithium-Sulfur Battery Cathodes. *ACS Nano* **12**, 226–233 (2018).
10. Lu, D. *et al.* Enabling High-Energy-Density Cathode for Lithium-Sulfur Batteries. *ACS Appl. Mater. Interfaces* **10**, 23094–23102 (2018).
11. He, X. *et al.* Expansion and shrinkage of the sulfur composite electrode in rechargeable lithium batteries. *J. Power Sources* **190**, 154–156 (2009).
12. Zhang, K., Zhao, Q., Tao, Z. & Chen, J. Composite of sulfur impregnated in porous hollow carbon spheres as the cathode of Li-S batteries with high performance. *Nano Res.* **6**, 38–46 (2013).
13. Wu, D. S. *et al.* Quantitative investigation of polysulfide adsorption capability of candidate materials for Li-S batteries. *Energy Storage Mater.* **13**, 241–246 (2018).
14. Zhang, X. Q., He, B., Li, W. C. & Lu, A. H. Hollow carbon nanofibers with dynamic adjustable pore sizes and closed ends as hosts for high-rate lithium-sulfur battery cathodes. *Nano Res.* **11**, 1238–1246 (2018).
15. Song, J. Y., Wang, Y. Y. & Wan, C. C. Review of gel-type polymer electrolytes for lithium-ion batteries. *J. Power Sources* **77**, 183–197 (1999).
16. Cheng, X., Pan, J., Zhao, Y., Liao, M. & Peng, H. Gel Polymer Electrolytes for Electrochemical Energy Storage. *Adv. Energy Mater.* **8**, 1–16 (2018).
17. Stephan, A. M. Review on gel polymer electrolytes for lithium batteries. *Eur.*

Polym. J. **42**, 21–42 (2006).

18. Kim, J. K. Hybrid gel polymer electrolyte for high-safety lithium-sulfur batteries. *Mater. Lett.* **187**, 40–43 (2017).

19. Natarajan, A., Stephan, A. M., Chan, C. H., Kalarikkal, N. & Thomas, S. Electrochemical studies on composite gel polymer electrolytes for lithium sulfur-batteries. *J. Appl. Polym. Sci.* **134**, 1–8 (2017).

20. Chen, J. *et al.* Improving Lithium-Sulfur Battery Performance under Lean Electrolyte through Nanoscale Confinement in Soft Swellable Gels. *Nano Lett.* **17**, 3061–3067 (2017).

21. Liu, M. *et al.* Novel gel polymer electrolyte for high-performance lithium-sulfur batteries. *Nano Energy* **22**, 278–289 (2016).

22. Kumaresan, K., Mikhaylik, Y. & White, R. E. A Mathematical Model for a Lithium–Sulfur Cell. *J. Electrochem. Soc.* **155**, A576 (2008).

23. Andrei, P., Shen, C. & Zheng, J. P. Theoretical and experimental analysis of precipitation and solubility effects in lithium-sulfur batteries. *Electrochim. Acta* **284**, 469–484 (2018).

24. Zhang, T., Marinescu, M., Walus, S., Kovacik, P. & Offer, G. J. What Limits the Rate Capability of Li-S Batteries during Discharge: Charge Transfer or Mass Transfer? *J. Electrochem. Soc.* **165**, A6001–A6004 (2018).

25. Pan, H. *et al.* On the Way Toward Understanding Solution Chemistry of Lithium Polysulfides for High Energy Li-S Redox Flow Batteries. *Adv. Energy Mater.* **5**, 1–7 (2015).

26. Danner, T., Zhu, G., Hofmann, A. F. & Latz, A. Modeling of nano-structured

cathodes for improved lithium-sulfur batteries. *Electrochim. Acta* **184**, 124–133 (2015).

27. Bard, Allen J.; Faulkner, L. R. *Electrochemical Methods*. *John Wiley & Sons, Inc.* (2004).

28. Bazant, M. Z. Theory of chemical kinetics and charge transfer based on nonequilibrium thermodynamics. *Acc. Chem. Res.* **46**, 1144–1160 (2013).

29. Thangavel, V. *et al.* A Microstructurally Resolved Model for Li-S Batteries Assessing the Impact of the Cathode Design on the Discharge Performance. *J. Electrochem. Soc.* **163**, A2817–A2829 (2016).

30. Tjaden, B., Cooper, S. J., Brett, D. J., Kramer, D. & Shearing, P. R. On the origin and application of the Bruggeman correlation for analysing transport phenomena in electrochemical systems. *Current Opinion in Chemical Engineering* **12**, 44–51 (2016).

31. Lu, Y. C., He, Q. & Gasteiger, H. A. Probing the lithium-sulfur redox reactions: A rotating-ring disk electrode study. *J. Phys. Chem. C* **118**, 5733–5741 (2014).

32. Valøen, L. O. & Reimers, J. N. Transport Properties of LiPF6-Based Li-Ion Battery Electrolytes. *J. Electrochem. Soc.* **152**, A882 (2005).

33. Halim, W. *et al.* Directly deposited binder-free sulfur electrode enabled by air-controlled electrospray process. *ACS Appl. Energy Mater.* **2**, 678–686 (2019).

34. Lee, J. H. *et al.* Effective Suppression of the Polysulfide Shuttle Effect in Lithium-Sulfur Batteries by Implementing rGO-PEDOT:PSS-Coated Separators via Air-Controlled Electrospray. *ACS Omega* **3**, 16465–16471 (2018).

35. Tao, X. *et al.* Balancing surface adsorption and diffusion of lithium-polysulfides on nonconductive oxides for lithium-sulfur battery design. *Nat. Commun.* **7**, 1–9 (2016).

36. Williams, B. P. & Joo, Y. L. Tunable Large Mesopores in Carbon Nanofiber Interlayers for High-Rate Lithium Sulfur Batteries. *J. Electrochem. Soc.* **163**, A2745–A2756 (2016).

37. Lee, J. *et al.* Facile and scalable fabrication of highly loaded sulfur cathodes and lithium–sulfur pouch cells via air-controlled electrospray. *Mater. Today Energy* **6**, 255–263 (2017).

38. Song, J. *et al.* Strong lithium polysulfide chemisorption on electroactive sites of nitrogen-doped carbon composites for high-performance lithium-sulfur battery cathodes. *Angew. Chemie - Int. Ed.* **54**, 4325–4329 (2015).

39. Chung, S. H. & Manthiram, A. A polyethylene glycol-supported microporous carbon coating as a polysulfide trap for utilizing pure sulfur cathodes in lithium-sulfur batteries. *Adv. Mater.* **26**, 7352–7357 (2014).

40. Zhou, T. *et al.* Twinborn TiO2-TiN heterostructures enabling smooth trapping-diffusion-conversion of polysulfides towards ultralong life lithium-sulfur batteries. *Energy Environ. Sci.* **10**, 1694–1703 (2017).

41. Liu, J. *et al.* SnO2 as a high-efficiency polysulfide trap in lithium-sulfur batteries. *Nanoscale* **8**, 13638–13645 (2016).

CHAPTER 6

MOLECULAR DYNAMICS SIMULATIONS OF GRAPHENE AND GRAPHITE PROCESSING: PRELIMINARY STUDIES

6.1 Introduction

6.1.1 Graphitic materials

Interest in graphene has surged exponentially in the last few years due to its extraordinary physical properties. Graphene is a 2-d sheet of carbon atoms arranged in a hexagonal pattern, with each carbon bonded to three neighbors. It can be considered a derivative of graphite, which consists of many graphene sheets stacked atop each other. Graphite is inexpensive and has long been in use as an intercalation medium in lithium-ion batteries due to its conductivity and chemical stability. Compared to graphite, the extremely thin 2-d structure of graphene affords it even higher electronic conductivity, surface area, and mechanical strength, and has promising new applications in energy storage.[1–3] Graphene is also closely related to graphene nanoribbons, which are thin strips of graphene produced through chemical unzipping of 1-d carbon nanotubes, which have been used as conductive filler material in lithium-ion anodes, for example[4]

Graphene can be functionalized with various groups leading to variants such as halogenated and sulfonated graphenes.[5] A more common variant of graphene is graphene oxide (GO), which contains oxygen functional groups like carboxyl and hydroxyl attached to some of the carbon atoms. These interruptions of the carbon pattern act as defects and reduce the conductivity of the material. However, the oxygen functional groups can benefit dispersion of graphene and the catalytic properties of the sheet. GO also benefits from efficient production through the Hummer’s method. GO can be chemically reduced, removing the oxygen groups to yield reduced graphene oxide (RGO). Although similar to graphene at first glance, the defects present in RGO from the addition and subsequent removal of oxygen groups reduce the performance of the material compared to graphene produced through other methods.

6.1.2 Graphene synthetic methods

If graphene is to be used in widespread applications, key challenges in its production must first be addressed. Bottom-up synthetic approaches like epitaxial growth and chemical vapor deposition can produce very high quality graphene sheets, but at very high costs. Top-down approaches like exfoliation of graphite promise lower costs and better scalability, but challenges in conversion and defects require further study. To exfoliate graphite into graphene, strong shear flow is created within a graphite/water suspension. One potential method to achieve this is through a Taylor-Couette reactor, which contains a rotating inner cylinder concentrically placed within a stationary outer cylinder. The graphite/water suspension travels between the cylinders and is exposed to high shear stresses which rip graphene sheets from the graphite chunks. The reactor can also increase the gap spacing between layers of graphite, which can ease exfoliation in later processing steps. The Taylor-Couette reactor has had success yielding both graphene and graphene oxide products.[6,7] To simulate the effects of shear on the graphite at the nanoscale level, nonequilibrium molecular dynamics simulations are employed.

6.1.3 Graphene fibers

Graphene fibers can be created from graphene suspensions through a wet spinning process.[8] In this process, graphene suspended in water is ejected from a nozzle into a water/ethanol bath containing a coagulating agent like cetyl trimethyl ammonium bromide (CTAB). Upon contact with the coagulating agent, the graphene sheets condense and form a continuous fiber. Also, as graphene is pushed through the restricting nozzle, the graphene sheets align towards the flow direction. This may have important implications for the morphology and properties of the final fiber. After the fiber enters the coagulation bath, it can be removed physically from the bath and allowed to dry. The graphene fibers have diameters on the micron scale, and inherit some of the strong thermal, electrical, and mechanical properties of the graphene sheets. This allows their potential applications in synthetic fibers and aerospace materials.[9–11]

If the graphene fibers can be produced in such a way that allows them to be redispersed into water, substantial transportation costs can be saved. Currently, graphene will restack into graphite if it is not dispersed in water. The high water fraction greatly raises the cost of graphene transportation. Graphene fibers provide a potential workaround by loosely binding graphene sheets without restacking them. If this can be achieved, graphene could be redispersed at its final destination after transport to recover the original material properties. An optical microscope image of a wet spun graphene fiber is shown in Figure 6.1.

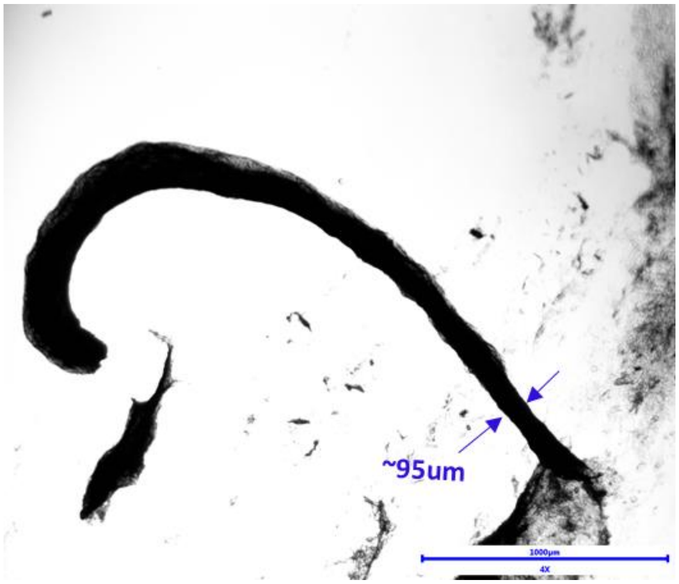

Figure 6.1 Optical microscope image a of a wet spun graphene fiber.

The application of graphene fibers depends on the morphology of the fiber, which is affected by the processing conditions. To better understand the effect of the confinement and deformation of the graphene sheets during the wet spinning process, a nonequilibrium coarse-grained molecular dynamics method is used.

6.2 Graphite simulation under shear flow

6.2.1 Simulation method

Non-equilibrium molecular dynamics was used to study the effect of shear flow on graphite in water. The simulation was conducted with a finite-sized atomistic graphite and coarse-grained water. The graphite is assumed to be resting on a flat wall representing the side of the Taylor-Couette reactor, and the bottom layer of the graphite is attached to the wall with a no-slip condition. The remaining space in the simulation is filled by water.

For graphite, neighboring carbon atoms in the honeycomb structure are connected by a harmonic bond potential,

$$u_{\mathrm{bond}}(r) = \mathrm{K}_b(r - r_0)^2$$

which serves to resist stretching of the sheet. u is the potential energy of the interaction, K is the stiffness parameter, r is the distance between two carbon atoms, and r_0 is the equilibrium bond distance. Stiffness to in-plane twisting is provided by a harmonic angle potential,

$$u_{\mathrm{angle}}(r) = \mathrm{K}_\theta(\theta - \theta_0)^2$$

which connects every 3 carbons. θ is then angle between 3 carbons and θ_0 is the equilibrium angle. Out-of-plane sheet bending stiffness is provided by a dihedral potential,

$$u_{\mathrm{dihedral}}(r) = \mathrm{K}_{\mathrm{dihedral}}(1 - \cos(2\varphi))$$

which connects every four carbons. φ is the dihedral angle.Parameters were adapted from An et al. and the OPLS-AA force field.[12] The parameters used in the model are given in Table 6.1.

Table 6.1 Parameters for the nonequilbrium graphite simulation.

Parameter	**Value**
Box x dimension	13.2nm
Box y dimension	26.4nm
Box z dimension	12.8nm
Number of beads	120000
Number of layers in graphite	26
Graphite layer spacing	0.34nm
Graphite x dimension	6.8 nm
Graphite y dimension	13.2nm
Temperature	300K
Shear rate	10^9 – 10^{11} s^{-1}
Harmonic bond stiffness, K_b	4690000 kcal mol^{-1} nm^{-2}
Harmonic bond equilibrium distance, r_0	0.142nm
Harmonic angle stiffness, K_θ	252 kcal mol^{-1} $radian^{-2}$
Harmonic angle equilibrium angle, θ_0	120 degrees
Harmonic dihedral stiffness, $K_{dihedral}$	5 kcal mol^{-1}
Number of timesteps	1000000
Timestep size	0.1 femtosecond

The atoms interact with one other with pair-wise potentials. All pairwise potentials (wall, carbon, water) are of the Lennard-Jones form and parameters were determined from the MARTINI force field.[13] Water is coarse-grained into four water per MD bead according to the MARTINI model. For carbon-carbon pairwise interactions, only carbons in neighboring sheets interact. Carbons within the same sheet or carbons two sheets away or more do not interact through Lennard-Jones potentials. The following equation is the Lennard-Jones potential used for all pairwise potentials. Values for pair parameters are given in Table 6.2.

$$u(r) = 4\varepsilon\left[\left(\frac{\sigma}{r}\right)^{12} - \left(\frac{\sigma}{r}\right)^{6}\right] + \varepsilon, \qquad r \leq 1\text{nm}$$

$$u(r) = 0, \quad r > 1\text{nm}$$

Table 6.2 Lennard-Jones parameters for graphite model.

Interaction	**ε (kcal mol^{-1})**	**σ(nm)**
C-C, C-wall	0.0556	3.4
C-water, water-wall	0.16	4.7
water-water	1.195	4.7

The graphite initial coordinates were generated using a Matlab file. Due to the rigid bond and angle constraints on the graphite, it must start from a minimum energy initial condition. The graphite is placed parallel and touching to the z-bottom of the simulation box, where a wall is created. Computational limitations require much smaller graphene compared to the micron-sized flakes seen in experiment. Water coarse-grained beads were generated randomly and equilibrated at the beginning of the simulation.

Shear flow with flow in the x direction and gradient in the z direction was implemented Lee-Edwards conditions in LAMMPS. This approach rescales the deforming simulation box after it becomes too skewed, and particles are moved back into to the rescaled box using the periodic boundary conditions. The shear flow is only applied to the water beads, which then impact the graphite to confer an effective shear stress. A schematic of the simulation setup is shown in Figure 6.2.

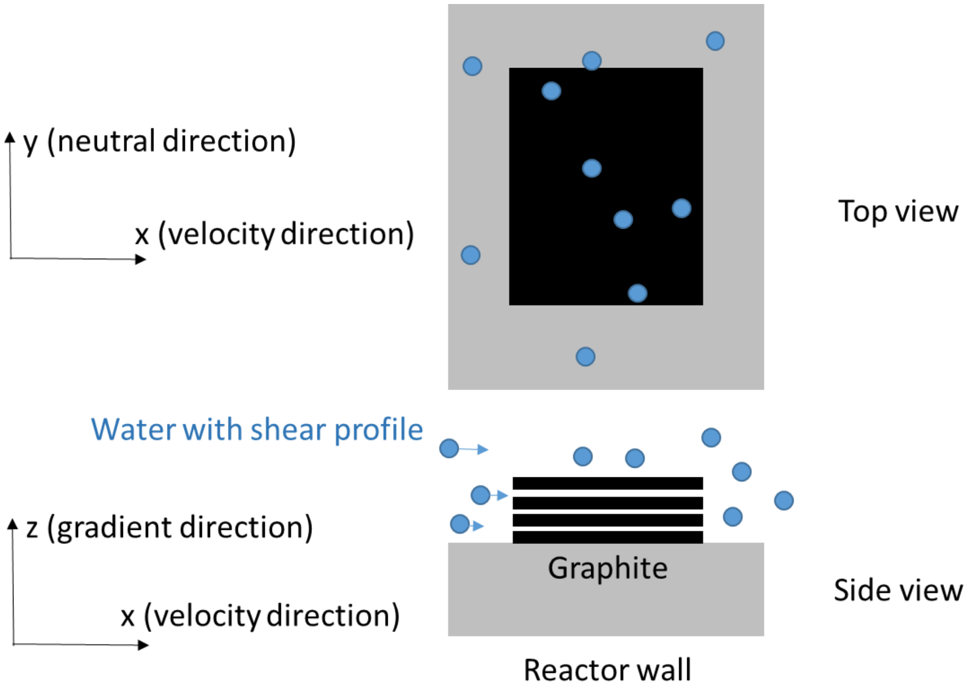

Figure 6.2 Side and top view of the graphite shear simulation.

Bead positions and velocities were calculated using the SLLOD equations of motion with following shear velocity gradient:

$$\frac{du_i}{dx_j} = \begin{bmatrix} 0 & 0 & \dot{\gamma} \\ 0 & 0 & 0 \\ 0 & 0 & 0 \end{bmatrix}$$

The SLLOD equation, which incorporates shear flow directly into the equations of motion, was integrated using a Velocity Verlet approach.

6.2.2 Results and discussion

Figure 6.3 shows the graphite simulation attached to reactor wall under shear.

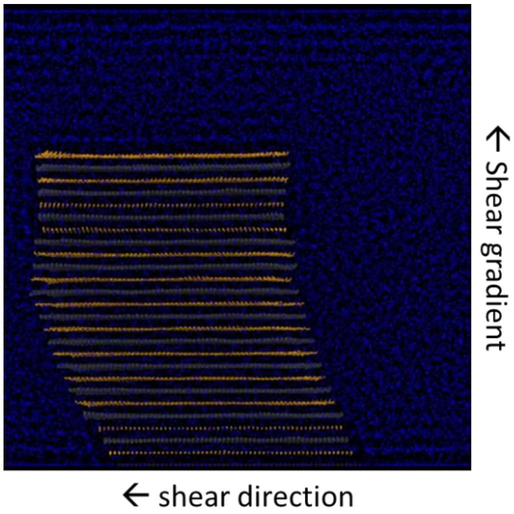

Figure 6.3 Visualization of graphite under shear flow, side perspective. Blue beads are water and grey/yellow beads are alternating layers of graphite. The shear rate was $5x10^9$ s^{-1}.

In the simulation, graphite layers will slide against each other in the shearing direction. This is likely due to the high shear rates and small graphite flake size, and is less likely to occur in experiments. With sufficient shear, layers will rip off and exfoliate into single or multi-layered graphene.

In experiments, the Taylor-Couette reactor has increased the gap spacing between gap layers. To measure the gap spacing in simulation, the distance between adjacent layers is calculated by finding the z-dimension center of mass for the two layers and subtracting. This is plotted in Figure 6.4 for two cases: simulations where the graphite is pinned (frozen) to the reactor wall and where it is unpinned (unfrozen) and allowed to slide along the surface.

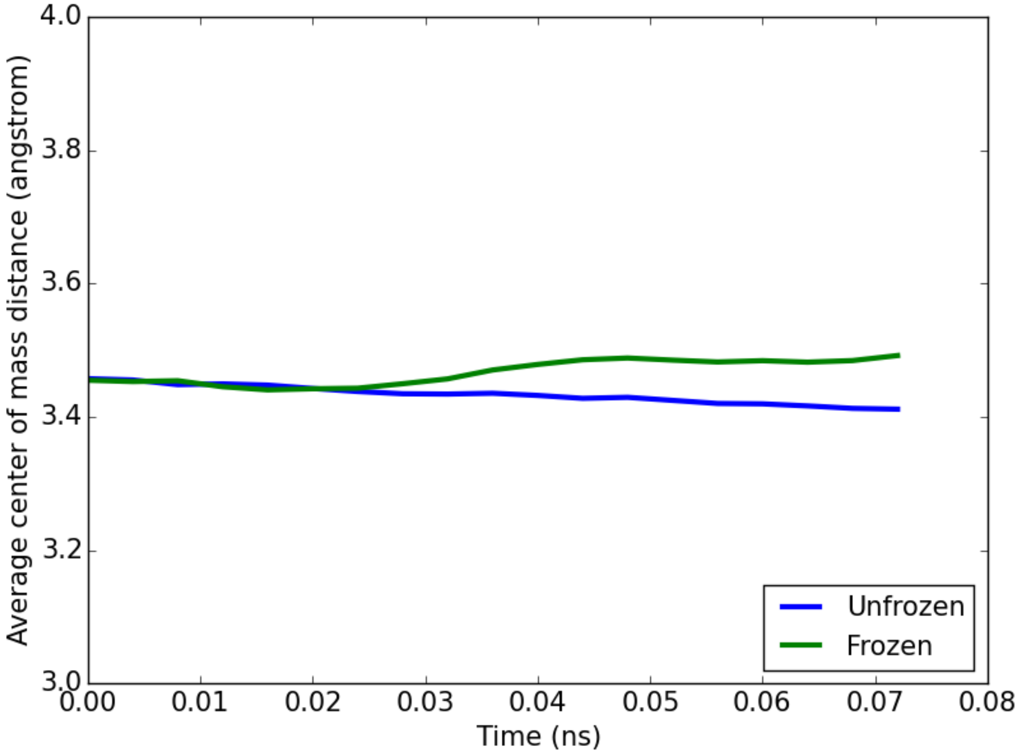

Figure 6.4 Average gap spacing during the shear flow simulation as a function of time and reactor wall pinning.

The graphite that is pinned to the reactor wall faces a much higher shear stresses as it is unable to slide long with the shear flow, resulting in greater separation of layers due to the high shear. This preliminary result demonstrates that MD simulation may be able to explain the mechanisms behind gap expansion in Taylor-Couette reactor experiments.

6.2.3 Future directions

The graphite simulations still require significant work. First, there are issues with the equilibration in some simulations which ruin the simulation if they occur. These problems are likely related to the thermostats for water and carbon. Because shear flow is only applied directly to water, the thermostats are more complex than a typical MD simulation. Second, it may not be reasonable to use coarse grained water in combination with atomistic graphite. It could be better to use atomistic water instead, but at the cost of considerable loss in efficiency. Third, the water does not currently behave properly and shows signs of crystallization. This is a common problem in MD simulations as water has proven to be highly difficult to simulate accurately. Possible solutions include finding a better forcefield for water or increasing the temperature. Fourth, the unrealistic small size of the graphite may bias simulation results. While the number of layers at 26 is matched to experiment, the large graphite flakes' lateral dimensions cannot be represented within computational limitations. This issue must be taken into account before simulation results can be directly compared to experiments.

6.3 Graphene simulation under extension and cylindrical confinement

6.3.1 Simulation method

Uniaxial extension with cylindrical confinement was performed in LAMMPS using the same general simulation method as in Chapter 4. Initially, graphene sheets were

Table 6.3 Parameters for the nonequilbrium graphene simulation. Parameters are in MD reduced units. Lengths approximately correspond to 1nm.

Parameter	**Value**
Cylinder start radius	200
Cylinder end radius	15-25
Graphene density	2wt%
Number of beads	609000
Graphite layer spacing	0.34
Graphite length dimension	14
Graphite width dimension	2.8-14
Temperature	1
Uniaxial extensional strain rate	0.04
Harmonic bond stiffness, $\mathbf{K}_{\boldsymbol{b}}$	1000
Harmonic bond equilibrium distance, $\boldsymbol{r}_{\mathbf{0}}$	1
Harmonic angle stiffness, $\mathbf{K}_{\boldsymbol{\theta}}$	500
Harmonic angle equilibrium angle, $\boldsymbol{\theta}_{\mathbf{0}}$	120 degrees
Harmonic dihedral stiffness, $\mathbf{K}_{\boldsymbol{dihedral}}$	5
Number of timesteps	300000
Timestep size	1
Lennard-Jones $\boldsymbol{\varepsilon}$	1
Lennard-Jones $\boldsymbol{\sigma}$	1

generated with random orientation at a density matching experiment. The graphene was coarse-grained with the ratio 4 carbons : 1 coarse-grained carbon, which maintains the same hexagonal carbon structure.[14] The coarse-graining is shown in Figure 6.5. The graphene sheets were equilibrated to prevent overlap before running the extensional deformation. Pair interactions between carbon atoms only occur for carbons more than four bonds away, and use the WCA potential.[15] The simulation scale and graphene size were chosen to be as large as possible within computational limits. Simulation parameters are shown in Table 6.3. No water is included in order to maintain computational efficiency.

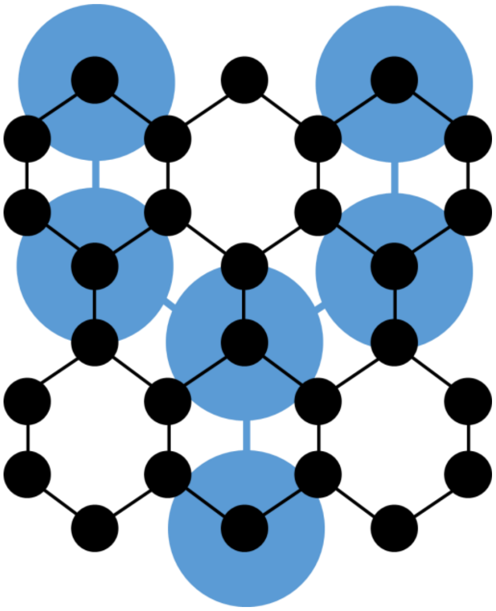

Figure 6.5 Graphene coarse graining scheme. Black spheres and lines represent carbon atoms and bonds, while blue spheres and lines represent coarse-grained carbon beads and bonds. Four carbon atoms form one coarse-grained bead.

6.3.2 Results and discussion

Figure 6.6 shows the visualizations of the graphene fiber before and after extensional strain. Initial, graphene sheets are oriented randomly. During extension and confinement, they are forces align towards the z direction. In addition, as the confinement radius decreases graphene sheets are forces to begin to curl and fold instead of maintaining their planar structure.

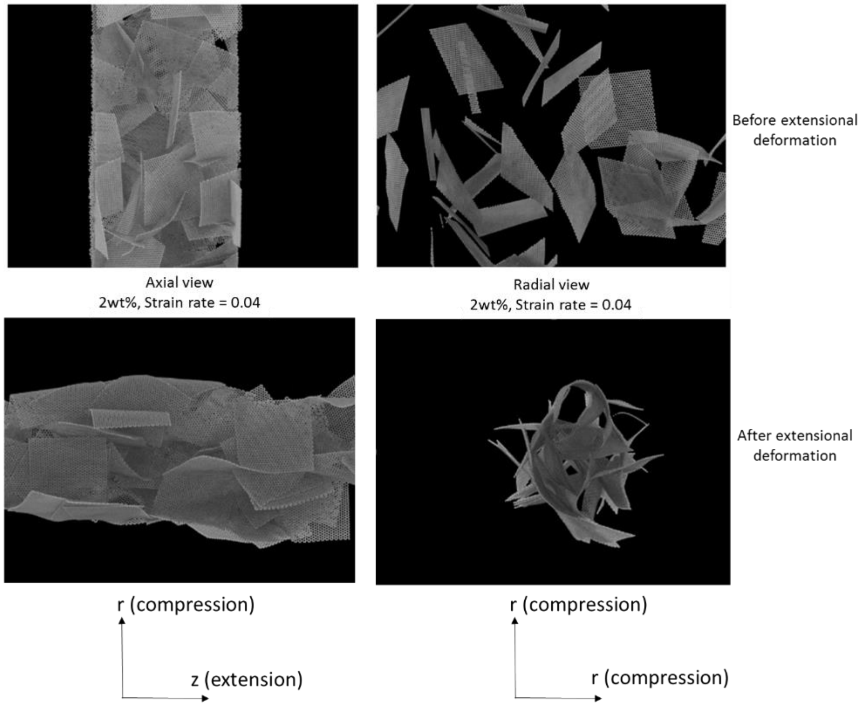

Figure 6.6 Symmetric graphene extensional simulation from axial and radial perspectives. Graphene sheets were 14nm by 14nm in size.

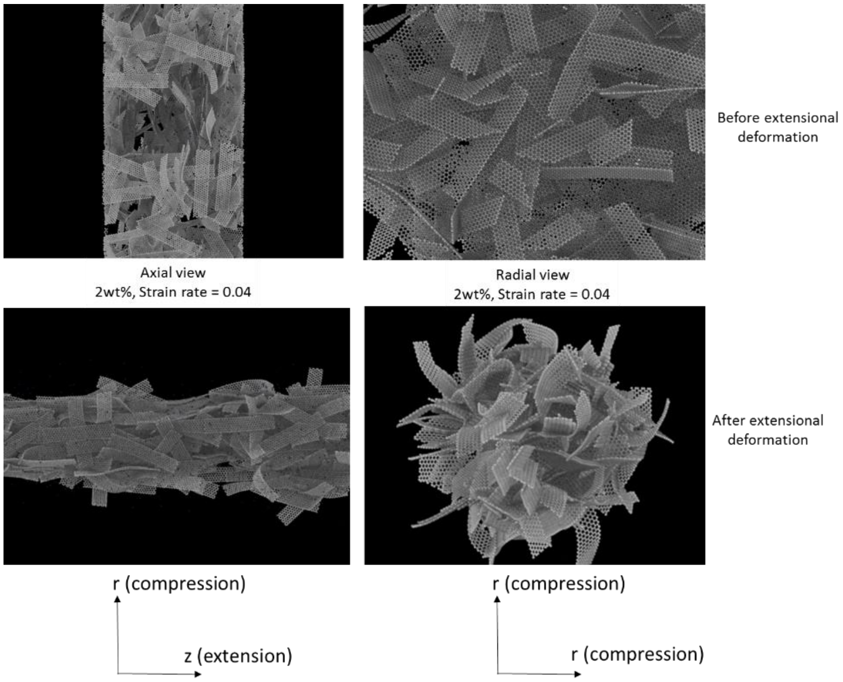

Figure 6.7 Asymmetric graphene extensional simulation from axial and radial perspectives. Graphene sheets were 14nm by 2.8nm in size.

In Figure 6.7, the simulation was repeated but with 5:1 aspect ratio graphene sheets instead of 1:1. These sheets can pack more easily due to their smaller size and increased flexibility, allowing them to form smaller diameter fibers. The results in Figure 6.6 and Figure 6.7 show qualitative agreement with experimental scanning electron microscope images. However, the simulations could benefit from further investigation into multi-layer graphene, which is more common than single-layer graphene in experiments. Additional improvements could include inclusion of water and modeling the effect of the CTAB coagulating agent on the fiber after extensional deformation is complete.

6.4 Conclusions

Nonequilibrium molecular dynamics simulations were used to simulate graphite and graphene processing methods. Early results from graphite under shear shows that gap spacing between layers can increase when the graphite is considered to be resting on the reactor wall with a no slip condition. To model graphene fiber wet spinning, graphene sheets underwent uniaxial extension and cylindrical confinement. It was found that a higher ratio of graphene size to confinement diameter forces graphene sheets to curl and fold. Also, the flexibility and size of the graphene plays an important role in the morphology and packing in the resulting graphene fiber.

6.5 References

1. Chen, L. *et al.* Toward high performance graphene fibers. *Nanoscale* **5**, 5809–5815 (2013).

2. Halim, W. *et al.* Directly deposited binder-free sulfur electrode enabled by air-controlled electrospray process. *ACS Appl. Energy Mater.* **2**, 678–686 (2019).
3. Fei, L. *et al.* Graphene Folding in Si Rich Carbon Nanofibers for Highly Stable, High Capacity Li-Ion Battery Anodes. *ACS Appl. Mater. Interfaces* **8**, 5243–5250 (2016).
4. Shoorideh, G. *et al.* Harvesting Interconductivity and Intraconductivity of Graphene Nanoribbons for a Directly Deposited, High-Rate Silicon-Based Anode for Li-Ion Batteries. *ACS Appl. Energy Mater.* **1**, 1106–1115 (2018).
5. Munaiah, Y., Ragupathy, P. & Pillai, V. K. Single-Step Synthesis of Halogenated Graphene through Electrochemical Exfoliation and Its Utilization as Electrodes for Zinc Bromine Redox Flow Battery. *J. Electrochem. Soc.* **163**, A2899–A2910 (2016).
6. Tran, T. S., Park, S. J., Yoo, S. S., Lee, T. R. & Kim, T. Y. High shear-induced exfoliation of graphite into high quality graphene by Taylor-Couette flow. *RSC Adv.* **6**, 12003–12008 (2016).
7. Park, W. K. *et al.* Facile synthesis of graphene oxide in a Couette-Taylor flow reactor. *Carbon N. Y.* **83**, 217–223 (2015).
8. Xu, Z. & Gao, C. Graphene fiber: A new trend in carbon fibers. *Mater. Today* **18**, 480–492 (2015).
9. Jalili, R. *et al.* Scalable one-step wet-spinning of graphene fibers and yarns from liquid crystalline dispersions of graphene oxide: Towards multifunctional textiles. *Adv. Funct. Mater.* **23**, 5345–5354 (2013).
10. Dong, Z. *et al.* Facile fabrication of light, flexible and multifunctional graphene

fibers. *Adv. Mater.* **24**, 1856–1861 (2012).

11. Cong, H. P., Ren, X. C., Wang, P. & Yu, S. H. Wet-spinning assembly of continuous, neat, and macroscopic graphene fibers. *Sci. Rep.* **2**, 1–6 (2012).

12. An, X. *et al.* Stable aqueous dispersions of noncovalently functionalized graphene from graphite and their multifunctional high-performance applications. *Nano Lett.* **10**, 4295–4301 (2010).

13. Marrink, S. J., Risselada, H. J., Yefimov, S., Tieleman, D. P. & Vries, A. H. De. The MARTINI Force Field : Coarse Grained Model for Biomolecular Simulations. **111**, 7812–7824 (2007).

14. Ruiz, L., Xia, W., Meng, Z. & Keten, S. A coarse-grained model for the mechanical behavior of multi-layer graphene. *Carbon N. Y.* **82**, 103–115 (2015).

15. Weeks, J., Chandler, D. & Andersen, H. C. Role of Repulsive Force in Determining the Equilibrium Structure of Simple Liquids. *J. Chem. Phys.* **54**, 5237 (1971).

CHAPTER 7

SUMMARY AND FUTURE WORK

Continued progress in electric vehicles, personal electronics, and grid-scale energy storage requires improvements in energy storage materials. Towards this aim, molecular dynamics simulations are carried out to model the effects of the electrospinning process on polymer systems. The polymer electrospun fibers have applications as nanoparticle hosts or as mesoporous carbon nanofiber precursors in next generation batteries like lithium sulfur. To model lithium sulfur batteries, a numerical simulation is developed and used to investigate cathode structure, adsorption, and gel electrolyte. The simulation is a promising tool to aid in experimental efforts to design improved energy storage materials and understand results.

Future research should focus on improving the Li-S model further. Useful additions include migration of ions, conductivity of the electrodes, change in diffusion based in the concentrations of species in the electrolyte, and an improved representation of the battery separator. Also, experimental work could be done to determine some of the many model parameters that are currently unknown such as adsorption parameters and polysulfide diffusion coefficients. A particularly promising addition to the field could be the combination of mass transport limitations and passivation into a single model. This model would need to explore scenarios where one or both of the failure mechanisms play a role. A final direction could be to focus on the charge of the battery.

Beyond the directions listed already, many promising avenues require additional theoretical knowledge of what happens inside a lithium-sulfur battery. For example, the exact composition of polysulfides in the battery under highly concentrated conditions would require targeted experiments to elucidate. Further understanding of the lithium sulfide deposition patterns within the complex porous carbon cathode structure could improve the model's treatment of clogging and passivation.

The model should also play a role in supporting the future efforts of experimentalists in the group. Ultimately, simulations are most useful as a supportive tool for the more practical efforts required for progress in the field. As a researcher focused on the fundamental mechanisms of the battery, the future simulation user should aim to provide a different perspective to aid the interpretation of often confusing and complex experimental data.